UNIVERSITY OF BIRMINGHAM

Investigating the homeostatic role and biomedical implications of the autophagy–NAD axis using human pluripotent stem cell-based platforms

By Congxin Sun

A thesis submitted to The University of Birmingham for the degree of DOCTOR OF PHILOSOPHY

Institute of Cancer & Genomic Sciences,
College of Medical and Dental Sciences
University of Birmingham
July 2024

ACKNOWLEDGEMENTS

I thank my supervisor, Dr Sovan Sarkar, for all the guidance, support and help throughout my PhD. I thank Dr Elena Seranova, Dr Dewi Astuti, Dr Gamze Kocak, Dr Malgorzata Zatyka, Ms Miriam Kosgen and Dr Tatiana Rosenstock in Sarkar lab for technical assistance and scientific discussions. I also thank Dr Jenny Roberts (University of Birmingham) for metabolite and amino acid uptake measurements, Dr Oliver Maddocks (Glasgow University) for metabolomics, Dr Samuel Lara Reyna (University of Birmingham) for Seahorse assay, Dr Benjamin Delprat (University of Montpellier, France) for drug testing in Wolfram syndrome zebrafish model, and Prof. Viktor Korolchuk (Newcastle University) for collaboration on autophagy and NAD. Finally, I am immensely thankful to my parents for their love and support throughout my life.

Abstract

Autophagy is a homeostatic process critical for cell survival and human health. It is an intracellular degradative process that removes undesirable macromolecules (like protein aggregates) and damaged organelles (like mitochondria) from the cells. Due to the vital role of autophagy in maintaining cellular homeostasis, malfunction of this process contributes to cell death and tissue degeneration. This is particularly detrimental for post-mitotic cells like neurons. Indeed, dysfunction of autophagy has been implicated in diverse human pathological conditions including a range of neurodegenerative diseases. However, the mechanistic understanding of how impairment in autophagy contributes to cell death remains elusive. Elucidating the cytotoxic mechanism will be of biomedical interest for developing therapeutic interventions to combat neurodegeneration.

To undertake human-relevant biology in physiological and preclinical *in vitro* experimental platforms, human embryonic stem cells (hESCs) and human induced pluripotent stem cells (iPSCs) were utilised in this study to generate neuronal cells. A genetic hESC model with autophagy knockout (*ATG5*$^{-/-}$) was used for generating human neurons with autophagy deficiency in order to study how loss of autophagy affects neuronal survival. Autophagy-deficient hESCs and hESC-derived neurons exhibited higher cell death at basal level accompanied by metabolic defects. Depletion of a metabolite called nicotinamide adenine dinucleotide (NAD) due to hyperactivation of NAD-consuming enzymes, such as SIRTs and PARPs, was found to trigger cell death via mitochondrial depolarisation in *ATG5*$^{-/-}$ hESC-derived neurons. Elevating intracellular NAD levels by supplementation with NAD precursors promoted the survival of *ATG5*$^{-/-}$ hESC-derived neurons by restoring mitochondrial bioenergetics and proteostasis. These findings elucidate a mechanistic link between autophagy deficiency and neuronal cell death that can be targeted for therapeutic interventions in neurodegenerative diseases associated with autophagic defects.

The biomedical relevance of this mechanism was further investigated in patient-derived iPSC model of a rare, early-onset neurodegenerative disease called Wolfram syndrome (WS). WS patient iPSC-derived neurons exhibited higher cell death that was associated with defective autophagy and NAD depletion, along with mitochondrial dysfunction and impairment in proteostasis. Targeting the defective autophagy–NAD axis in WS by autophagy and NAD enhancers ameliorated these disease phenotypes and improved the

survival of WS patient iPSC-derived neurons, thereby highlighting a potential therapeutic strategy for the treatment of WS.

For future clinical translation by drug repurposing, a human neuronal platform was established using an autophagy reporter (mCherry-EGFP-LC3) hESC line in order to identify FDA-approved, CNS-penetrant, autophagy-inducing drugs via image-based chemical screen. Based on the efficacy in inducing autophagy at clinically-relevant dose, paediatric use, oral deliverability, and mTOR independence, four high-confidence hits were selected that include carbamazepine, nimodipine, sodium valproate and verapamil. All these FDA-approved autophagy inducers were shown to rescue disease phenotypes and improve cell survival in WS patient iPSC-derived neurons, thus informing potential drug candidates for clinical trials in future.

In a nutshell, defective autophagy–NAD axis was found to contribute to neuronal cell death, whilst targeting this cytotoxic cascade by autophagy and NAD enhancers exerted therapeutic benefits in patient-derived neuronal cells of a rare neurodegenerative disease. Since many rare and common neurodegenerative conditions are associated with autophagy dysfunction and NAD depletion, the findings from this work has the potential to be generalisable to some of these disease contexts.

List of figures

Figure	1.1	The mechanism of autophagy	20
Figure	1.2	The signalling pathway regulating autophagy	24
Figure	1.3	Chemical screening methods using LC3-based autophagy reporters for identifying autophagy modulators in mammalian cells	27
Figure	1.4	The role of autophagy in the maintenance of metabolic homeostasis	29
Figure	1.5	The application of a hiPSC-based platform in studying autophagy, disease modelling and drug discovery	35
Figure	2.2	*ATG5*$^{-/-}$ hESCs exhibit pluripotency markers and maintain proliferative capacity	41
Figure	2.3	Loss of autophagy and increased cell death in *ATG5*$^{-/-}$ hESCs	42
Figure	2.4	Differentiation of *ATG5*$^{-/-}$ NPs and neurons from *ATG5*$^{-/-}$ hESCs	44
Figure	2.5	Autophagy deficiency and increased cell death in *ATG5*$^{-/-}$ hESC-derived NPs and neurons	45
Figure	2.6	Metabolic perturbations in *ATG5*$^{-/-}$ hESC-derived neurons	48
Figure	2.7	Elevation of glucose uptake in *ATG5*$^{-/-}$ hESC-derived neurons	51
Figure	2.8	[U-$^{13}C_6$]-Glucose tracer shows greater contribution of glucose-derived carbons from glycolytic pathway in *ATG5*$^{-/-}$ hESC-derived neurons	52
Figure	2.9	[U-$^{13}C_6$]-Glucose tracer shows greater contribution of glucose in glycolysis and TCA cycle metabolites in *ATG5*$^{-/-}$ hESC-derived neurons	53
Figure	2.10	Depletion of ATP, ADP, NAD^+ and NADH in *ATG5*$^{-/-}$ hESC-derived neurons	54
Figure	2.11	Amino acid uptake profiling in *ATG5*$^{-/-}$ hESC-derived neurons	56
Figure	2.12	Supplementation of L-tryptophan restores NAD levels and rescues viability of *ATG5*$^{-/-}$ hESC-derived neurons	57
Figure	2.13	Suppression of NAD production by NAMPT inhibitor FK866 increases cell death in *ATG5*$^{-/-}$ hESC-derived neurons	59
Figure	2.14	NAD precursor NAM increases NAD levels and improves cell viability in *ATG5*$^{-/-}$ hESC-derived neurons	60
Figure	2.15	Boosting NAD with NR and NMN restore NAD levels and improve cell viability in *ATG5*$^{-/-}$ hESC-derived neurons	61

Figure	2.16	Increased NADase activity in *ATG5*$^{-/-}$ hESC-derived neurons	63
Figure	2.17	Inhibition of SIRTs and PARPs rescues NAD levels and cell viability in *ATG5*$^{-/-}$ hESC-derived neurons	64
Figure	2.18	Increased DNA damage in *ATG5*$^{-/-}$ hESC-derived neurons	65
Figure	2.19	NAD depletion triggers cell death via mitochondrial depolarisation in *ATG5*$^{-/-}$ hESC-derived neurons	68
Figure	2.20	Suppression of NADH consumption by CP2 rescues NAD levels and cell viability in *ATG5*$^{-/-}$ hESC-derived neurons	69
Figure	2.21	NAD boosters restore mitochondrial membrane potential and respiration in *ATG5*$^{-/-}$ hESC-derived neurons	70
Figure	2.22	NAD boosters reduce aggresomes in *ATG5*$^{-/-}$ hESCs and hESC-derived neuronal cells	72
Figure	3.1	Autophagy inducers rescue the defective autophagic flux in WS patient iPSC-derived neurons	77
Figure	3.2	Autophagy inducers rescue aggresome accumulation and mitochondrial depolarisation WS patient iPSC-derived neurons	78
Figure	3.3	Autophagy inducers rescue cell death in WS patient iPSC-derived neurons	80
Figure	3.4	Depletion of intracellular NAD levels in WS neuroblastoma cell model and patient iPSC-derived neurons	81
Figure	3.5	NAD boosters rescue the defective autophagic flux and proteostasis in WS patient iPSC-derived neurons	83
Figure	3.6	NAD boosters rescue mitochondrial bioenergetics and cell viability in WS patient iPSC-derived neurons	85
Figure	3.7	NAD boosters rescue hyperlocomotion phenotype on visual motor response (VMR) test in WS zebrafish model	87
Figure	4.1	Generation and characterization of autophagy reporter hESC line	91
Figure	4.2	Differentiation of mCherry-EGFP-LC3 hESCs into neural precorsors and neurons	93
Figure	4.3	Image-based chemical screen with FDA-approved and investigational autophagy-inducing drugs in autophagy reporter	97

hESC-derived neuronal precursors

Figure 4.4 Chemical screen hits that are FDA-approved autophagy-inducing drugs suitable for paediatric use rescue disease-relevant phenotypes in WS patient iPSC-derived neurons 98

Figure 5.1 Summary of findings in Chapter 2 102

List of tables

Table	1	LC–MS based metabolomic data	129
Table	2	List of control (CT) and Wolfram Syndrome (WS) patient-derived hiPSC lines from which neural precursors and neurons were derived	130
Table	3	Compounds used for modulating NAD levels	131
Table	4	List of primary and secondary antibodies for immunoblotting analysis	132
Table	5	List of primary and secondary antibodies for immunofluorescence analysis	133
Table	6	Primers used for qPCR	134
Table	7	List of primary and secondary antibodies for immunoprecipitation	135
Table	8	FDA-approved and investigational compounds used for high-content screening in mCherry-EGFP-LC3 autophagy reporter hESC-derived NPs	136

List of abbreviations

AAVS1	Adeno-associated virus integration site 1
AD	Alzheimer's disease
ADP	Adenosine diphosphate
ALS	Amyotrophic lateral sclerosis
AMBRA1	Activating molecule in Beclin 1-regulated autophagy protein 1
AMP	Adenosine monophosphate
AMPK	AMP-activated protein kinase
ATG	Autophagy-related gene
ATP	Adenosine triphosphate
Baf A1	Bafilomycin A1
cAMP	3',5'-cyclic adenosine monophosphate
CNS	Central nervous system
DAPI	4′,6-Diamidino-2-Phenylindole
DFCP1	Double FYVE domain containing protein 1
DMSO	Dimethyl sulfoxide
DNA	Deoxyribonucleic acid
EB	Embryoid body
EGFP	Enhanced green fluorescent protein
ER	Endoplasmic reticulum
ETC	Electron transport chain
FCCP	Carbonyl Cyanide-4-(Trifluoromethoxy)Phenylhydrazone
FDR	False discovery rate
FM	Full medium
FIP200	Focal adhesion kinase family-interacting protein of 200 kDa
GD	Gaucher disease
HBSS	Hanks balanced salt solution
HCS	High-content screening

HOPS	Homotypic fusion and protein sorting
HTS	High-throughput screening
IP_3	Inositol 1,4,5-trisphosphate
LIR	LC3-interaction region
mCherry	Monomeric Cherry
MEFs	Mouse embryonic fibroblasts
MS	Mass spectrometry
NAD+	Nicotinamide adenine dinucleotide (oxidised form)
NADH	Nicotinamide adenine dinucleotide (reduced form)
NAM	Nicotinamide
NAMPT	Nicotinamide phosphoribosyltransferase
NBR	Nucleotide releasing buffer
NBR1	Neighbor of BRCA1 gene 1
NCL	Neuronal ceroid lipofuscinosis
NDP52	Nuclear dot protein of 52 kDa
NO	Nitric oxide
NPM	NP medium
NPs	Neural precursors
NR	Nicotinamide riboside
NRH	Dihydronicotinamide riboside
OCT4	Octamer-binding transcription factor 4
OD	Optical density
OPTN	Optineurin
OXPHOS	Oxidative phosphorylation
PARPs	Poly-ADP-ribose polymerases
PAS	Phagophore assembly site
PCA	Principal component analysis
PE	Phosphatidylethanolamine

PI3KC3-C1	Class III phosphatidylinositol-3-kinase complex 1
PI3P	Phosphatidylinositol 3-phosphate
ROS	Reactive oxygen species
RT	Room temperature
SIRTs	Sirtuins
SNAREs	Soluble N-ethylmaleimide-sensitive factor-attachment protein receptors
SOX2	SRY (sex determining region Y)-box 2
SQSTM1	Sequestosome 1
SSEA4	Stage specific embryo antigen 4
TALENs	Transcription activator-like effector nucleases
TCA	Tricarboxylic acid
TFEB	Transcription factor EB
TMRE	Teramethylrhodamine
UBD	Ubiquitin-binding domain
ULK1	Unc-51-like kinase-1
UVRAG	UV radiation resistance associated gene
VPS34	Vacuolar protein sorting 34
WIPI2	WD repeat domain phosphoinositide-interacting protein 2
ZFNs	Zinc finger nucleases
hESCs	Human embryonic stem cells
hiPSCs	Human induced pluripotent stem cells
mTOR	Mechanistic target of rapamycin
qPCR	Quantitative polymerase chain reaction
ΔΨm	Mitochondrial membrane potential

Table of contents

Chapter 1: Introduction

1.1. Overview 17

1.2. The mechanism of autophagy 17

1.2.1 Autophagy initiation and phagophore nucleation 17

1.2.2 Phagophore elongation and autophagosome formation 18

1.2.3 Autophagosome maturation and autolysosome formation 19

1.3. Nature of autophagic degradation 21

1.3.1 Nature of autophagic degradation 21

1.3.2 Non-selective autophagy 21

1.3.3 Selective autophagy 21

1.4. Regulation of autophagy by signalling pathways and small molecules 22

1.4.1 mTOR-dependent regulation autophagy 22

1.4.2 mTOR-independent regulation of autophagy 23

1.5. Methods for monitoring autophagy 25

1.5.1 Assays based on autophagosome turnover using LC3 reporters 25

1.5.1.1 GFP-LC3 reporter 25

1.5.1.2 mRFP-GFP-LC3 or mCherry-EGFP-LC3 reporters 26

1.5.2 Assays based on autophagic substrate clearance 26

1.6. The role of autophagy and NAD in cellular metabolism and ageing 28

1.7 Role of autophagy in human diseases 30

1.7.1 Role of autophagy in neurodegenerative diseases 30

1.7.2 Role of autophagy in Wolfram Syndrome 31

1.8 Human pluripotent stem cell-based platforms for studying autophagy and drug development 32

1.9 Aims and objectives 36

Chapter 2: NAD depletion mediates cytotoxicity in human neurons with autophagy deficiency

2.1 Introduction 38

2.2 Objectives 39

2.3 Results 39

2.3.1 Generation and characterisation of autophagy-deficient hESCs 39

2.3.2 Autophagy-deficient human neurons manifest with elevated cell death 43
2.3.3 Metabolic perturbations in autophagy-deficient human neurons 46
2.3.4 Depletion of ATP and NAD in autophagy-deficient neurons despite compensatory increase in glucose metabolism 49
2.3.5 Supplementation of L-tryptophan restores NAD levels and rescues viability of autophagy-deficient neurons 55
2.3.6 Boosting intracellular NAD improves the viability of autophagy-deficient neurons 58
2.3.7 Increased NADase activity mediates NAD depletion in autophagy-deficient neurons 62
2.3.8 NAD depletion triggers cell death via mitochondrial depolarization in autophagy-deficient neurons 66
2.3.9 Mitochondrial dysfunction perturbs proteostasis in autophagy-deficient neurons 71

Chapter 3: Targeting the autophagy-NAD axis rescues disease phenotypes in iPSC-derived neuronal model of Wolfram syndrome

3.1 Introduction 74
3.2 Objectives 75
3.3 Results 75
3.3.1 Autophagy inducers rescue defective autophagic flux in WS patient iPSC-derived neurons 75
3.3.2 Autophagy inducers restore proteostasis and mitochondrial membrane potential in WS patient iPSC-derived neurons 76
3.3.3 Autophagy inducers improve cell viability in WS patient iPSC-derived neurons 79
3.3.4 NAD depletion in WS patient iPSC-derived neurons 79
3.3.5 NAD boosters rescue defective autophagy and improve proteostasis in WS patient iPSC-derived neurons 82
3.3.6 NAD boosters improve mitochondrial bioenergetics and cell survival in WS patient iPSC-derived neurons 84
3.3.7 NAD boosters rescue disease-relevant phenotype in WS zebrafish model 86

Chapter 4: Chemical screen to identify FDA-approved autophagy inducers for biomedical applications

4.1 Introduction 89

4.2 Objectives 90

4.3 Results 90

4.3.1 Characterisation of autophagy reporter hESC line 90

4.3.2 Generation and characterisation of autophagy reporter neural precursors and neurons from hESCs 92

4.3.3 Chemical screen to identify FDA-approved autophagy-inducing drugs in autophagy reporter hESC-derived neural precursors 94

4.3.4 FDA-approved autophagy-inducing drugs are cytoprotective in WS patient iPSC-derived neurons 96

Chapter 5: Discussion

5.1 Overview of key research findings 100

5.1.1 NAD depletion mediates cell death underlying autophagy deficiency 100

5.1.2 Autophagy and NAD enhancers are cytoprotective in Wolfram Syndrome 102

5.1.3 Chemical screen identifies FDA-approved autophagy inducers for drug repurposing in neurodegenerative diseases 104

5.2 Limitations of research 104

5.3 Further work 105

Chapter 6: Methods and materials

6.1 Culture of human embryonic stem cells 109

6.2 Genome editing for ATG5 gene knockout in hESCs 110

6.3 Differentiation of hESCs into neural precursors and neurons 110

6.4 Neuronal differentiation of Wolfram syndrome patient-derived hiPSC lines 111

6.5 Compound treatment and amino acid supplementation 111

6.6 Immunoblotting analysis 112

6.7 Immunofluorescence 113

6.8 Image acquisition of fixed cells 113

6.9 Image analysis of pluripotency markers 114
6.10 Gene expression analysis 114
6.11 TUNEL assay for apoptotic cells 114
6.12 Cytotoxicity Assay 115
6.13 DAPI staining for apoptotic nuclear morphology 115
6.14 DNA damage analysis 115
6.15 Cell proliferation analysis 116
6.16 Proteostat aggresome assay 116
6.17 Measurement of SIRT1, SIRT2, PARP1 and PARP2 enzyme activity 116
6.18 NAD^+ and NADH measurements 117
6.19 ATP and ADP measurements 117
6.20 Mitochondrial ΔΨm and ROS measurements 118
6.21 Mitochondrial respiration measurement 118
6.22 MitoTracker staining and mitochondrial rod/branch length analysis 119
6.23 Mitochondrial and cytosolic fractionation 120
6.24 Analysis of glucose concentration in the medium 120
6.25 Analysis of amino acid concentrations in the medium by GC–MS 120
6.26 [U-$^{13}C_6$]-Glucose tracer labelling and analysis of metabolites by GC–MS 121
6.27 LC–MS-based metabolomics 121
6.28 Metabolomics data analysis 122
6.29 High Content drug screening of FDA-approved and investigational compounds 122
Quantification and statistical analysis 124

Key resource table 125
Tables 1–8 129
References 137
Appendix 1: List of published articles 149
Appendix 2: List of conference poster presentations 152

Chapter 1

Introduction

Chapter 1: Introduction

Some of the materials presented in this chapter have been previously published in the following review articles where I contributed to the text as a co-author:

1. *Seranova E, Palhegyi AM, Verma S et al. with Sun C and Sarkar S. Human Induced Pluripotent Stem Cell Models of Neurodegenerative Disorders for Studying the Biomedical Implications of Autophagy. J. Mol. Biol. 432(8):2754-2798 (2020)* [1].
2. *Wilson N, Kataura T, Korsgen ME, Sun C, Sarkar S and Korolchuk VI. The autophagy-NAD axis in longevity and disease. Trends Cell Biol. 33(9):788-802 (2023)* [2].

1.1 Overview

Autophagy is an intracellular degradation pathway for the clearance of unwanted cytoplasmic materials like aggregation-prone proteins, damaged organelles and invading pathogens. This biological process is essential for maintaining cellular homeostasis and survival, and is thus vital for human health. Autophagy plays a role in various physiological processes such as development, longevity and immunity, and is implicated in diverse human diseases including neurodegeneration, cancer and infectious diseases, amongst others. Therefore, understating the role of autophagy in cell survival is of fundamental interested, and therapeutic manipulation of this process is of biomedical interest.

1.2. The Mechanism of autophagy

In 1993, Yoshinori Ohsumi's laboratory identified autophagy-related (*Atg*) genes via genetic screens in yeast [3]. Autophagy is evolutionarily conserved from yeast to humans. The Atg proteins or its mammalian orthologs form the core autophagy machinery, which regulate multiple stages of the autophagy process, such as (i) initiation, (ii) phagophore nucleation and formation, (iii) phagophore elongation and autophagosome formation, (iv) lysosomal fusion and autolysosome formation [4].

1.2.1. Autophagy initiation and phagophore nucleation

Autophagy is triggered by stress signals such as nutrient deprivation (starvation). This process starts with the formation of isolated double-membrane structures called phagophores, which originate from specific areas of the endoplasmic reticulum (ER) called

phagophore assembly sites (PAS). The initiation of autophagy is orchestrated by a number of protein complexes (**Figure 1.1**). The initial step involves activation of the ULK1 (Unc-51-like kinase 1) complex, which consists of ULK1, FIP200 (focal adhesion kinase family-interacting protein of 200 kDa), ATG13 and ATG101. ULK1 complex then phosphorylates Beclin-1, and activates class III phosphatidylinositol-3-kinase complex 1 (PI3KC3-C1), which consists of VPS34 (vacuolar protein sorting 34), Beclin-1, ATG14L, and VPS15 [4-8]. ULK1 directly phosphorylates Beclin-1 that activates the lipid kinase VPS34, which in turn phosphorylates phosphatidylinositol to form phosphatidylinositol 3-phosphate (PI3P) [9-11]. PI3P, which is essential for autophagosome biogenesis at PAS, acts as the signaling molecule for recruiting PI3P-binding proteins like WIPI2 (WD repeat domain phosphoinositide-interacting protein 2) and DFCP1 (double FYVE containing protein 1) at PAS that contributes to phagophore expansion [8]. ULK1 also phosphorylates ATG9, which contributes lipids from ATG9-containing vesicles to the growing phagophore membrane [12].

1.2.2. Phagophore elongation and autophagosome formation

Two ubiquitin-like conjugation systems are essential for autophagosome formation (Figure 1). The first conjugation system involves ATG7 (as E1-like ubiquitin-activating enzyme) and ATG10 (as E2-like ubiquitin-conjugating enzyme) that mediate ATG5-ATG12 conjugation, which interacts with ATG16L1 to form the ATG12-ATG5-ATG16L1 complex [4, 6]. The second system promotes the conjugation of microtubule-associated protein 1 light chain 3 (LC3) with phosphatidylethanolamine (PE) to form membrane-bound LC3-II. LC3 first undergoes C-terminal post-translational cleavage by protease ATG4B to form cytosolic LC3-I, which is then conjugated with PE via ATG7(as E1-like ubiquitin-activating enzyme), ATG3 (as E2-like ubiquitin conjugating enzyme) and ATG12-ATG5-ATG16L complex (as E3-like ubiquitin ligase) to form the lipidated LC3-II. LC3-II remains bound to the autophagosome membrane throughout the autophagy process [13] and is thus used as a marker for autophagy to assess the steady-state level of autophagosomes in cells. LC3-II binds to both the inner and outer membrane of the autophagosome and after lysosomal fusion, LC3-II bound to the inner membrane is degraded, while those on the outer membrane are cleaved and recycled by ATG4B [14]. LC3-II is also essential for phagophore elongation and sealing to form autophagosomes by mediating membrane tethering [15, 16]. During autophagosome formation, the autophagic cargo is captured

either selectively (for selective autophagy such as mitophagy and aggrephagy) or non-selectively (for bulk degradation during starvation); described in Section 1.

1.2.3. Autophagosome maturation and autolysosome formation

After formation, the autophagosomes move towards the lysosome-enriched area in the perinuclear region of the cell via microtubules [17, 18]. The autophagosomes either fuse with the lysosomes directly to form autolysosomes, or they initially fuse with the late endosomes to form amphisomes and then fuse with the lysosomes to form autolysosomes. Autolysosomes are the acidic terminal autophagic vesicles wherein lysosomal acid hydrolases degrade the autophagic cargo [4]. Autophagosome maturation into autolysosomes is mediated by Rab7, ESCRTs (endosomal sorting complexes required for transport), SNAREs (N-ethylmaleimide-sensitive factor attachment protein receptors) and the class C VPS proteins [2] (**Figure 1.1**). Class III phosphatidylinositol-3-kinase complex 2 (PI3KC3-C2) consists of VPS34, Beclin 1, VPS15, and UVRAG (UV radiation resistance-associated gene protein) also facilitates autophagosome maturation through the association of UVRAG with HOPS complex for activating Rab7 [19-22]. The SNARE complex mediating membrane fusion during autophagosome maturation involves SNAP-29 (synaptosome-associated protein 29), which tethers the autophagosomal syntaxin-17 with late endosomal/lysosomal VAMP8 (vesicle-associated membrane protein 8) [23].

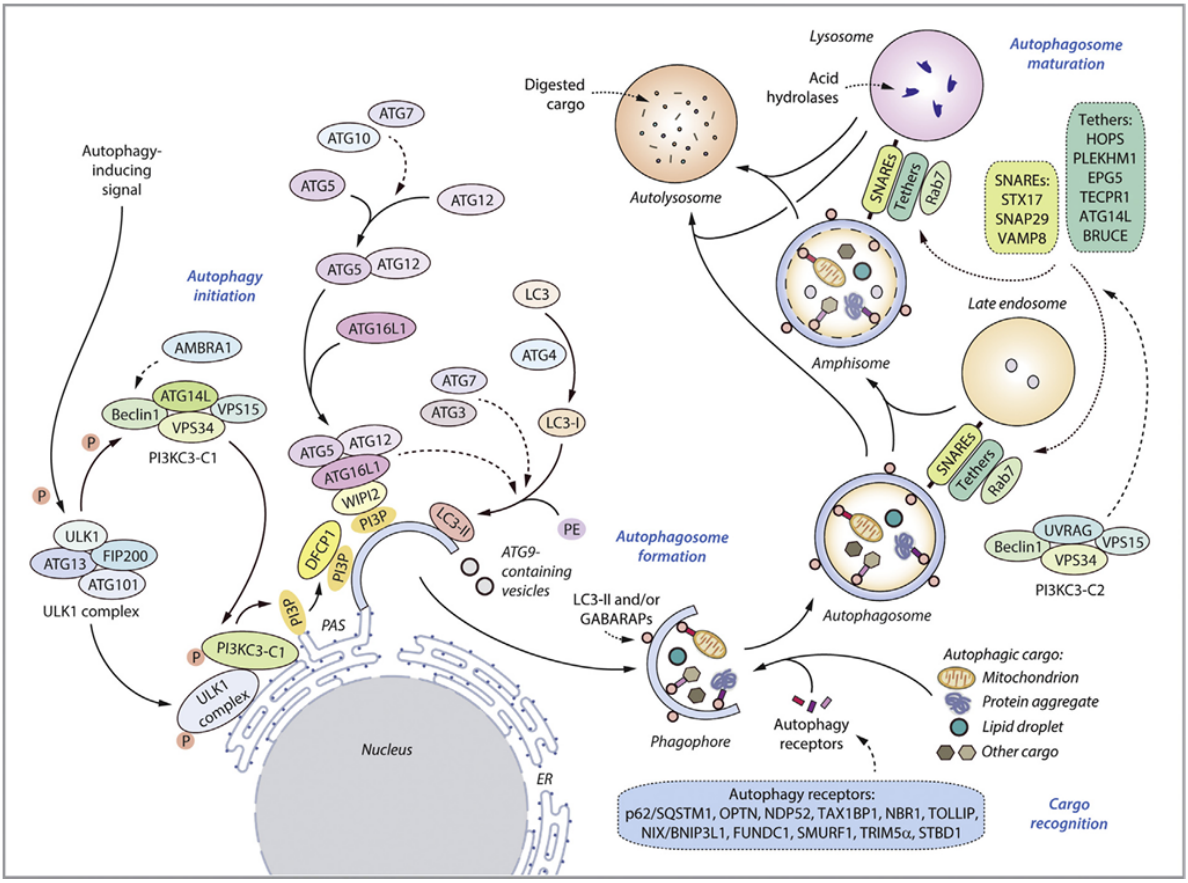

Figure 1.1 The mechanism of autophagy

The ATG proteins mediate phagophore formation, phagophore elongation and autophagosome formation. Specific autophagy receptors mediate cargo recognition for selective autophagy. Various SNAREs and tethering proteins mediate autophagosome maturation. The autophagic cargo is degraded in autolysosomes by lysosomal acid hydrolases.

Figure ref: [1] (Seranova E. et al. with Sun C. and Sarkar S. *J. Mol. Biol.* 432: 2754-2798, 2020).

1.3. Nature of autophagic degradation

Autophagy is primarily non-selective for bulk degradation, but multiple lines of evidence suggest this process can be selective for the recognition and degradation of specific cargo.

1.3.1. Non-selective autophagy

The fundamental non-selective bulk degradation of autophagic cargo is induced during fasting and starvation conditions. This process maintains cellular homeostasis and metabolic equilibrium by degrading cytoplasmic macromolecules and recycling their breakdown products like amino acids, sugars, fatty acids, and nucleosides as building blocks to generate energy and compensate for nutrients deprivation [4, 24, 25].

1.3.2. Selective autophagy

The removal of certain unwanted cellular materials, such as protein aggregates (like those associated with neurodegeneration), damaged organelles (like mitochondria) and invading pathogens (including *Mycobacteria*, *Salmonella*, and *Listeria*), require selective targeting for autophagic degradation. These cargos are usually marked by ubiquitination for enabling recognition by specific autophagic receptor proteins and subsequent targeting to the autophagosomes for degradation [26]. Based on the nature of the autophagic cargo, selective autophagy is further categorised into aggrephagy (for protein aggregates), mitophagy (for damaged mitochondria), xenophagy (for pathogens), and so on [26, 27].

For selective targeting of autophagic cargo, the autophagy receptor proteins bind to the ubiquitinated cargo via their ubiquitin-binding domain (UBD) and to the growing phagophore via their LC3- interacting region (LIR) [28, 29]. They could also interact and cooperate with each other during cargo recognition [30, 31]. For ubiquitin-dependent selective autophagy, the autophagy receptor proteins for xenophagy include p62 (SQSTM1), NDP52 (nuclear dot protein of 52 kDa) and OPTN (optineurin), and for aggrephagy include p62, NBR1 (neighbour of BRCA1 gene 1), OPTN and TOLLIP (Tollin interacting protein) [26, 27].

1.4. Regulation of autophagy by signalling pathways and small molecules

Autophagy can be activated by stress signals such as nutrient deprivation, hypoxia, growth factor depletion, oxidative stress, protein aggregation, infection, and endoplasmic reticulum (ER) stress, amongst others [32]. This process is primarily governed by the mechanistic target of rapamycin (mTOR) pathway, but can be also regulated by multiple mTOR-independent pathways (**Figure 1.2**).These pathways can be targeted by small molecules for pharmacological modulation of autophagy.

1.4.1. mTOR-dependent regulation autophagy

Autophagy is classically regulated by the mechanistic target of rapamycin (mTOR) (Figure 2), which is a serine/threonine protein kinase that exists in two distinct protein complexes: mTOR complex 1 (mTORC1) and mTOR complex 2 (mTORC2). Nutrient deprivation or starvation is one of the major stress signals that induces autophagy by inhibiting mTORC1 [33-35]. Under nutrient sufficient conditions, mTORC1 negatively regulates autophagy [14, 15]. Activated mTORC1 can directly suppress the ULK1 autophagy initiation complex via phosphorylation [8]. Moreover, mTORC1 indirectly inhibits ULK1 by phosphorylating AMBRA1 (activating molecule in Beclin 1-regulated autophagy protein 1). These events lead to impaired ULK1 kinase activity [36]. mTORC1 also suppresses autophagy by phosphorylating TFEB (transcription factor EB), causing cytoplasmic sequestration of this transcription factor that otherwise is required for lysosomal biogenesis and regulation of autophagy-related gene expression when translocated to the nucleus [37-39].

mTORC1 is regulated by several upstream factors including energy deprivation, which increases AMP/ATP ratio [4]. Increased AMP level activates AMPK (AMP-activated protein kinase), which induces autophagy by phosphorylating RAPTOR (regulatory-associated protein of mTOR) and TSC2 (tuberous sclerosis complex 2) to suppress mTORC1 activity [40-42]. Importantly, AMPK can also directly phosphorylate ULK1 and Beclin 1 (in PI3KC3 complex) to induce autophagy independently of mTORC1 [11, 43, 44]. Furthermore, mTOR is also regulated by growth factors and cytoplasmic amino acid levels to influence autophagy [4, 33, 34]. Pharmacological inhibition of mTORC1, such as with rapamycin, is the classical method for inducing autophagy [4, 45]. Other mTOR inhibitors stimulating autophagy include Torin 1 [46], as well as the analogs of rapamycin (called rapalogs) like temsirolimus (CCI-779) [47] and everolimus (RAD-001) [48].

1.4.2. mTOR-independent regulation of autophagy

Apart from influencing autophagy, mTOR has essential roles in regulating a range of vital cellular processes including gene transcription, protein translation, cell growth and proliferation [33, 35].Therefore, inhibition of mTOR is not the ideal pharmacological target for stimulating autophagy since this could result in undesirable side effects unrelated to autophagy regulation. However, autophagy is also regulated independently of mTORC1 (**Figure 1.2**), and this avenue is more clinically desirable for therapeutic exploitation of this process [4, 45]. Elevation of intracellular levels of a number of second messengers, such as IP_3 (inositol 1,4,5-trisphosphate) [49], Ca^{2+} [50, 51], cAMP (3',5'-cyclic adenosine monophosphate) [50] and NO (nitric oxide) [52], negatively regulate autophagy in mTORC1 independent manner [4]. Although IP_3, cAMP and NO inhibit autophagosome formation, Ca^{2+} has a more complex effect. Influx of extracellular Ca^{2+} suppresses autophagosome formation whereas release of stored ER Ca^{2+} prevent autophagosome maturation [49-51]; an aspect not fully elucidated. Increased cytosolic Ca^{2+} can activate calpains, which also inhibit autophagosome formation [50, 51]. Furthermore, activation of JNK1 (c-Jun N-terminal kinase 1) pathway during nutrient deprivation positively regulates autophagy independently of mTOR. Activated JNK1 phosphorylates the anti-autophagy protein Bcl-2 and prevents its interaction with Beclin-1, thereby allowing Beclin-1 to form the pro-autophagy VPS34–Beclin-1 complex for autophagy initiation [43]. The mTOR-independent autophagy pathways can be targeted at distinct stages for inducing autophagy, such as with lithium, carbamazepine and valproic acid (by reducing inositol and IP_3 levels) [49], verapamil [50] and felodipine (by lowering cytosolic Ca^{2+}) [53], rilmenidine, (by reducing cAMP levels) [50], trehalose [54, 55] and metformin (via AMPK activation) [56], L-NAME (by reducing NO levels) [52], SMER28 [57], and many others. Additionally, autophagy can be triggered by the autophagy-inducing peptide Tat-Beclin 1, and by natural compounds or nutritional supplements such as resveratrol (by activation of sirtuin 1 and mTOR inhibition) [58, 59], spermidine (by upregulating ATG gene expression) [60] and vitamin D3 (by upregulating Beclin 1 and ATG expression) [61, 62].

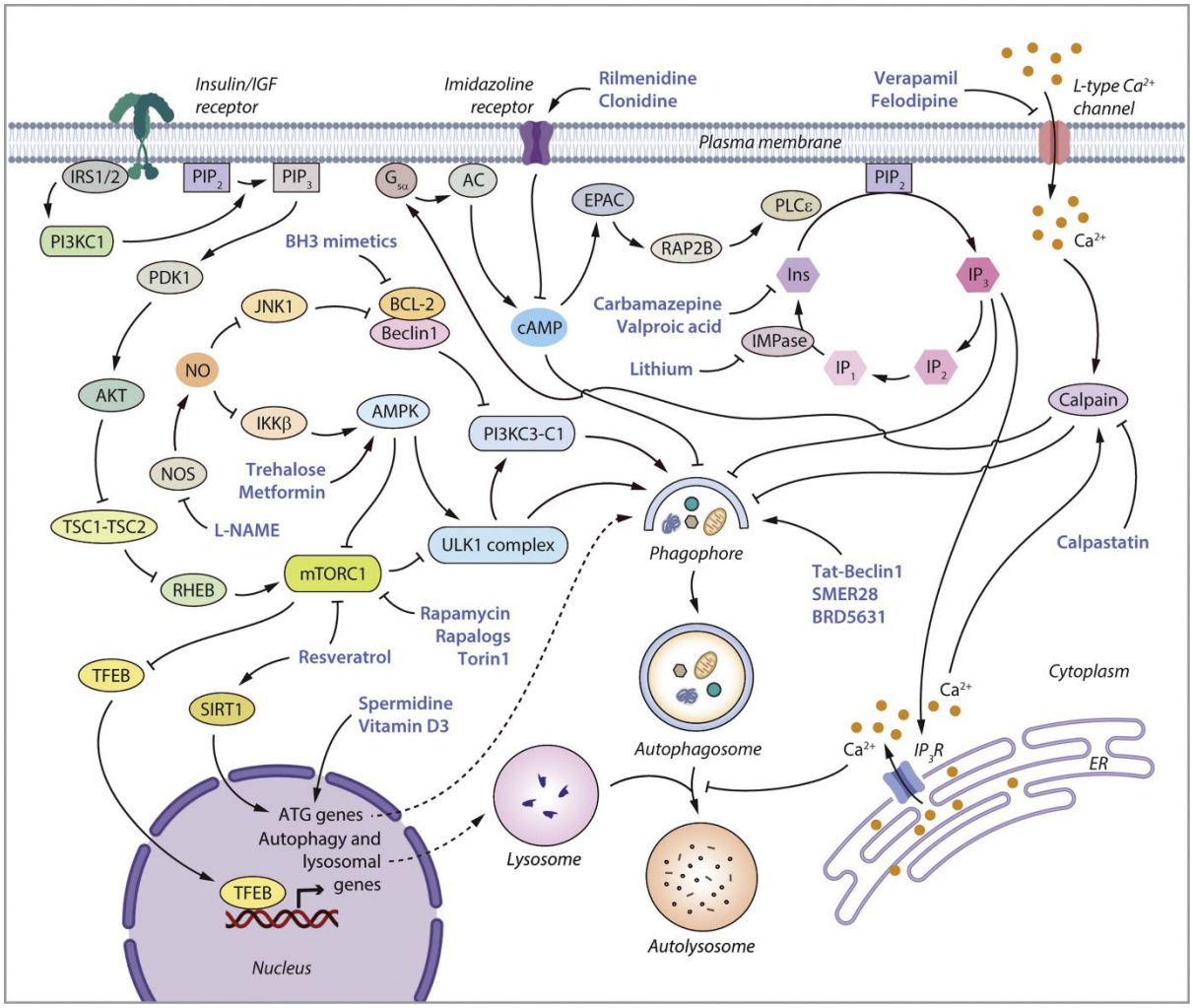

Figure 1.2 The signalling pathway regulating autophagy.

Regulation of autophagy by signaling pathways and small molecules. Autophagy is regulated by the mTOR pathways and various mTOR-independent signaling pathways. These pathways can be targeted by chemical compounds for stimulating autophagy that has potential biomedical applications in diverse human diseases.

Figure ref: [1] (Seranova E. et al. with Sun C. and Sarkar S. *J. Mol. Biol.* 432: 2754-2798, 2020).

1.5. Methods for monitoring autophagy

Multiple methods have been described for monitoring autophagy and assessing autophagic flux. These include assays related to autophagosome (LC3) turnover and autophagic cargo (p62) clearance (**Figure 1.3 A**). The primary autophagy method generally used for chemical and genetic screens involves LC3-based reporters.

1.5.1. Assays based on autophagosome turnover using LC3 reporters

The properties of LC3 described in section 1.1.2 make it an indicator of the changes in autophagosomes and autolysosome numbers and thus used routinely as a marker of autophagy. Fluorescent-tagged LC3 reporters such as GFP-LC3 [16] and mRFP-GFP-LC3 [63] have been extensively used to study autophagy regulation and for genetic or chemical screening.

1.5.1.1. GFP-LC3 reporter

For assays involving GFP-LC3, the number of GFP^+ puncta is quantified in each cell to measure the changes in steady-state autophagosome number. This reporter has been widely utilized for screening purposes because of its simplicity in measuring the readout. With this reporter, autophagy inducers and blockers will increase GFP-LC3 puncta whereas autophagy inhibitors will decrease GFP-LC3 puncta (**Figure 1.3 B**). Despite the benefits of the GFP-LC3 readout-based screening method, the reporter has a significant disadvantage in that it is unable to distinguish between autophagosomes and autolysosomes. Thus, GFP-LC3 reporter cannot distinguish between autophagy inducer versus autophagy blocker because both scenarios can increase the number of autophagosomes. Autophagy inducers increase autophagosome numbers by enhancing formation at the early stage, whereas autophagy blockers cause the accumulation of autophagosomes by preventing their maturation at the late stage [64]. Hence, GFP-LC3 based screen alone cannot fully characterize the autophagy modulators, and thorough secondary assays are essential for further validating the hits identified in GFP-LC3 based screen (for example, assays for autophagic substrate clearance, and assays for autophagosome biogenesis and maturation) [65, 66].

1.5.1.2. mRFP-GFP-LC3 or mCherry-EGFP-LC3 reporters

Tandem fluorescent-tagged LC3 reporters such as mRFP-GFP-LC3 are pH-sensitive, and can compensate for the shortfall of GFP-LC3 reporter. The mRFP-GFP-LC3 reporter is sensitive to the lysosomal acidic environment, and this property allows the distinction between the autophagosomes and the autolysosomes. In this system, the autophagosomes appear yellow due to the emission of both red (mRFP) and green (GFP) signals. After the lysosomal fusion of autophagosomes, the GFP signal is quenched in the acidic environment of the autolysosomes that emit only red (mRFP) signal [63]. For fluorescent image-based analysis in screening, mRFP and GFP puncta are quantified in each cell to evaluate the perturbations in the number of autophagosomes ($mRFP^+/GFP^+$) and autolysosomes ($mRFP^+/GFP^-$). Autophagy inducers or inhibitors will increase or decrease autophagosomes and autolysosomes, respectively, whereas autophagy blockers will increase autophagosomes but decrease autolysosomes (**Figure 1.3 B**). This readout can be improved by making mCherry-EGFP-LC3 reporter by substituting mRFP/GFP with more photostable mCherry [31] and EGFP (Enhanced GFP) that have higher sensitivity and brighter fluorescence [67]. Furthermore, these reporters can be used as a secondary assays for the hits from the primary GFP-LC3 screen.

1.5.2. Assays based on autophagic substrate clearance

Apart from the LC3-based reporters, assays measuring autophagic substrate degradation can also be used as an indicator of autophagic flux (**Figure 1.3 A**). The autophagic substrates include neurodegeneration-associated aggregation-prone proteins such as mutant huntingtin or α-synuclein, or the more widely-used specific substrate, p62/SQSTM1 [30, 31]. These readouts are either analyzed by immunoblotting or imaging of fluorescent-tagged reporters [68]. However, this method will not be able to distinguish between autophagy inhibitors versus autophagy blockers and are generally used as a secondary assay for assessing autophagic flux [66].

A

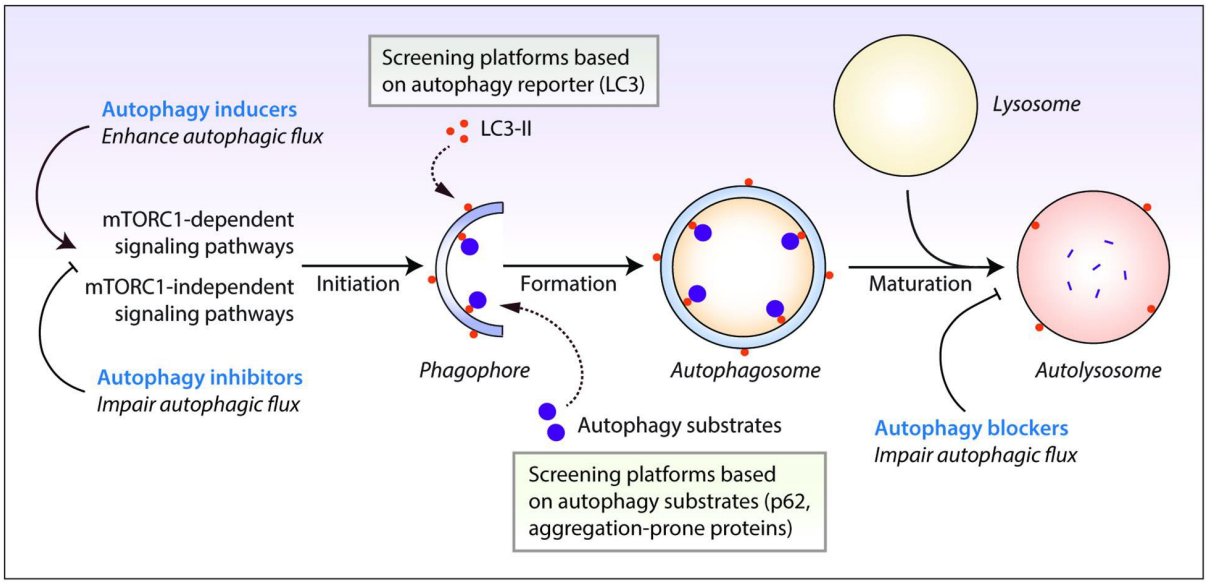

B

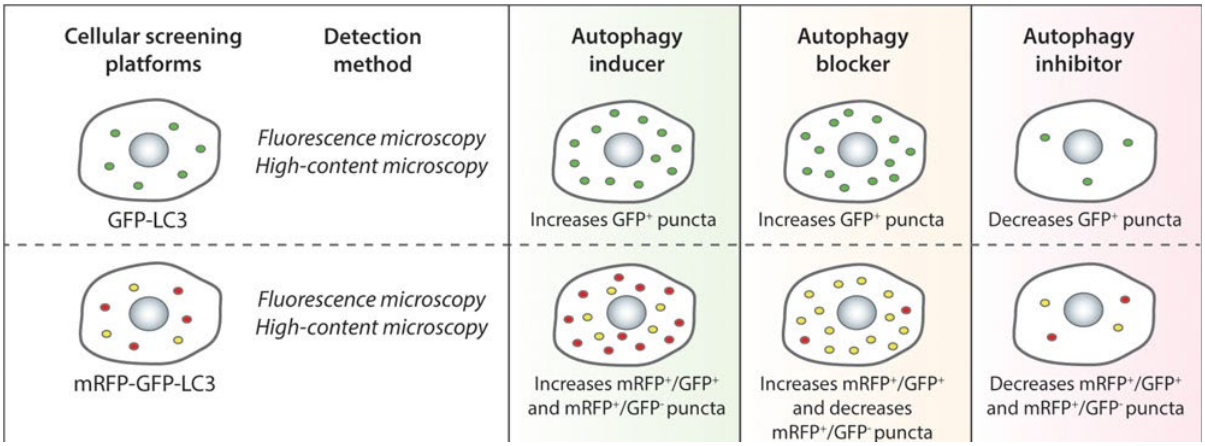

Figure 1.3. Chemical screening methods using LC3-based autophagy reporters for identifying autophagy modulators in mammalian cells.

(A) Screening platforms based on LC3 and autophagy substrate reporters.

(B) LC3-based autophagy reporters such as GFP-LC3 and mRFP-GFP-LC3. The detection methods for the respective reporters and the expected readouts for autophagy inducers, blockers or inhibitors are indicated.

Figure Ref: [69] (Panda P.K. et al. and Sarkar S. *Front. Cell Dev. Biol.* 7: 38, 2019).

1.6 The role of autophagy and NAD in cellular metabolism and ageing

The process of autophagy involves the degradation of cellular macromolecules like proteins, lipids, and carbohydrates. The resulting breakdown products, such as amino acids, fatty acids, and sugar molecules, are reused as inputs into various biosynthetic pathways to provide energy during the starvation period [32, 70, 71] (**Figure 1.4**). Failure of autophagy to contribute to metabolic homeostasis could cause metabolic stress [70, 71]. Given its catabolic nature and its connection to nutrient status, autophagy exerts a significant influence on cellular metabolism [71]. However, growing evidence shows that metabolites can control autophagy through a feedback mechanism [72]. Leucine, arginine, and glutamate are commonly known as activators of the mTOR complex 1 (mTORC1). When these amino acids are deprived, mTORC1 activity is suppressed, leading to the initiation of autophagy [73]. Importantly, research has shown a link between ageing and a decrease in mouse longevity caused by continuous mTORC1 activation brought on by impaired nutrition sensing [73]. Furthermore, the polyamine spermidine has been demonstrated to extend the lifespan of eukaryotic organisms by directly enhancing autophagy, thereby implicating the metabolite in the processes of ageing and longevity [74].

The process of ageing and neurodegeneration is associated with a decline in autophagy function that is accompanied by metabolic perturbations [2]. One of the metabolites that is also depleted in these contexts is nicotinamide adenine dinucleotide (NAD), which plays a vital role in a range of cellular processes like energy metabolism, cell signalling, and DNA repair [2, 75, 76]. The redox interaction between its oxidised form (NAD^+) and its reduced form (NADH) allows NAD to function as a cofactor for oxidoreductase enzymes that are vital for several important metabolic pathways, such as glycolysis, the tricarboxylic acid cycle, and oxidative phosphorylation (OXPHOS) [77]. The intracellular NAD pool is distributed between various subcellular locations, including the mitochondria, cytosol, and nucleus [78]. It is hypothesised that the spatial distribution of NAD exerts regulation over local protein modification and organellar function [78].

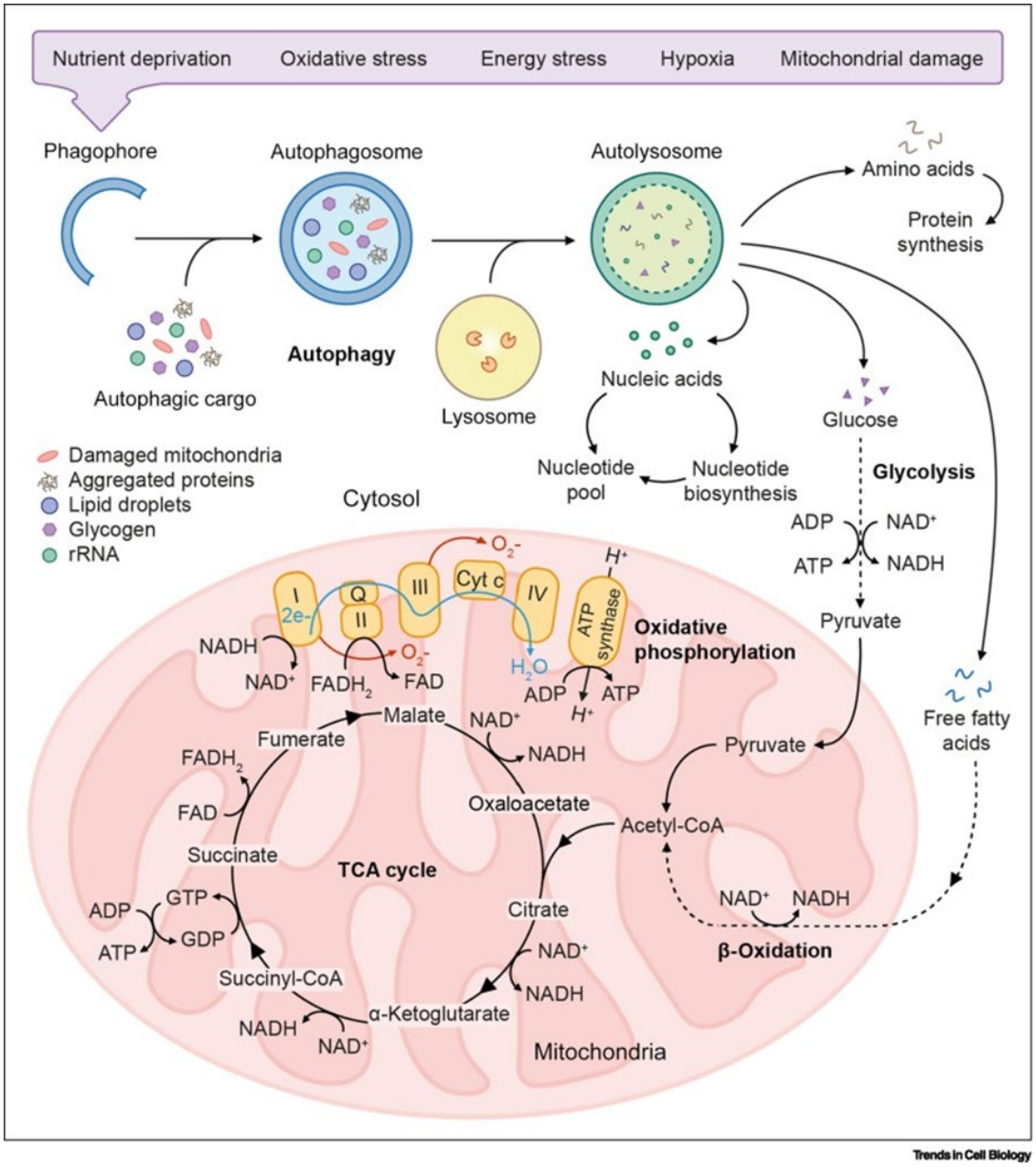

Figure 1.4. The role of autophagy in the maintenance of metabolic homeostasis.

Autophagy is activated in cells by numerous stimuli, from nutrient deprivation to mitochondrial damage. This triggers the formation of a phagophore, which extends into a sealed double-membraned autophagosome. During this process, macromolecules are selectively engulfed into autophagosomes and are subsequently degraded following fusion with lysosomes. The breakdown products of cargo degradation are released from autolysosomes to be reutilised by the cell to fuel various metabolic pathways. Notably, glucose and free fatty acids liberated by autophagy feed into the TCA cycle and oxidative phosphorylation to support mitochondrial ATP generation, particularly during cellular energy crisis. This process maintains metabolic homeostasis during cellular stress to support cell viability.

Figure ref: [2] (Wilson N. et al. with Sun C. and Sarkar S. *Trends Cell Biol.* 33: 788-802, 2023).

Declining levels of autophagy and NAD are considered to be contributing factors in the development of ageing and age-related diseases [79, 80]. It has been demonstrated that the independent enhancement of autophagy or intracellular NAD pools can facilitate the promotion of eukaryotic health and lifespan extension, as evidenced in yeast and murine models [81-83]. It is also established that NAD replenishment has the capacity to normalise cellular function by virtue of its ability to directly enhance autophagy [84-86]. Specifically, the autophagic clearance of impaired mitochondria promoted by NAD metabolism has been associated with enhanced health and longevity for several years [75, 76, 87-89]. In conclusion, the processes of autophagy and the metabolism of NAD are mutually dependent for optimal cellular function. Nevertheless, the mechanisms underlying this apparently bidirectional relationship remain poorly characterised.

1.7. Role of autophagy in human diseases

Because of the vital role of autophagy in maintaining cellular homeostasis and survival, dysfunction of autophagy leads to cytotoxicity and is thus implicated in the pathology of diverse human diseases including neurodegeneration, infectious diseases and cancer [90-93]. Multiple studies have demonstrated that autophagy is impaired in myriad diseases, particularly in several neurodegenerative diseases, whereas pharmacological upregulation of autophagy is considered a potential treatment strategy [93, 94]. Hence, therapeutic manipulation of autophagy is of immense biomedical relevance.

1.7.1. Role of autophagy in neurodegenerative diseases

Autophagy is vital for neuronal homeostasis, and the neurons are particularly susceptible to cell death underlying autophagy dysfunction because they are post-mitotic. Impairment in autophagy contributes to the insufficient clearance of neurodegeneration-associated aggregation-prone proteins and damaged organelles. This causes these toxic materials to accumulate and contribute to cytotoxicity [95, 96]. However, the molecular mechanisms of how defective autophagy contributes to neurotoxicity are not fully elucidated.

Autophagy dysfunction has been reported in multiple neurodegenerative conditions such as Alzheimer’s disease (AD), Parkinson’s disease (PD), Huntington’s disease (HD) and amyotrophic lateral sclerosis (ALS) [1, 95, 97], and also in certain neurodegenerative lysosomal storage disorders like neuronal ceroid lipofuscinosis (NCL), Gaucher disease

(GD) and Niemann-Pick type C1 (NPC1) disease [1]. The pathological protein aggregation is a key pathological hallmark of a variety of neurodegenerative diseases [98-102]. Selective clearance of protein aggregates via aggrephagy is the major degradation route of various aggregation-prone proteins associated with neurodegeneration, and thus, impairment of autophagy will lead to the accumulation of these undesirable protein aggregates that reduce neuronal viability [103, 104]. For example, mutant huntingtin (in HD), α-synuclein (in PD) and Tau (AD) are autophagy substrates, whereas the buildup of these proteins in neurons correlates with neurotoxicity [105].

Another hallmark of the pathogenesis of some common neurodegenerative diseases is the impairment in mitochondrial function. Multiple studies have reported mitochondrial dysfunction in common neurodegenerative diseases like AD, PD, and in certain rare neurodegenerative and lysosomal storage diseases [106]. Mitochondria have crucial roles in regulating bioenergetics, ion homeostasis, metabolism, and apoptosis. They also establish dynamic connections with other cellular organelles [107]. When mitochondria is damaged, it is removed from the cell via mitophagy (autophagic degradation of mitochondria) to ensure cell survival. PD-associated mutant proteins like PINK1 and PARKIN can directly impair mitophagy, whereas malfunction in the general autophagic flux will also retard mitophagy [108, 109]. Accumulation of damaged mitochondria due to problems in mitophagy can contribute to mitochondrial dysfunction and oxidative stress [110].

1.7.2. Role of autophagy in Wolfram Syndrome

Apart from autophagy studies in a range of neurodegenerative diseases mentioned above, unpublished data from Sarkar lab suggest autophagy is also defective in Wolfram syndrome 1 (WS), which is a rare, early-onset neurodegenerative disease. WS is an autosomal recessive condition characterised by diabetes insipidus (DI), diabetes mellitus (DM), optic atrophy (OA), and deafness (D); therefore, also known as DIDMOAD syndrome [111-114]. The epidemiology of WS1 is 1:770,000 in adults [115] and 1:500,000 [116] in children in the UK.

The pathogenesis of WS is associated with mutations in the *WFS1* gene located on chromosome 4p16 [117].The *WFS1* gene encodes the transmembrane protein called wolframin. In brain tissues such as the hippocampus, wolframin protein is highly expressed [118]. Wolframin is located in the mitochondria-associated ER membranes

(MAM), and is involved in posttranslational protein modification, folding, and assembly [119, 120]. Hence, it has important physiological roles in membrane trafficking, secretion, processing, and the regulation of ER Ca^{2+} homeostasis. *WFS1* mutations lead to ER dysregulation, which results in misfolded protein accumulation, an increase in ER stress level and stress-induced apoptosis in the human tissue [121]. The accumulation of potentially toxic misfolded protein is one of the major hallmarks of common neurodegernative disease phenotype [98-102]. In WS, this will induce unfolded protein response (UPR) to counteract the ER stress and restore the ER homeostasis [122, 123]. In healthy individuals, the UPR, ER-associated degradation (ERAD), ER-phagy (autophagic degradation of ER fragments) and aggrephagy function to eliminate the accumulated protein aggregates and prevent the cells from dying. [124, 125]. Coversely, autophagy dysfunction as seen in many common neurodegenerative diseases will result in the failure in the clearance of misfolded protein aggregates and alleviation of ER stress [1]. The UPR then triggers a cascade of downstream events via multiple signalling pathways, leading to apoptosis and altering neuronal activity [120, 121].

Additionally, mutations in the MAM-associated protein WFS1 in WS also contributes to mitochondrial dysfunction involving altered mitochondrial dynamics, mitochondrial depolarization, decreased mitochondrial respiration, less ATP production, and oxidative stress [126]. Notably, malfunction of MAM has been linked to the development of various neurodegenerative disorders such as AD and PD [127].

1.8. Human pluripotent stem cell-based platforms for studying autophagy and drug development

Multiple lines of evidence indicate cell type specificity of autophagy modulators and that many of them identified in immortalized or non-human cell lines might not produce the same therapeutic efficacy in the target human cell types under specific disease conditions [1]. Therefore, experimental platforms with human relevance are needed for studying the homeostatic role of autophagy at a fundamental level and for identifying cell-specific or potent autophagy modulators for biomedical applications. The use of human embryonic stem cell (hESC) and patient-derived induced pluripotent stem cell (iPSC) models for undertaking basic science and drug discovery in a manner relevant to human biology is gaining attention in recent years. This is due to two important characteristics of hESCs

and iPSCs: (i) self-renewal – ability to proliferate without immortalization; (ii) pluripotent – ability to differentiate into all three embryonic germ layers and generate different somatic cell types [128]. The hESCs are derived from the inner cell mass of blastocyst-stage embryos, whilst the iPSCs are derived from healthy individuals or disease patients via cellular reprogramming. The above characteristics of these pluripotent stem cells enable us to generate physiological or disease-affected cellular platforms for research [1]. Using this experimental system, in-depth studies of biological processes such as autophagy can be undertaken in various human cell types, such as neuronal and glial cells (for neurodegenerative diseases) [129-131], macrophages (for infectious diseases) [132], hepatic cells (for liver diseases) [133], amongst others (**Figure 1.5**).

Furthermore, an important aspect of these human pluripotent stem cells is their ability to be genome engineered for creating reporter or knockout models to study biological pathways or gene functions. For instance, Sarkar lab has generated autophagy reporter (mCherry-EGFP-LC3; unpublished) and autophagy knockout (*ATG5*$^{-/-}$) [134] hESC lines can be differentiated into various human cell types of interest with an isogenic background, thus allowing the study of any cell type-specific effects.

An important step in the development of targeted therapies is to understand the molecular mechanisms underlying pathology. iPSC-based disease models can provide a pre-clinical platform for studying disease mechanisms and evaluating drug candidates in patient-derived disease-affected cells. Therefore, the advancements in human stem cell technology enable the generation of appropriate experimental platforms for studying fundamental biology relevant to humans and for compound screening to identify candidate drugs that will be effective in the target organs of the patients [135, 136]. Many studies have utilised iPSC models of neurodegenerative diseases to study autophagy and assess the therapeutic efficacy of autophagy inducers in a range of neurodegenerative disease neuronal cells [1]. From a biomedical perspective, pharmacological upregulation of autophagy has been advantageous in various transgenic neurodegenerative disease models. This is achieved by enhancing the clearance of mutant proteins and rescuing disease-relevant phenotypes. [95, 137]. Both mTOR-dependent (rapamycin) and mTOR-independent autophagy inducers (trehalose, carbamazepine, rilmenidine, felodipine, SMER28, and many others) rescued disease phenotypes in transgenic mouse and patient-derived induced pluripotent stem cell (iPSC) models of a number of neurodegenerative conditions including HD [47, 50, 53, 57, 138, 139], AD [140-144], PD

[145-148], ALS [149, 150] and NPC1 disease [69, 151]. Therefore, modulation of autophagy has a great potential for therapeutic interventions in certain neurodegenerative and lysosomal storage diseases.

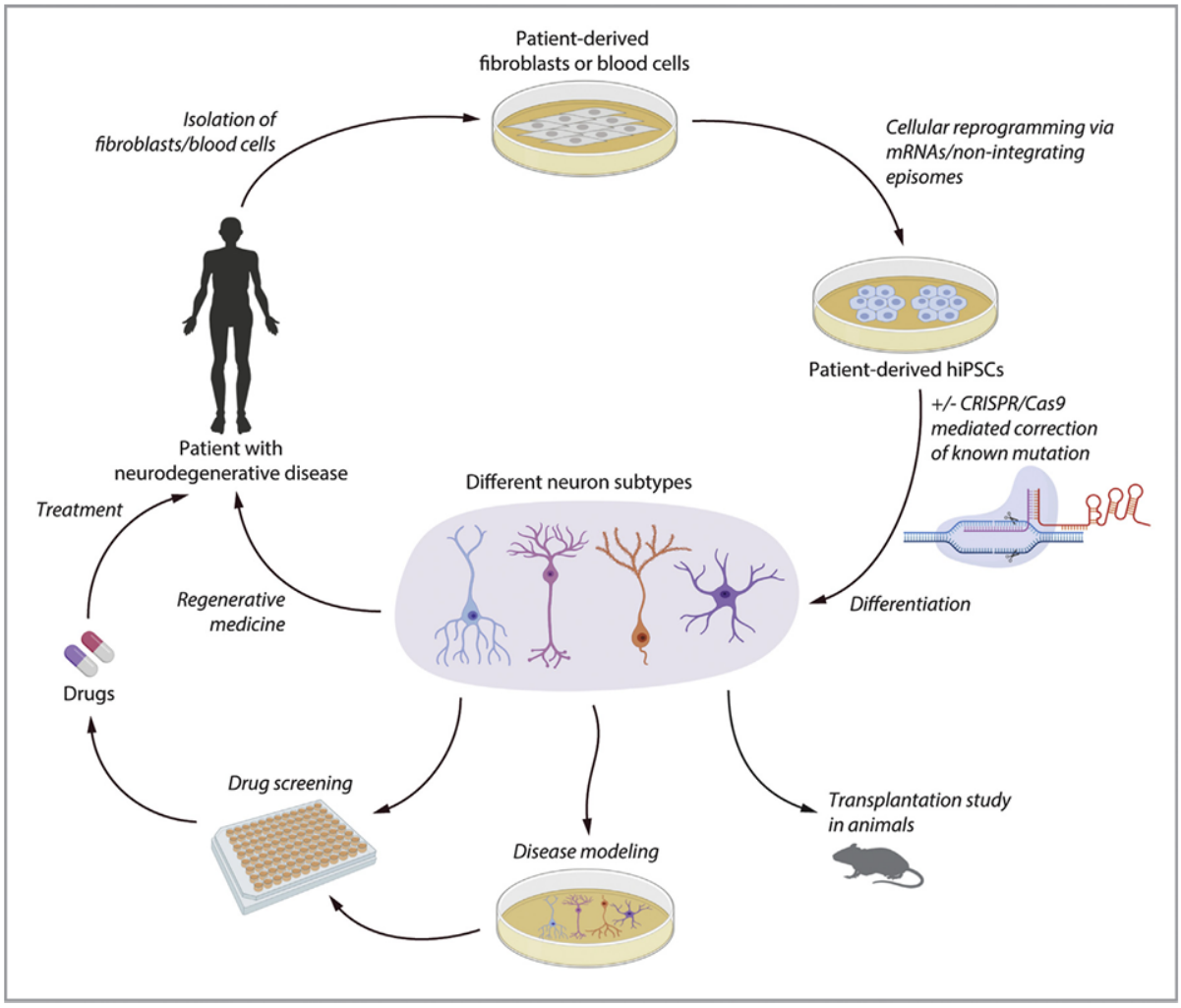

Figure 1.5 The application of a hiPSC-based platform in studying autophagy, disease modelling and drug discovery. Autophagy enables the acquisition of somatic cells from patients with metabolic diseases, which can then be converted into human induced pluripotent stem cells hiPSCs. hiPSCs are subsequently transformed into specific cell types relevant to the condition, such as neurons, to create models for studying neurodegenerative diseases. These cells can be cultivated in two or three dimensions for modelling purposes, implanted into animals, and then go through a high-throughput screening process to find new drugs.

Figure ref: [1] (Seranova E. et al. with Sun C. and Sarkar S. *J. Mol. Biol.* 432: 2754-2798, 2020).

1.9 Aims and Objectives

The aims of this study are to investigate the homeostatic role of autophagy in neuronal survival, and to develop therapeutic interventions for neurodegenerative diseases associated with autophagy dysfunction. To undertake the study in a manner relevant to human biology, human pluripotent stem cell-based experimental platforms have been utilised for fundamental and biomedical science.

The objectives to achieve the aim of this study are as follows:

(1) Investigate the cell death mechanisms underlying autophagy deficiency in hESC-derived neuronal cells [related to Chapter 2].

(2) Develop therapeutic intervention for a rare neurodegenerative disease called Wolfram Syndrome using hiPSC-derived neuronal cells [related to Chapter 3].

(3) Identify FDA-approved autophagy-inducing drugs for drug repurposing in rare neurodegenerative diseases using hESC- and hiPSC-derived neuronal cells [related to Chapter 4].

Chapter 2:

NAD depletion mediates cytotoxicity in human neurons with autophagy deficiency

Chapter 2: NAD depletion mediates cytotoxicity in human neurons with autophagy deficiency

The work presented in this chapter has previously been published in my first-author research paper where I generated the majority of the data:
Sun C, Seranova E, Cohen MA et al. and Sarkar S. NAD depletion mediates cytotoxicity in human neurons with autophagy deficiency. Cell Rep. 42(5): 112372 (2023) [134].

2.1. Introduction

Autophagy is a catabolic process that plays a fundamental role in cellular and energy homeostasis via the clearance of undesirable macromolecules and organelles and via the utilization of the breakdown products in metabolic pathways [70, 71, 152]. These functions of autophagy are vital for cell survival and pertinent for postmitotic cells like neurons where the damaged cellular components are not diluted by cell proliferation [153].Genetic studies in mouse models demonstrated that brain-specific abrogation of basal autophagy by inducible knockout of essential autophagy genes like *Atg5* or *Atg7* causes neurodegeneration [154, 155], implying that basal autophagy is essential for neuronal homeostasis.

Similarly in other organisms, suppression of autophagy by deletion or downregulation of *atg5* reduced the lifespan in *Drosophila melanogaster* and the survival in *Saccharomyces cerevisiae* under starvation conditions [156, 157], Indeed, dysregulation of autophagy has been reported in myriad human diseases including neurodegenerative and lysosomal storage disorders, where defective autophagy is implicated as a contributing factor to the disease pathology [1, 4, 94-96, 158]. Despite the biomedical importance of autophagy in pathological contexts including neurodegeneration, it is not clear how malfunction of autophagy causes cytotoxicity. In order to mechanistically elucidate this causal link in a manner relevant to human biology, we established human cellular platforms with autophagy deficiency by utilizing human embryonic stem cells (hESCs). Unlike immortalized cells, the hESCs provide a more physiologically relevant in vitro experimental system because they are capable of self-renewal and also, being pluripotent, are able to differentiate into a range of human cell types like neurons [159, 160].

2.2. Objectives

(1) Generate and characterise of hESC-based cellular platforms with autophagy deficiency.
(2) Elucidate the mechanism of cell death in hESC-derived neurons with autophagy deficiency.
(3) Determine pharmacological means of improving cell survival in autophagy-deficient human neurons.

2.3. Results

2.3.1. Generation and characterisation of autophagy-deficient hESCs

Loss of autophagy can be achieved by knockout of *ATG5*, which encodes for a key protein required for autophagosome formation [161]. Autophagy-deficient (*ATG5*$^{-/-}$) hESCs were previously generated by Haoyi Wang and Sovan Sarkar by knockout of *ATG5* exon 3 via genome editing with transcription activator-like effector nucleases (TALENs) (**Figure 2.1 A, B**). Various homozygous (*ATG5*$^{-/-}$) and heterozygous (*ATG5*$^{+/-}$) knockout clones were obtained (**Figure 2.1 C**), which expressed pluripotency markers (**Figure 2.2 A-C**) and maintained proliferative capacity (**Figure 2.2 D, E**) comparable to wild-type (*ATG5*$^{+/+}$) hESCs.

Since ATG5 protein normally exists in conjugation with ATG12 [162], immunoblotting analysis revealed complete or partial loss of the ATG5-ATG12 conjugate in *ATG5*$^{-/-}$ and *ATG5*$^{+/-}$ hESCs, respectively (**Figure 2.3 A**). Loss of autophagy was demonstrated under basal and starvation conditions in multiple clones of *ATG5*$^{-/-}$ hESCs via the absence of autophagosomes (lack of LC3^{+} puncta, LC3-II levels or autophagic vacuoles) and an accumulation of autophagy substrate (increased p62 levels). Moreover, starvation-induced autophagy was observed in wild-type but not in *ATG5*$^{-/-}$ hESCs. (**Figure 2.3 A-D**). Next, the impact of loss of autophagy on cell survival in hESCs was studied. Increased apoptosis in *ATG5*$^{-/-}$ hESCs was evident from elevated levels of luminescence-based cytotoxicity assay under normal growth conditions (**Figure 2.3 E**), indicating that autophagy deficiency impairs cell viability in hESCs.

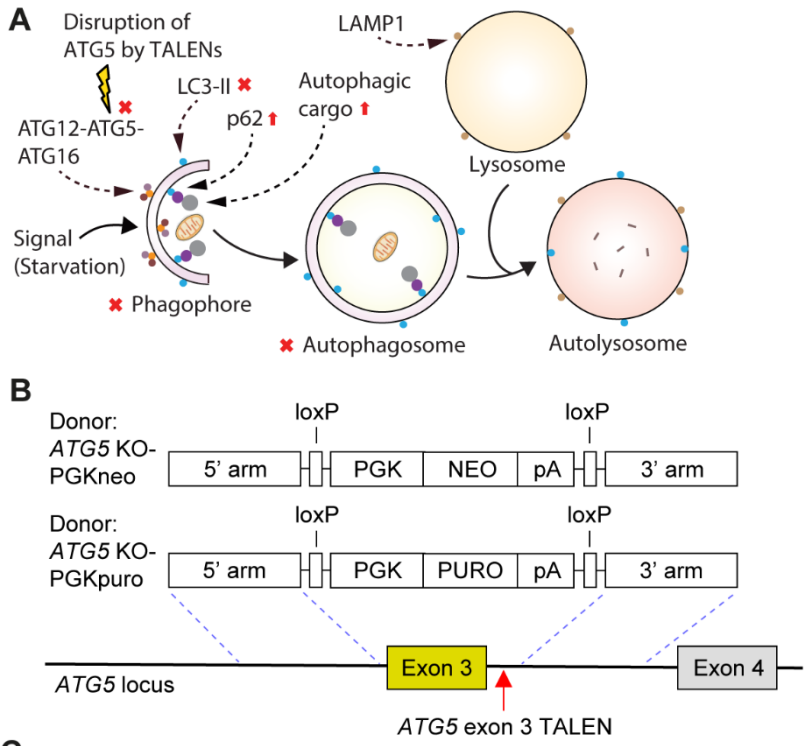

C

Overview of parental and autophagy-deficient hESC lines

WIBR3 hESC lines	*Genotype for ATG5 knockout*	*Autophagy*	*Cell line designation with clone ID*
WIBR3 hESC *ATG5*$^{+/+}$	Wild-type	Yes	WIBR3
WIBR3 hESC *ATG5*$^{+/-}$	Heterozygous	Yes	WIBR3-ATG5$^{+/-}$ #1, #2
WIBR3 hESC *ATG5*$^{-/-}$	Homozygous	No	WIBR3-ATG5$^{-/-}$ #1, #3, #4, #5, #6

Figure 2.1. Generation of autophagy-deficient (*ATG5*$^{-/-}$) hESCs.

(A) Schematic representation of the impact of *ATG5* gene knockout on abrogation of autophagy.

(B) Targeting strategy in hESCs for deleting exon 3 in human *ATG5* gene by TALENs.

(C) List of autophagy-deficient hESC lines generated by genome editing in parental WIBR3 hESCs.

The autophagy-deficient hESC lines were generated by Haoyi Wang and Sovan Sarkar.

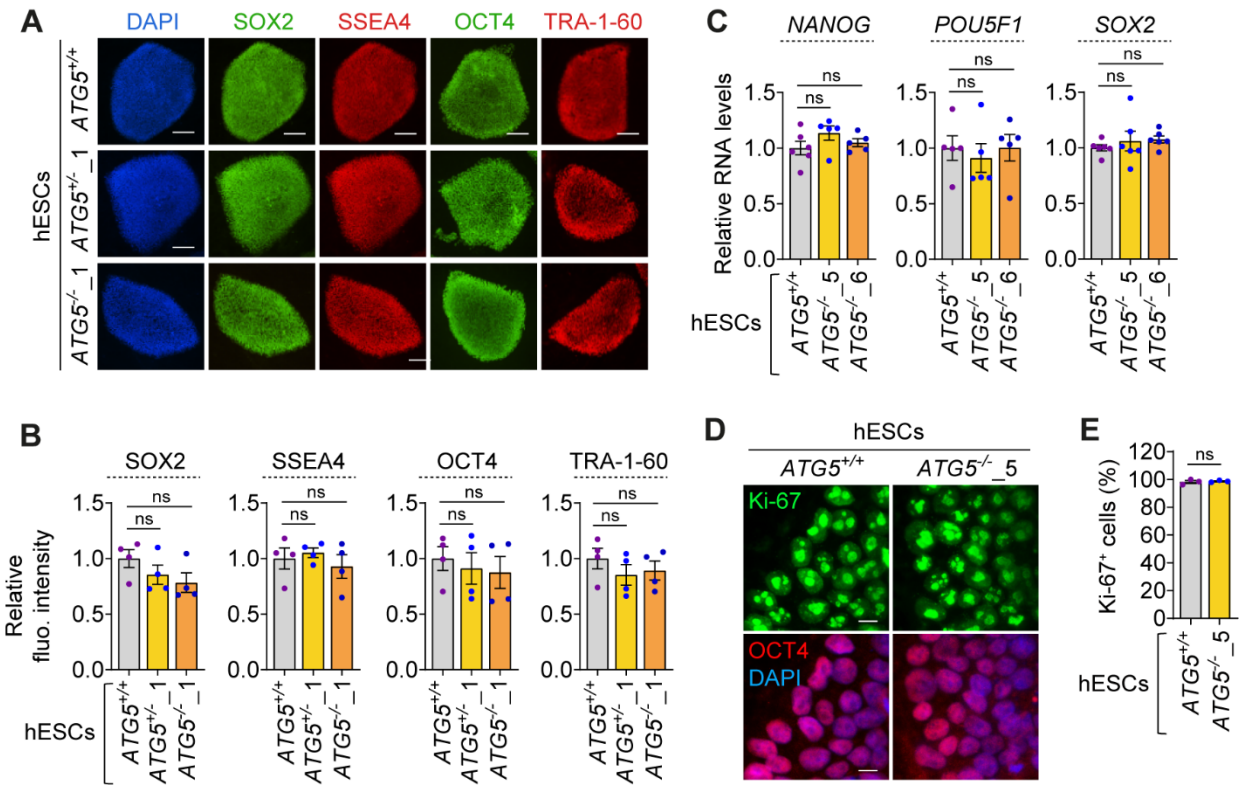

Figure 2.2. *ATG5*$^{-/-}$ hESCs exhibit pluripotency and maintain proliferative capacity.

(A) Immunofluorescence images of SOX2, SSEA4, OCT4, and TRA-1-60 in *ATG5*$^{+/+}$, *ATG5*$^{+/-}$_1, and *ATG5*$^{-/-}$_1 hESCs, cultured in full growth medium. *Data generated with Elena Seranova.*

(B) Quantification of fluorescence intensity relative to hESC colony area of SOX2, SSEA4, OCT4 and TRA-1-60 (as in Figure 2.2A) in *ATG5*$^{+/+}$, *ATG5*$^{+/-}$_1 and *ATG5*$^{-/-}$_1 hESCs.

(C) Quantitative RT-PCR expression analyses of *NANOG*, *POU5F1* (*OCT4*) and *SOX2* relative to *GAPDH* in *ATG5*$^{+/+}$, *ATG5*$^{-/-}$_5 and *ATG5*$^{-/-}$_6 hESCs.

(D, E) Immunofluorescence images of Ki-67 and OCT4 (D) and quantification of Ki-67^{+} cells (E) in *ATG5*$^{+/+}$ and *ATG5*$^{-/-}$_5 hESCs.

Graphical data are mean ± SEM of n = 3–6 biological replicates as indicated. P values were calculated by one-way ANOVA followed by multiple comparisons with two-stage linear step-up procedure of Benjamini, Krieger, and Yekutieli on 3 independent experiments (B and C) or unpaired two-tailed Student's t-test (E). ∗∗∗p < 0.001; ∗∗p < 0.01; ∗p < 0.05. Scale bars: 200 µm (A), 10 µm (D).

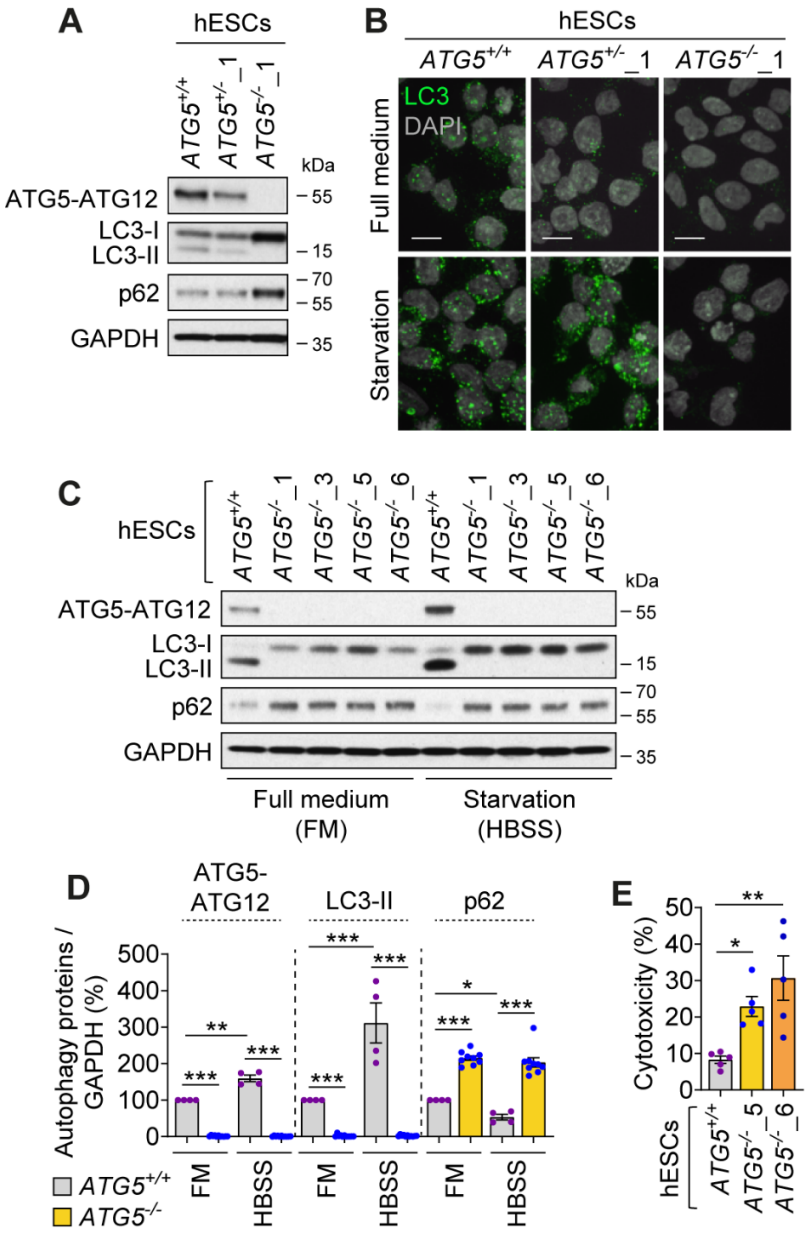

Figure 2.3. Loss of autophagy and increased cell death in *ATG5*$^{-/-}$ hESCs.

(A) Immunoblotting analyses of ATG5, LC3, p62 in *ATG5*$^{+/+}$, *ATG5*$^{+/-}$_1 and *ATG5*$^{-/-}$_1 hESCs, cultured either in full growth medium.

(B) Immunofluorescence images of LC3 puncta in *ATG5*$^{+/+}$, *ATG5*$^{+/-}$_1 and *ATG5*$^{-/-}$_1 hESCs cultured in full growth medium (FM) or starvation condition (HBSS for 3 hours).

(C, D) Immunoblotting analyses of ATG5, LC3, and p62 in *ATG5*$^{+/+}$, *ATG5*$^{+/-}$_1 and *ATG5*$^{-/-}$_1 hESCs cultured in full growth medium (FM) or starvation condition (HBSS for 3 hours).

(E) Cytotoxicity assay in *ATG5*$^{+/+}$, *ATG5*$^{-/-}$_5, and *ATG5*$^{-/-}$_6 hESCs.

Graphical data are mean ± SEM of n = 3–11 biological replicates as indicated. P values were calculated by one-way ANOVA followed by multiple comparisons with two-stage linear step-up procedure of Benjamini, Krieger, and Yekutieli on 3 independent experiments (D and E). ∗∗∗p < 0.001; ∗∗p < 0.01; ∗p < 0.05. Scale bar: 100 μm (B). *Data in this figure partially generated with Elena Seranova.*

2.3.2. Autophagy-deficient human neurons manifest with elevated cell death

After establishing a causal link between loss of autophagy and cell death in hESCs, human neuronal cells with autophagy deficiency were next generated to investigate whether and how loss of autophagy affects neuronal survival. *ATG5*$^{+/+}$ and multiple clones of *ATG5*$^{-/-}$ hESCs were differentiated into neural precursors (NPs) via the 'dual-SMAD inhibition method' followed by neuronal differentiation (**Figure 2.4 A**), as previously described [163]. The NPs derived via this method carry an anterior identity and commit to forebrain fates when cultured in the presence of bFGF and EGF [164]. The cellular identity of hESC-derived NPs and neurons was confirmed by the expression of their cell-specific markers, which were comparable between the wild-type and *ATG5*$^{-/-}$ cells (**Figure 2.4 B, C**).

Autophagy deficiency was confirmed in *ATG5*$^{-/-}$ hESC-derived NPs and neurons via the lack of ATG5-ATG12 conjugate and LC3-II levels/puncta, as well as p62 accumulation (**Figure 2.5 A-D**). Increased cytotoxicity was observed in *ATG5*$^{-/-}$ neurons as early as 2 weeks of neuronal differentiation, and this was more substantial after 4 weeks (**Figure 2.5 E**). Altogether, the cell death phenotypes in autophagy-deficient hESCs and NPs appear to become further pronounced following their differentiation to neurons. These data suggest that loss of basal autophagy reduces cell viability of hESC-derived neuronal cells.

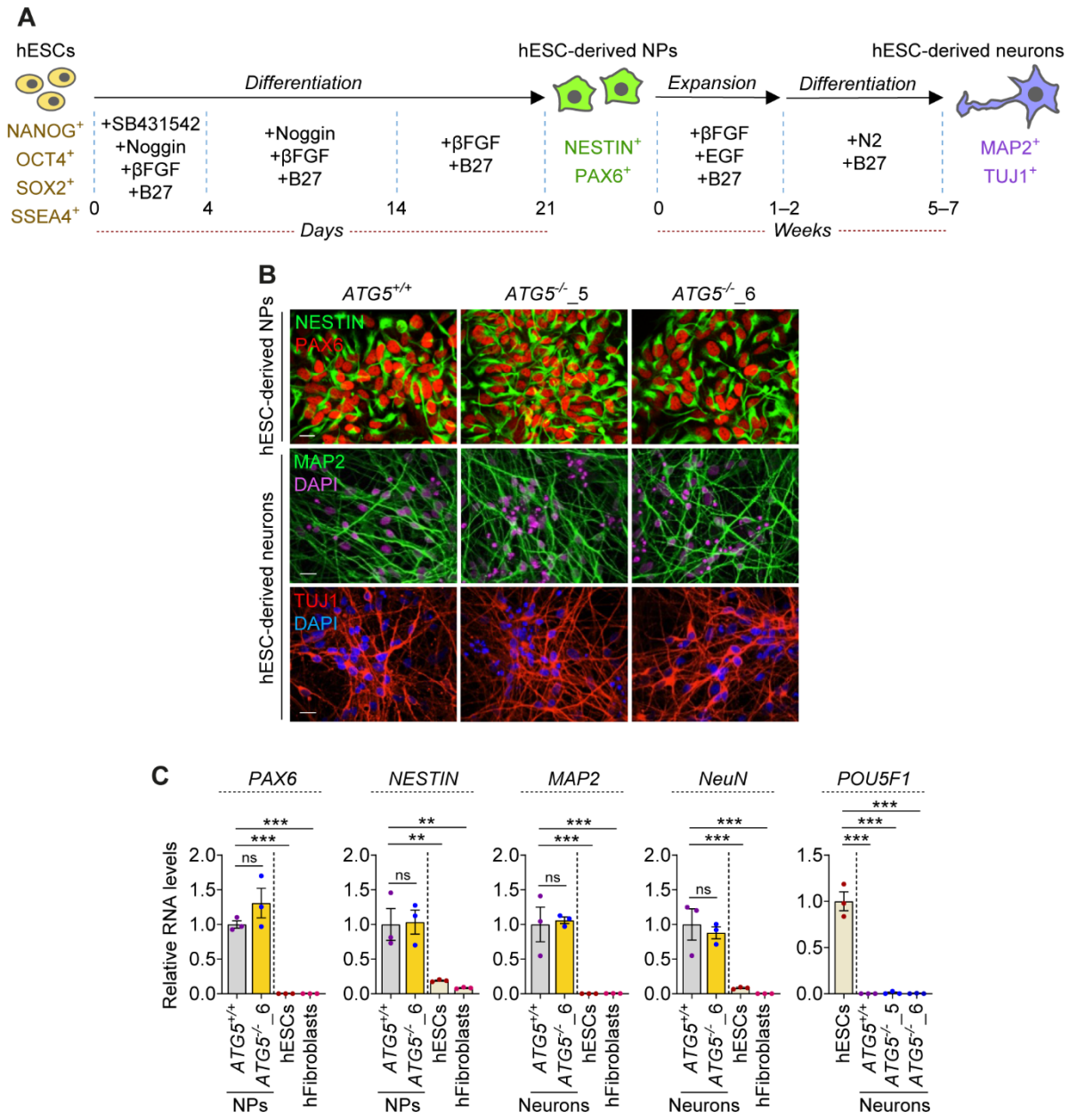

Figure 2.4. Differentiation of *ATG5*$^{-/-}$ NPs and neurons from *ATG5*$^{-/-}$ hESCs.

(A) Schematic representation of differentiation of hESCs into neural precursors (NPs) and neurons.

(B) Immunofluorescence images of NESTIN, PAX6, MAP2, and TUJ1 in *ATG5*$^{+/+}$ and multiple clones of *ATG5*$^{-/-}$ hESC-derived NPs and neurons (4 weeks). *Data generated with Elena Seranova.*

(C) Quantitative RT-PCR expression analyses of *PAX6*, *NESTIN*, *MAP2*, *NeuN* and *POU5F1* (*OCT4*) relative to *GAPDH* in *ATG5*$^{+/+}$, *ATG5*$^{-/-}$_5 and *ATG5*$^{-/-}$_6 hESC-derived NPs and neurons (4 weeks) as indicated, along with wild-type hESCs and human dermal fibroblasts (hFibroblasts) as controls.

Graphical data are mean ± s.e.m. of n = 3–4 biological replicates as indicated. P values were calculated by one-way ANOVA followed by multiple comparisons with two-stage linear step-up procedure of Benjamini, Krieger and Yekutieli on 3 independent experiments (C). ***P<0.001; **P<0.01; ns (non-significant). Scale bar: 100 µm (B).

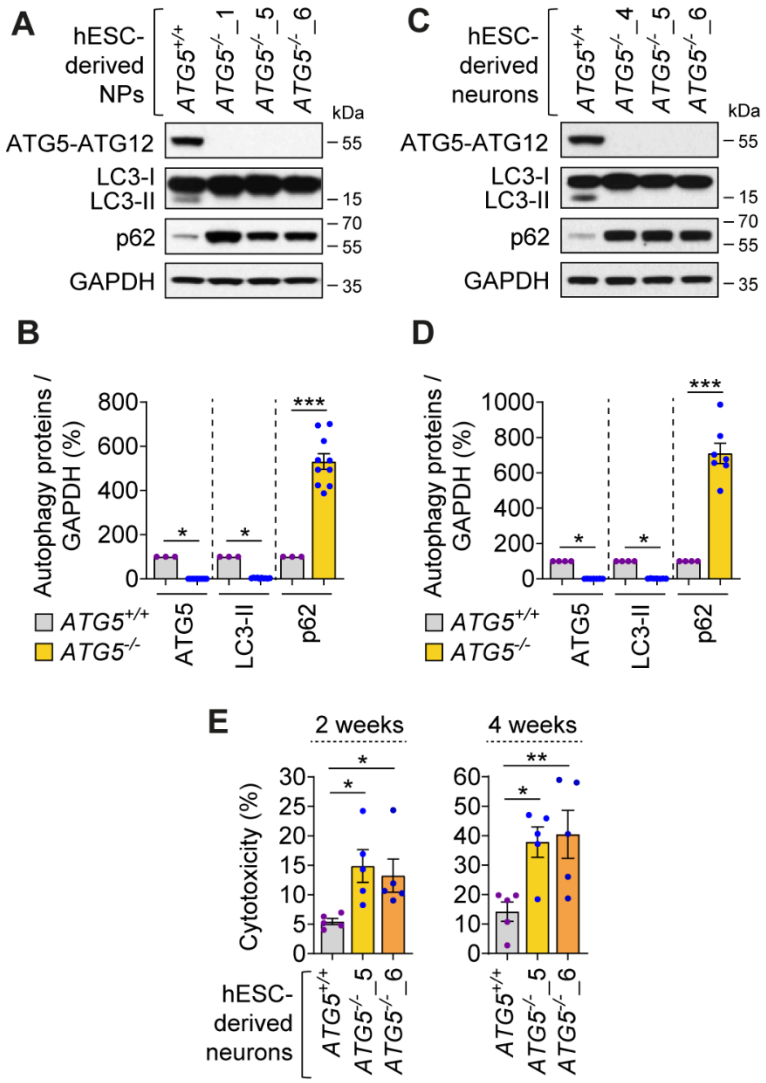

Figure 2.5. Autophagy deficiency and increased cell death in *ATG5*$^{-/-}$ hESC-derived NPs and neurons.

(A-D) Immunoblotting analyses of ATG5, LC3, and p62 in *ATG5*$^{+/+}$ and multiple clones of *ATG5*$^{-/-}$ hESC-derived NPs (A and B) and neurons (4 weeks) (C and D).

(E) Cytotoxicity assay in *ATG5*$^{+/+}$, *ATG5*$^{-/-}$_5, and *ATG5*$^{-/-}$_6 hESC-derived neurons at 2 or 4 weeks of neuronal differentiation.

Graphical data are mean ± SEM of n = 3–10 biological replicates as indicated. P values were calculated by one-way ANOVA followed by multiple comparisons with two-stage linear step-up procedure of Benjamini, Krieger, and Yekutieli on 3 independent experiments (B, D, and E). ∗∗∗p < 0.001; ∗∗p < 0.01; ∗p < 0.05. *Data generated together with Elena Seranova.*

2.3.3. Metabolic perturbations in autophagy-deficient human neurons

Next, the cellular mechanisms underlying cell death was investigated that are primarily affected due to autophagy deficiency in human neurons. Since *ATG5*$^{-/-}$ hESCs and hESC-derived NPs and neurons exhibited cytotoxicity at basal state, it was hypothesized that this might arise from a metabolic failure. Autophagy promotes metabolic homeostasis by recycling cytoplasmic macromolecules and providing the breakdown products as inputs to cellular anabolic processes; failure of which could lead to metabolic stress [70, 165]. Although depletion of several metabolites, amino acids and nucleotides associated with the loss of autophagy has been reported in immortalized cells and mouse models[71, 166], the mechanistic link between these metabolic defects and cell death is unclear.

To investigate any specific metabolic defect in our experimental system, an unbiased metabolomics profiling of wild-type and *ATG5*$^{-/-}$ hESC-derived neurons was performed. Significant depletion of many metabolites related to glycolysis and tricarboxylic acid (TCA) cycle, nucleotide energy carriers and various amino acids was detected in *ATG5*$^{-/-}$ neurons (**Figure 2.6 A, B**). By plotting the magnitude of change against the measure of significance, several nucleotides were found to be significantly depleted in *ATG5*$^{-/-}$ neurons (**Figure 2.6 B-D**). This is in accordance with the nucleic acid recycling defect reported in autophagy-deficient tumour-derived cell lines [166]. Alongside, some of the intermediates of glycolysis and TCA cycle were also significantly lower in *ATG5*$^{-/-}$ neurons. These findings suggest that autophagy-deficient human neurons are associated with metabolic stress under normal growth condition.

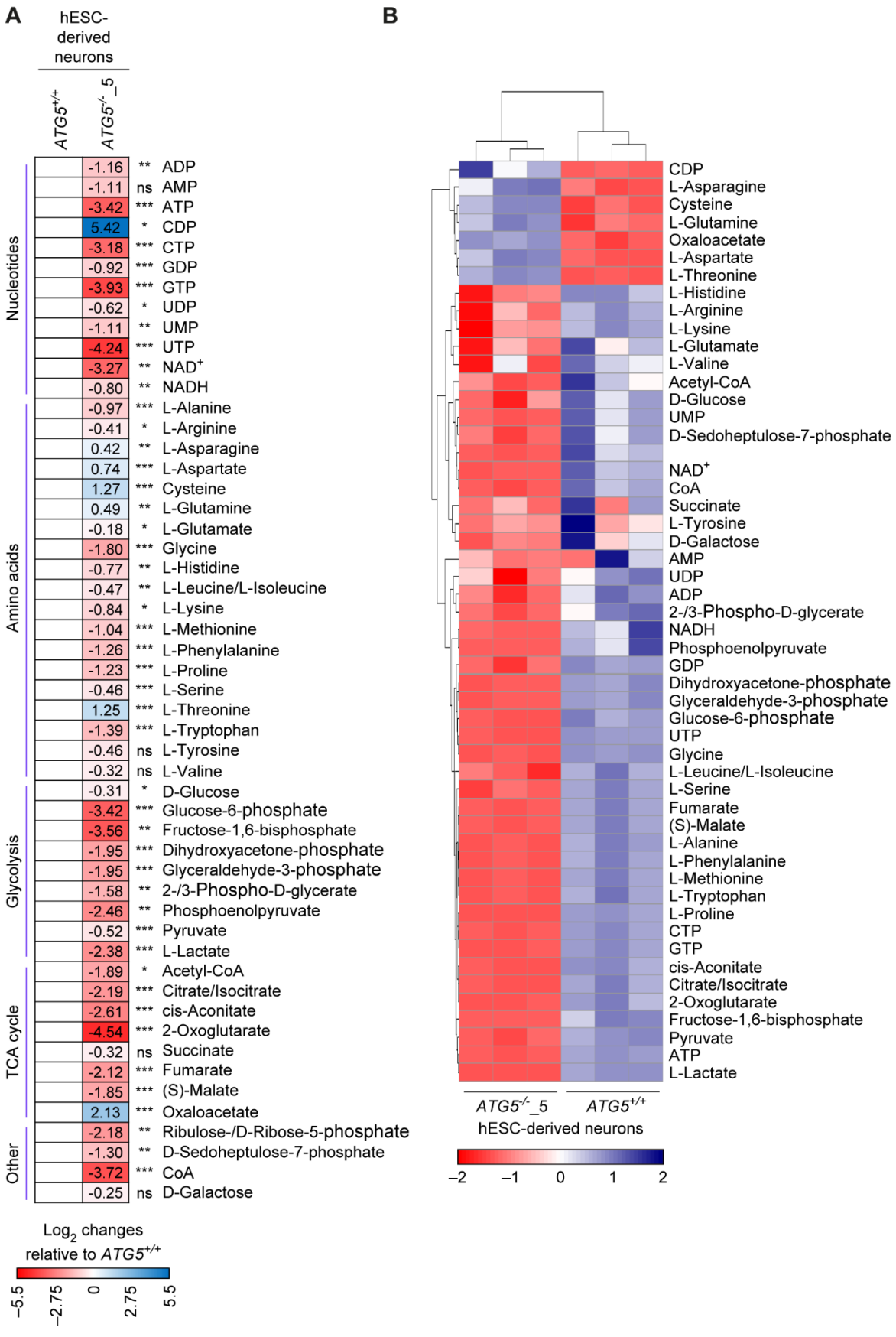
A
hESC-derived neurons
ATG5+/+
ATG5-/-_5
Nucleotides
Amino acids
Glycolysis
TCA cycle
Other
-1.16 ** ADP
-1.11 ns AMP
-3.42 *** ATP
5.42 * CDP
-3.18 *** CTP
-0.92 *** GDP
-3.93 *** GTP
-0.62 * UDP
-1.11 ** UMP
-4.24 *** UTP
-3.27 ** NAD+
-0.80 ** NADH
-0.97 *** L-Alanine
-0.41 * L-Arginine
0.42 ** L-Asparagine
0.74 *** L-Aspartate
1.27 *** Cysteine
0.49 ** L-Glutamine
-0.18 * L-Glutamate
-1.80 *** Glycine
-0.77 ** L-Histidine
-0.47 ** L-Leucine/L-Isoleucine
-0.84 * L-Lysine
-1.04 *** L-Methionine
-1.26 *** L-Phenylalanine
-1.23 *** L-Proline
-0.46 *** L-Serine
1.25 *** L-Threonine
-1.39 *** L-Tryptophan
-0.46 ns L-Tyrosine
-0.32 ns L-Valine
-0.31 * D-Glucose
-3.42 *** Glucose-6-phosphate
-3.56 ** Fructose-1,6-bisphosphate
-1.95 *** Dihydroxyacetone-phosphate
-1.95 *** Glyceraldehyde-3-phosphate
-1.58 ** 2-/3-Phospho-D-glycerate
-2.46 ** Phosphoenolpyruvate
-0.52 *** Pyruvate
-2.38 *** L-Lactate
-1.89 * Acetyl-CoA
-2.19 *** Citrate/Isocitrate
-2.61 *** cis-Aconitate
-4.54 *** 2-Oxoglutarate
-0.32 ns Succinate
-2.12 *** Fumarate
-1.85 *** (S)-Malate
2.13 *** Oxaloacetate
-2.18 ** Ribulose-/D-Ribose-5-phosphate
-1.30 ** D-Sedoheptulose-7-phosphate
-3.72 *** CoA
-0.25 ns D-Galactose
Log2 changes relative to ATG5+/+
−5.5 −2.75 0 2.75 5.5
B
CDP
L-Asparagine
Cysteine
L-Glutamine
Oxaloacetate
L-Aspartate
L-Threonine
L-Histidine
L-Arginine
L-Lysine
L-Glutamate
L-Valine
Acetyl-CoA
D-Glucose
UMP
D-Sedoheptulose-7-phosphate
NAD+
CoA
Succinate
L-Tyrosine
D-Galactose
AMP
UDP
ADP
2-/3-Phospho-D-glycerate
NADH
Phosphoenolpyruvate
GDP
Dihydroxyacetone-phosphate
Glyceraldehyde-3-phosphate
Glucose-6-phosphate
UTP
Glycine
L-Leucine/L-Isoleucine
L-Serine
Fumarate
(S)-Malate
L-Alanine
L-Phenylalanine
L-Methionine
L-Tryptophan
L-Proline
CTP
GTP
cis-Aconitate
Citrate/Isocitrate
2-Oxoglutarate
Fructose-1,6-bisphosphate
Pyruvate
ATP
L-Lactate
ATG5-/-_5
ATG5+/+
hESC-derived neurons
−2 −1 0 1 2

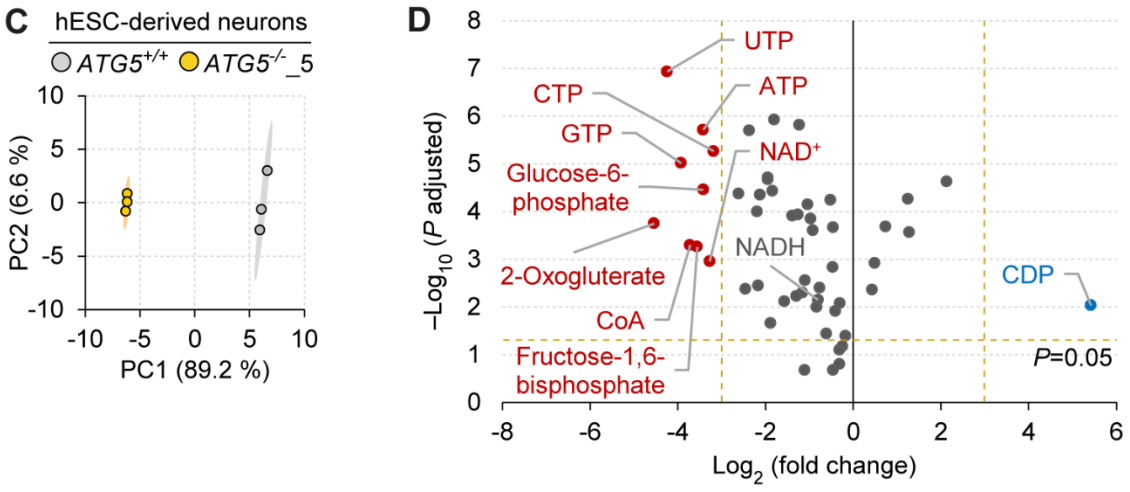

Figure 2.6. Metabolic perturbations in *ATG5*$^{-/-}$ hESC-derived neurons.

(A, B) Heatmap of metabolite levels (A) with hierarchical clustering (B) in *ATG5*$^{+/+}$ and *ATG5*$^{-/-}$_5 hESC-derived neurons (3 weeks).

(C, D) Metabolic profiling depicted as heatmap of log2 (fold change), two-dimensional principal component analysis (PCA) scores plot of metabolites (C) and volcano plot representation of all analyzed metabolites (thresholds shown as dashed orange lines) (D), in a pairwise comparison of *ATG5*$^{-/-}$_5 with *ATG5*$^{+/+}$ hESC-derived neurons (3 weeks).

P values were calculated by Student's *t*-test using Benjamini and Hochberg FDR method (A, C).

2.3.4. Depletion of ATP and NAD in autophagy-deficient neurons despite compensatory increase in glucose metabolism

Metabolomics data implied that glycolysis and TCA cycle are affected because the steady-state levels of the respective starting molecule, such as glucose and acetyl-CoA, as well as several other intermediates were reduced in *ATG5*$^{-/-}$ neurons (**Figure 2.6 A, B**). However, glucose uptake was significantly higher in *ATG5*$^{-/-}$ neurons (**Figure 2.7 A, B**), suggesting that intracellular glucose could be rapidly metabolised through the glycolytic pathway.

Furthermore, [U-$^{13}C_6$]-Glucose tracer was employed to elucidate the contribution of glucose to glycolysis and TCA cycle (**Figure 2.8 A**). Glycolysis breaks the glucose carbon skeleton into three carbon units in the form of pyruvate, which can then undergo several metabolic transformations. These include lactate, alanine, oxaloacetate and the two-carbon unit acetyl-CoA that can enter the TCA cycle condensing with oxaloacetate to form citrate (**Figure 2.8 A**) [167]. The pattern of ^{12}C and ^{13}C carbons in each metabolite provides information on the active metabolic pathways. Both lactate and pyruvate were secreted into the medium with a higher fraction of the M+3 isotopomer in *ATG5*$^{-/-}$ neurons (**Figure 2.8 B, C**), demonstrating a greater contribution of glucose-derived carbons from the glycolytic pathway.

Likewise, intracellular alanine also had an elevated fraction of the M+3 isotopomer in *ATG5*$^{-/-}$ neurons (**Figure 2.9 C**). Labelling patterns of the TCA cycle intermediates such as citrate, α-ketoglutarate, succinate, fumarate and malate included both the M+2 and M+3 isotopomers, indicating that a higher fraction of glucose-derived pyruvate was incorporated via both acetyl CoA and oxaloacetate in *ATG5*$^{-/-}$ neurons. The amino acids aspartate and glutamate also contained glucose-derived ^{13}C label that mirrored the labelling of malate and citrate respectively, indicating that the synthesis of both these metabolites involved a greater contribution from glucose in *ATG5*$^{-/-}$ neurons (**Figure 2.9 A-J**).

Collectively, the data show a greater use of glucose in central carbon metabolism in autophagy-deficient neurons as an attempt to cope with their metabolic stress. However, despite this compensation, the reduction in almost all TCA cycle metabolites suggests that this response is insufficient to ameliorate the loss of autophagy-derived metabolites from the metabolic network.

The overall yield from glycolysis and TCA cycle normally constitutes ATP and NADH [168]. Despite increased glucose contribution to these metabolic pathways, unbiased metabolomics data revealed significant depletion of ATP, ADP, NAD^+ and NADH levels in *ATG5*$^{-/-}$ neurons (**Figure 2.10 A, B**); which was further confirmed by specific luminescence- and colorimetric-based assays (**Figure 2.10 C, D**). Since depletion of energy carriers like ATP and NADH could trigger an energetic deficit [168], it is likely that the autophagy-deficient neurons are attempting to restore their levels by utilizing more glucose through glycolysis and TCA cycle. These data indicate that amongst the major energy carriers, NAD depletion during loss of autophagy in post-mitotic neurons is associated with increased cytotoxicity.

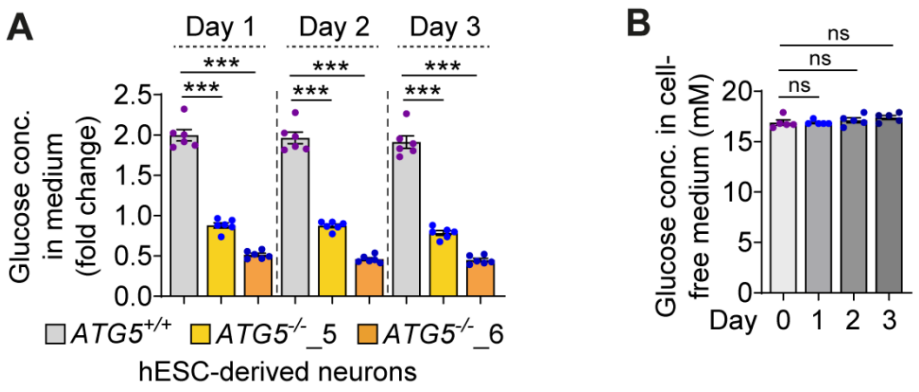

Figure 2.7. Elevation of glucose uptake in *ATG5*$^{-/-}$ hESC-derived neurons.

(A) Measurement of glucose concentration in the medium (fold change from day 0) of *ATG5*$^{+/+}$ and *ATG5*$^{-/-}$ hESC-derived neurons (3 weeks).

(B) Measurement of glucose concentration in cell-free medium (to establish baseline concentration over the duration of the experiment) at day 0, 1, 2 and 3.

Graphical data are mean ± SEM of n = 5–6 biological replicates as indicated. P values were calculated by one-way ANOVA followed by multiple comparisons with two-stage linear step-up procedure of Benjamini, Krieger, and Yekutieli (A, B) on 3 independent experiments. ∗∗∗p < 0.001; ∗∗p < 0.01; ∗p < 0.05; ns (non-significant).

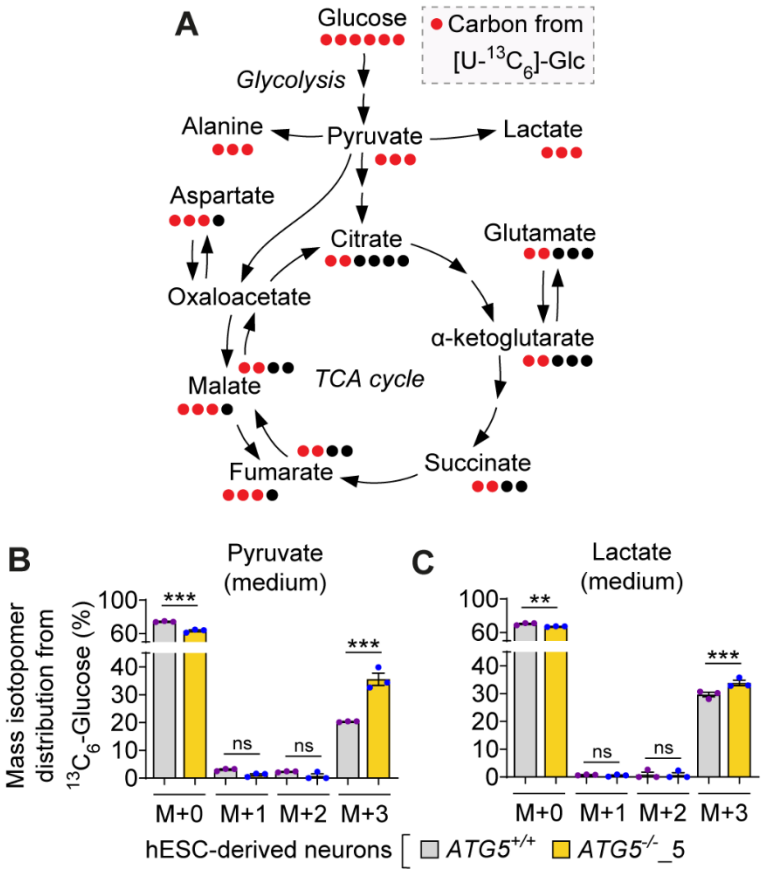

Figure 2.8. [U-$^{13}C_6$]-Glucose tracer shows greater contribution of glucose-derived carbons from glycolytic pathway in *ATG5*$^{-/-}$ hESC-derived neurons.

(A) Schematic representation of carbon atom (circles) transitions from [U-$^{13}C_6$]-glucose tracer to determine the contribution of glucose to glycolysis and TCA cycle.

(B, C) Mass isotopomer distribution from [U-$^{13}C_6$]-glucose in various glycolysis and TCA cycle intermediates Pyruvate (B) and Lactate (C), measured in the medium of *ATG5*$^{+/+}$ and *ATG5*$^{-/-}$ hESC-derived neurons (3 weeks) by GC-MS.

Graphical data are mean ± SEM of n = 3 biological replicates as indicated. P values were calculated by one-way ANOVA followed by multiple comparisons with two-stage linear step-up procedure of Benjamini, Krieger, and Yekutieli (B, C). ∗∗∗p < 0.001; ∗∗p < 0.01; ∗p < 0.05; ns (non-significant).

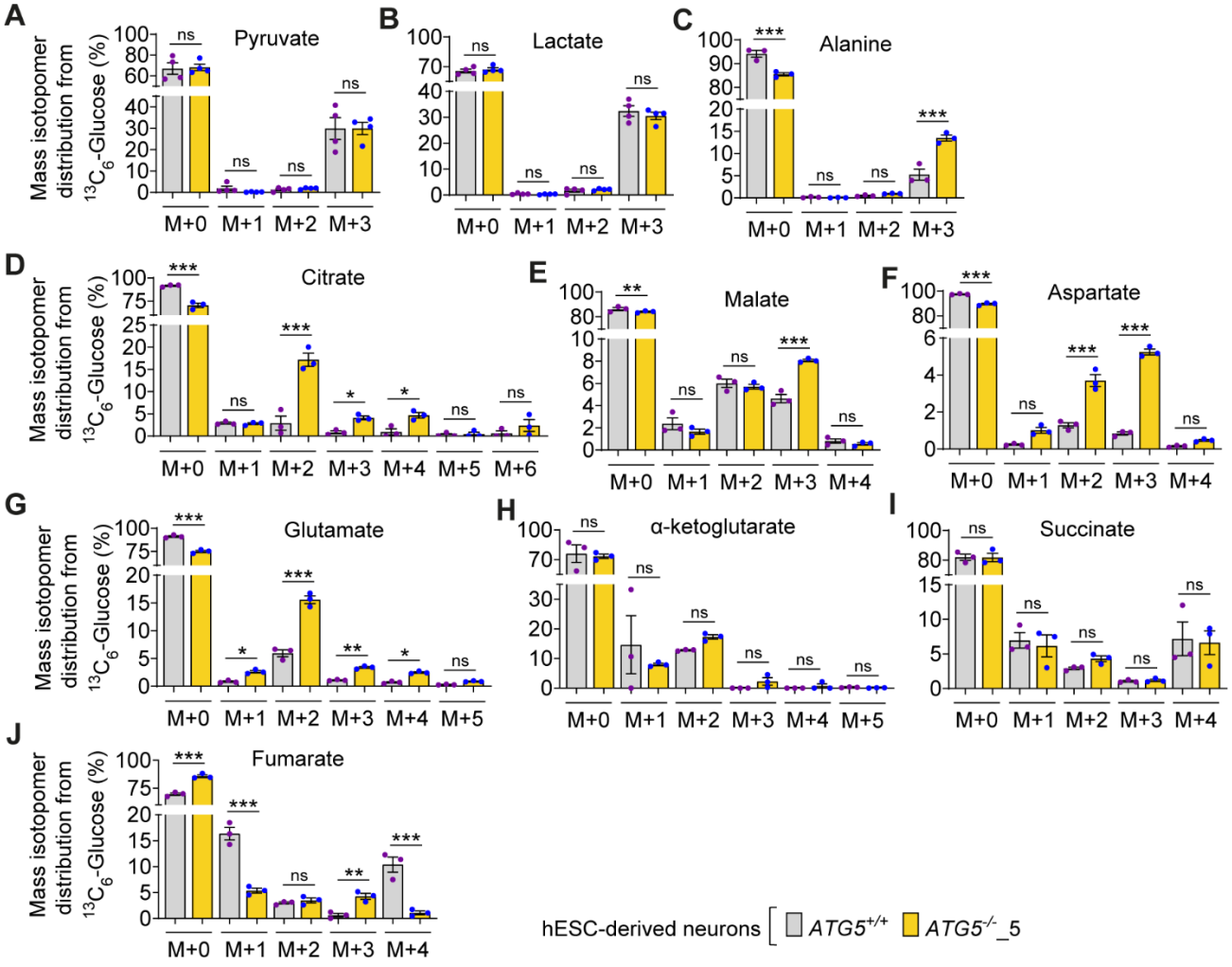

Figure 2.9. [U-$^{13}C_6$]-Glucose tracer shows greater contribution of glucose in glycolysis and TCA cycle metabolites in *ATG5*$^{-/-}$ hESC-derived neurons.

(A-J) Mass isotopomer distribution from [U-$^{13}C_6$]-glucose in various glycolysis and TCA cycle intermediates as indicated, measured in the cell extract of *ATG5*$^{+/+}$ and *ATG5*$^{-/-}$ hESC-derived neurons (3 weeks) by GC-MS.

Graphical data are mean ± SEM of n = 3-4 biological replicates as indicated. P values were calculated by one-way ANOVA followed by multiple comparisons with two-stage linear step-up procedure of Benjamini, Krieger, and Yekutieli (A-J). ***p < 0.001; **p < 0.01; *p < 0.05; ns (non-significant).

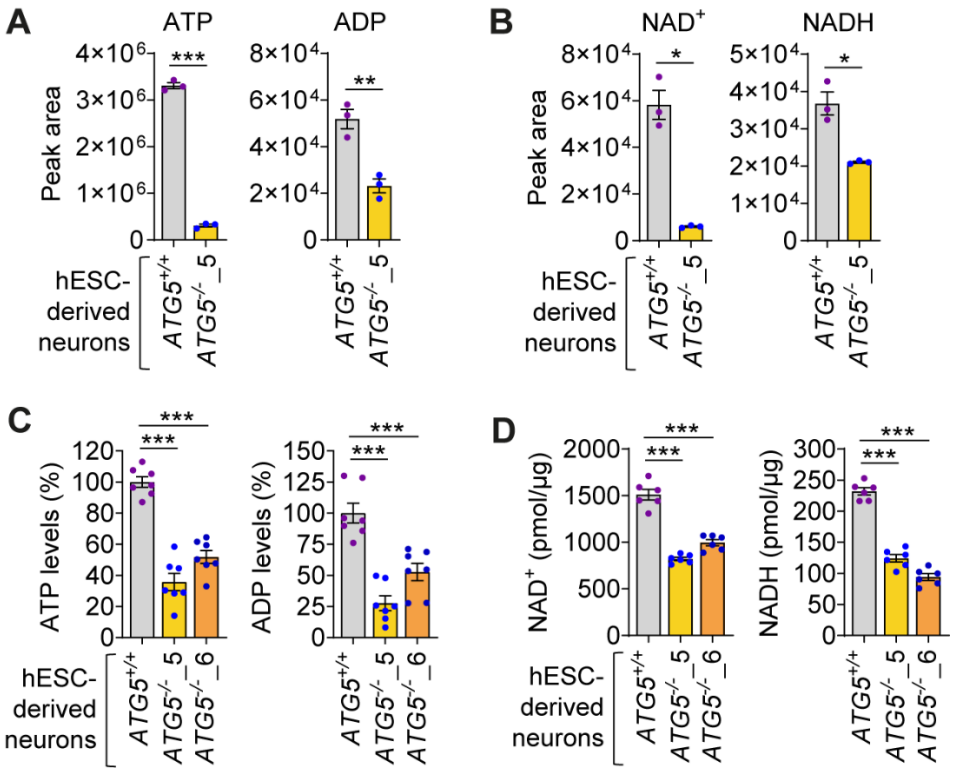

Figure 2.10. Depletion of ATP, ADP, NAD⁺ and NADH in *ATG5*$^{-/-}$ hESC-derived neurons.

(A, B) LC-MS analyses of ATP, ADP (A), NAD⁺ and NADH (B) levels in *ATG5*$^{+/+}$, *ATG5*$^{-/-}$_5 hESC-derived neurons (3 weeks)

(C, D) Assay-based measurements of ATP, ADP (A), NAD⁺ and NADH (B) levels in *ATG5*$^{+/+}$ and *ATG5*$^{-/-}$ hESC-derived neurons (3 weeks).

Graphical data are mean ± SEM of n = 3–7 biological replicates as indicated. P values were calculated by one-way ANOVA followed by multiple comparisons with two-stage linear step-up procedure of Benjamini, Krieger, and Yekutieli (A-D) on 3 independent experiments. ∗∗∗p < 0.001; ∗∗p < 0.01; ∗p < 0.05; ns (non-significant).

2.3.5. Supplementation of L-tryptophan restores NAD levels and rescues viability of autophagy-deficient neurons

Apart from nucleotides and various intracellular metabolites, unbiased metabolomics profiling also revealed a significant depletion of several amino acids in *ATG5*$^{-/-}$ neurons (**Figure 2.6 A, B**). By plotting the magnitude of change of all the amino acids against their measure of significance, glycine and L-tryptophan were found to be most significantly depleted in *ATG5*$^{-/-}$ neurons (**Figure 2.11 A**). However, individual amino acid uptake was not overtly different between ATG5$^{-/-}$ and wild-type neurons as measured by the fold change of amino acid concentrations in the medium, except for increased uptake of L-aspartate and L-glutamate in *ATG5*$^{-/-}$ neurons (**Figure 2.11 B-F**), indicating higher reliance on these amino acids. Both amino acids are excitatory neurotransmitters. [169], and their increased uptake in *ATG5*$^{-/-}$ neurons could be due to higher metabolic demand in TCA cycle as revealed by [U-$^{13}C_6$]-Glucose tracer (**Figure 2.8 A** and **2.9 A-J**).

Next, investigation was made whether supplementation with each of the 12 amino acids, which were significantly depleted as per unbiased metabolomics (**Figure 2.6 A, B**), could rescue the viability of *ATG5*$^{-/-}$ neurons. Interestingly, only supplementation of L-tryptophan, which was depleted in these cells (**Figures 2.6 A, B** and **2.11 A, E**), significantly reduced cytotoxicity in *ATG5*$^{-/-}$ neurons (**Figure 2.12 A**). The cytoprotective effect of L-tryptophan supplementation was further confirmed by the reduction of TUNEL^{+} apoptotic nuclei in TUJ1^{+} *ATG5*$^{-/-}$ neurons (**Figures 2.12 B, C**). L-tryptophan is required for the de novo synthesis of NAD via the kynurenine pathway (**Figures 2.12 D**) [170], and hence it could impact cell survival by modulating NAD levels that were depleted in *ATG5*$^{-/-}$ neurons (**Figures 2.6 A, D** and **2.10 B, D**). Concomitant to reducing cell death, L-tryptophan supplementation significantly restored NAD levels in *ATG5*$^{-/-}$ neurons (**Figure 2.12 E**), raising the possibility that NAD levels could affect the viability of autophagy-deficient human neurons.

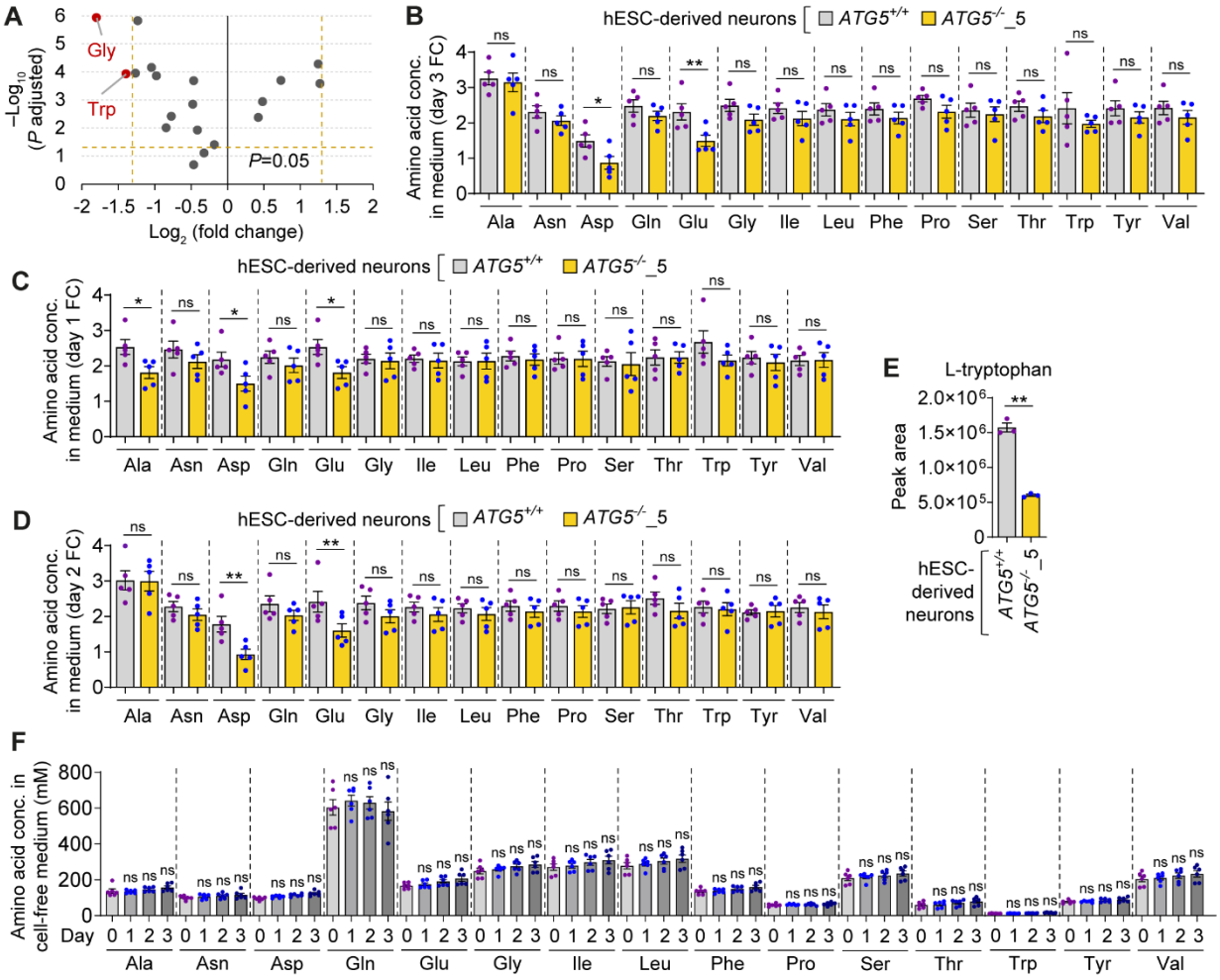

Figure 2.11. Amino acid uptake profiling in *ATG5*$^{-/-}$ hESC-derived neurons.

(A) Volcano plot representation of all amino acids in a pairwise comparison of *ATG5*$^{-/-}$ with *ATG5*$^{+/+}$ hESC-derived neurons (3 weeks); thresholds shown as dashed orange lines.

(B) Measurement of amino acid concentrations (fold change at day 3) in the medium of *ATG5*$^{+/+}$ and *ATG5*$^{-/-}$ hESC-derived neurons (3 weeks) by GC-MS.

(C, D) Measurements of individual amino acid concentrations in medium, depicted as fold change (FC) at day 1 (C) and 2 (D) of *ATG5*$^{+/+}$ and *ATG5*$^{-/-}$ hESC-derived neurons (3 weeks) by GC-MS.

(E) LC-MS analysis of L-tryptophan in *ATG5*$^{+/+}$ and *ATG5*$^{-/-}$ hESC-derived neurons (3 w).

(F) Measurements of individual amino acid concentrations in cell-free medium at day 0, 1, 2 and 3 by GC-MS. A cell-free control was used to account for variation in concentration due to evaporation or thermal degradation of the analytes.

Graphical data are mean ± SEM of n = 3–6 biological replicates as indicated. P values were calculated by Student's t test using Benjamini and Hochberg FDR method (A) or one-way ANOVA followed by multiple comparisons with two-stage linear step-up procedure of Benjamini, Krieger, and Yekutieli (B-E) on 3 independent experiments. ∗∗∗p < 0.001; ∗∗p < 0.01; ∗p < 0.05; ns (non-significant).

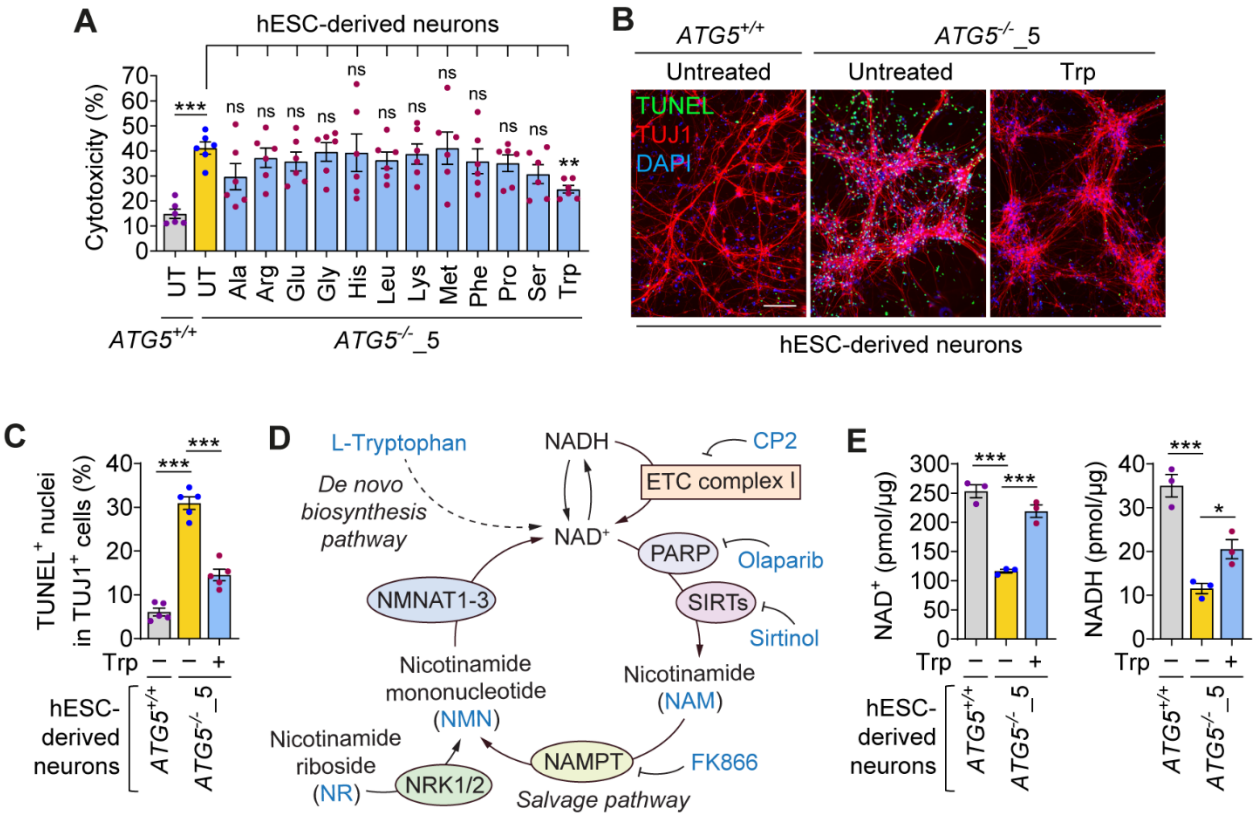

Figure 2.12. Supplementation of L-tryptophan restores NAD levels and rescues viability of *ATG5*$^{-/-}$ hESC-derived neurons.

(A) Cytotoxicity assay in *ATG5*$^{+/+}$ and *ATG5*$^{-/-}$ hESC-derived neurons (3 weeks), where *ATG5*$^{-/-}$ neurons were treated with or without 1 mM individual amino acid as indicated for the last 6 days of neuronal differentiation period.

(B, C) Immunofluorescence images of TUJ1 with TUNEL staining (B) and quantification of TUNEL^{+} apoptotic nuclei (C) in *ATG5*$^{+/+}$ and *ATG5*$^{-/-}$_5 hESC-derived neurons (3 weeks), where *ATG5*$^{-/-}$ neurons were treated with or without 1 mM L-tryptophan (Trp) for the last 6 days of neuronal differentiation period.

(D) Schematic representation of NAD^{+} de novo biosynthetic and salvage pathways where compounds used for modulating NAD levels are indicated.

(E) Measurements of NAD^{+} and NADH levels in *ATG5*$^{-/-}$ hESC-derived neurons (3 weeks), treated with or without 1 mM L-Trp for the last 6 days of neuronal differentiation period.

Graphical data indicate mean ± SEM of n = 3–6 biological replicates. P values were calculated by one-way ANOVA followed by multiple comparisons with two-stage linear step-up procedure of Benjamini, Krieger, and Yekutieli (A, C, and E) on 3 independent experiments. ***p < 0.001; **p < 0.01; *p < 0.05; ns (non-significant). Scale bar: 100 µm (B).

2.3.6. Boosting intracellular NAD improves the viability of autophagy-deficient neurons

A potential role of NAD in mediating cytotoxicity in human neurons with autophagy deficiency was further investigated. NAD^+ (the oxidized form of NAD) was one of the most depleted metabolites in *ATG5*$^{-/-}$ neurons, whereas NADH (the reduced form of NAD) was also significantly lower, indicating exhaustion of the total pool of NAD (**Figures 2.10 B, D**). Initially, assessment was made whether preventing NAD production affects cell viability by the inhibition of the enzyme nicotinamide phosphoribosyltransferase (NAMPT), which is involved in NAD biosynthesis via a salvage pathway, with FK866 (**Figure 2.12 D**) [171]. The NAMPT inhibitor FK866 markedly lowered NAD levels and compromised the viability of *ATG5*$^{-/-}$ neurons (Figures and **Figure 2.13 A-D**), suggesting that depletion of intracellular NAD reduced neuronal viability.

Conversely, it was studied whether boosting intracellular NAD levels can rescue cell viability. A well-known strategy is supplementation with the bioavailable NAD precursor nicotinamide (NAM) (**Figure 2.12 D**) [75, 76], which significantly raised the levels of NAD and enhanced the survival of *ATG5*$^{-/-}$ neurons (**Figures 2.14 A-D**). The cytoprotective effects of boosting NAD in autophagy-deficient cells were further supported with additional NAD precursors, such as nicotinamide riboside (NR) and nicotinamide mononucleotide (NMN) (**Figure 2.12 D**) [172, 173]. Indeed, both NR and NMN significantly restored NAD levels and rescued cell viability in *ATG5*$^{-/-}$ neurons (**Figures 2.15 A-D**). Since the NAD precursors elevated NAD levels via the salvage pathway, their dependency on NAMPT for conversion was analysed using FK866 (**Figure 2.12 D**). The cytoprotective effect of NAM in rescuing the viability of *ATG5*$^{-/-}$ neurons was completely abolished by FK866 (**Figure 2.14 B**); however, the effects of NR or NMN were unaffected by FK866 treatment (**Figure 2.15 D**). This is likely because NAMPT is required for the conversion of NAM to NAD^+, whereas NR and NMN act downstream of NAMPT (**Figure 2.12 D**). Overall, these data suggest that modulating NAD levels affects cell viability and that boosting intracellular NAD improves the survival of autophagy-deficient human neurons.

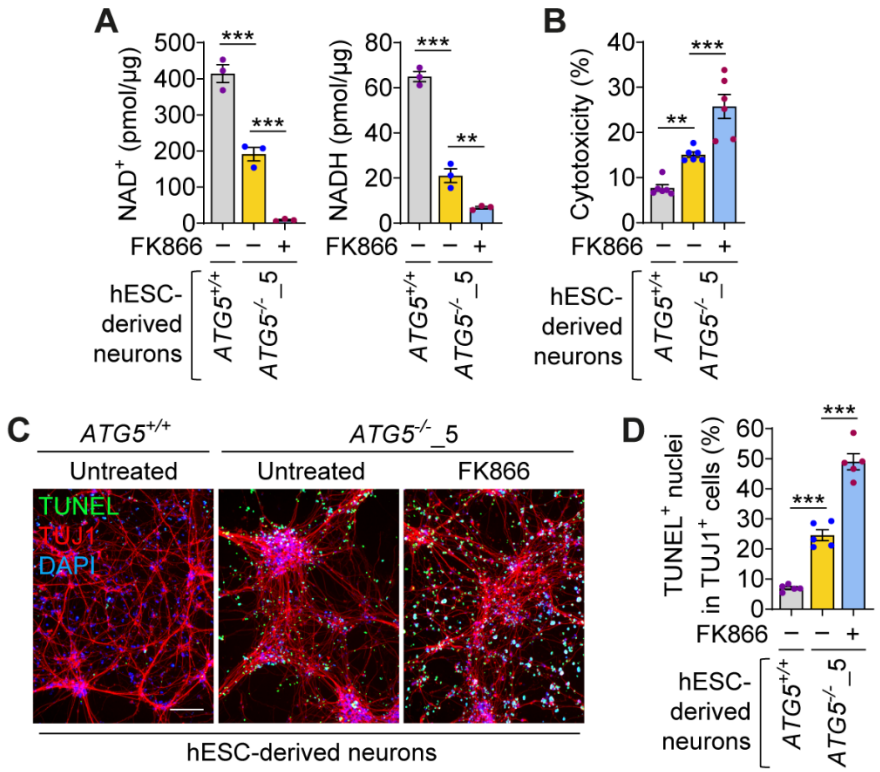

Figure 2.13. Suppression of NAD production by NAMPT inhibitor FK866 increases cell death in *ATG5*$^{-/-}$ hESC-derived neurons.

(A-D) Measurements of NAD^+ and NADH levels (A), cytotoxicity assay (B), immunofluorescence images of TUJ1 with TUNEL staining (C), and quantification of $TUNEL^+$ apoptotic nuclei (D) in *ATG5*$^{+/+}$ and *ATG5*$^{-/-}$_5 hESC-derived neurons (3 weeks), where *ATG5*$^{-/-}$ neurons were treated with or without 10 nM FK866 for the last 6 days of neuronal differentiation period.

Graphical data are mean ± SEM of n = 3–6 biological replicates as indicated. P values were calculated by one-way ANOVA followed by multiple comparisons with two-stage linear step-up procedure of Benjamini, Krieger, and Yekutieli on 3 independent experiments (A, B, D). ***p < 0.001; **p < 0.01; *p < 0.05; ns (non-significant). Scale bar: 100 µm (C).

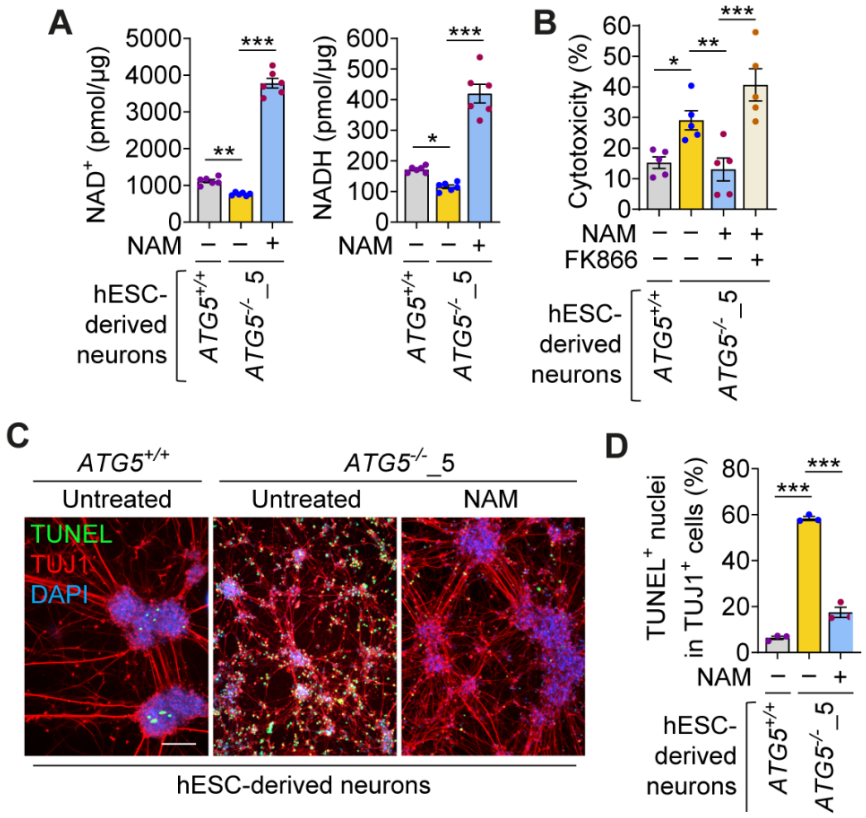

Figure 2.14. NAD precursor NAM increases NAD levels and improves cell viability in *ATG5*$^{-/-}$ hESC-derived neurons.

(A–D) Measurements of NAD$^+$ and NADH levels (A), cytotoxicity assay (B), immunofluorescence images of TUJ1 with TUNEL staining (C), and quantification of TUNEL$^+$ apoptotic nuclei (D) in *ATG5*$^{+/+}$ and *ATG5*$^{-/-}$_5 hESC-derived neurons (3 weeks), where *ATG5*$^{-/-}$ neurons were treated with or without 10 nM FK866(B), 1 mM NAM(A-D) as indicated for the last 6 days of neuronal differentiation period.

Graphical data are mean ± SEM of n = 3–6 biological replicates as indicated. P values were calculated by one-way ANOVA followed by multiple comparisons with two-stage linear step-up procedure of Benjamini, Krieger, and Yekutieli on 3 independent experiments (A, B, D). ***p < 0.001; **p < 0.01; *p < 0.05; ns (non-significant). Scale bar: 100 µm (C).

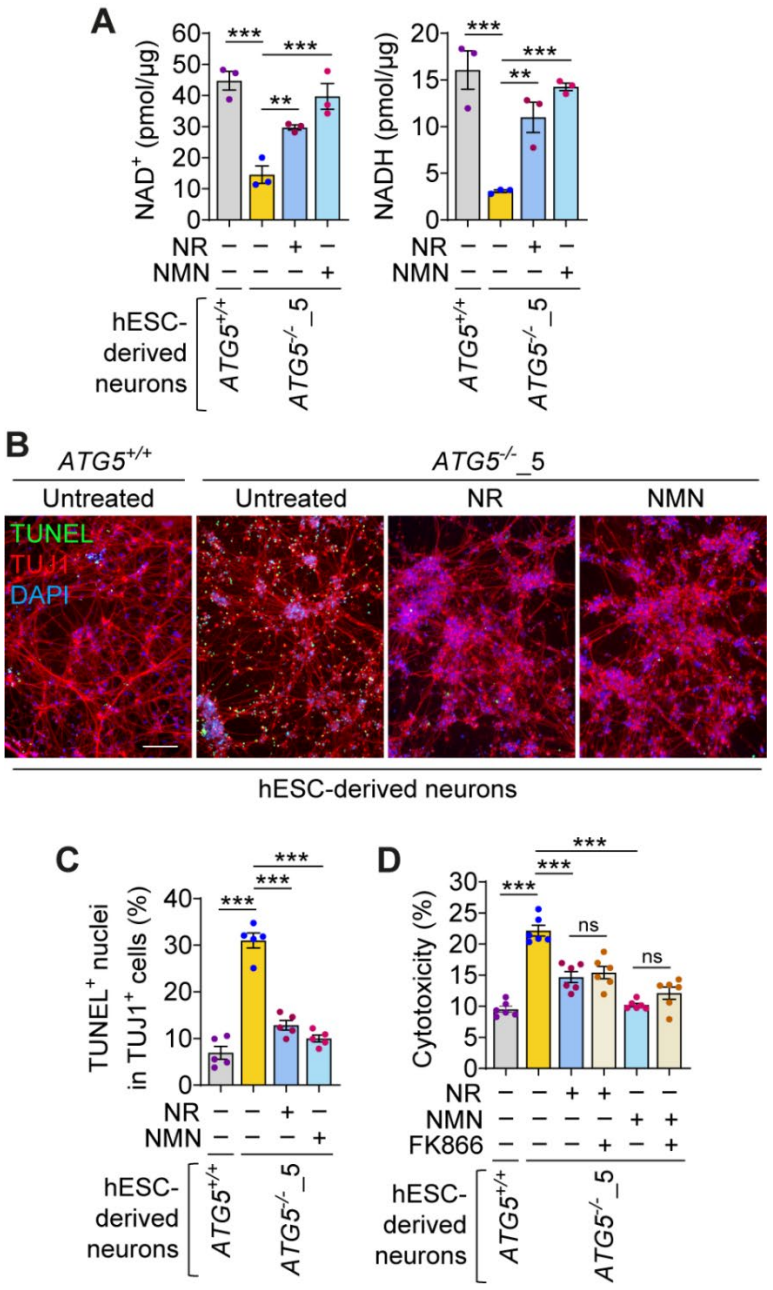

Figure 2.15. Boosting NAD with NR and NMN restore NAD levels and improve cell viability in *ATG5*$^{-/-}$ hESC-derived neurons.

(A-D) Measurements of NAD$^+$ and NADH levels (A), immunofluorescence images of TUJ1 with TUNEL staining (B), quantification of TUNEL$^+$ apoptotic nuclei (C), and cytotoxicity assay (D) in *ATG5*$^{+/+}$ and *ATG5*$^{-/-}$_5 hESC-derived neurons (3 weeks), where *ATG5*$^{-/-}$ neurons were treated with or without 1 mM NR (A-D), 1 mM NMN (A-D), or 10 nM FK866 (D) as indicated for the last 6 days of neuronal differentiation period.

Graphical data are mean ± SEM of n = 3–6 biological replicates as indicated. P values were calculated by one-way ANOVA followed by multiple comparisons with two-stage linear step-up procedure of Benjamini, Krieger, and Yekutieli on 3 independent experiments (A, C, D). ∗∗∗p < 0.001; ∗∗p < 0.01; ∗p < 0.05; ns (non-significant). Scale bar: 100 µm (B).

2.3.7. Increased NADase activity mediates NAD depletion in autophagy-deficient neurons

Further investigation was done on the mechanism of NAD depletion in *ATG5*$^{-/-}$ neurons. NAD^+ can be degraded by NAD^+ nucleosidases (NADases) to maintain NAD^+ homeostasis [174, 175]. The two main classes of NADases are deacetylases of the sirtuin family (SIRTs) and poly-ADP-ribose polymerases (PARPs), which utilize NAD^+ as a substrate (**Figure 2.12 D**) [176]. Activities of SIRTs and PARPs were elevated in *ATG5*$^{-/-}$ neurons and also in *ATG5*$^{-/-}$ hESCs and NPs, as evident from the reduction in protein acetylation and increase in poly-ADP-ribosylation (PARylation) of acetylated lysine and poly(ADP-ribose), respectively (**Figures 2.16 A-E**). Further measurement was carried out for the enzymatic activity of SIRT1, SIRT2, PARP1, and PARP2, all of which were higher in *ATG5*$^{-/-}$ neurons compared with WT neurons (**Figure 2.16 F**). These data imply that hyperactivation of these NAD-consuming enzymes during loss of autophagy could deplete NAD and trigger cell death.

To test this possibility, pharmacological inhibition of SIRTs and PARPs was done with sirtinol and olaparib, respectively (**Figures 2.12 D** and **Figure 2.17 A-D**). Both sirtinol and olaparib rescued NAD levels and the viability of *ATG5*$^{-/-}$ neurons (**Figures 2.17 E-H**), suggesting that suppression of NAD exhaustion increases the survival of autophagy-deficient human neurons. Simultaneous inhibition of SIRTs and PARPs in *ATG5*$^{-/-}$ neurons rescued NAD levels and cell viability to a greater extent than what was achieved with the inhibition of either enzyme alone (**Figures 2.17 E, F**), thus implicating both classes of NADases in NAD depletion.

PARPs and SIRTs are activated in response to DNA damage and oxidative stress, and both these NADases are involved in the regulation of genomic stability [177]. instability via impairment in DNA double-strand break repair mechanisms and inefficient turnover of p62 and nuclear components [178]. Expectedly, increased DNA damage was found in *ATG5*$^{-/-}$ neurons as evident from significantly higher numbers of γH2AX and 53BP1 foci compared with the WT neurons (**Figures 2.18 A-D**). These data imply that persistent DNA damage in autophagy deficient neurons could contribute to NAD depletion via activation of NAD-consuming enzymes.

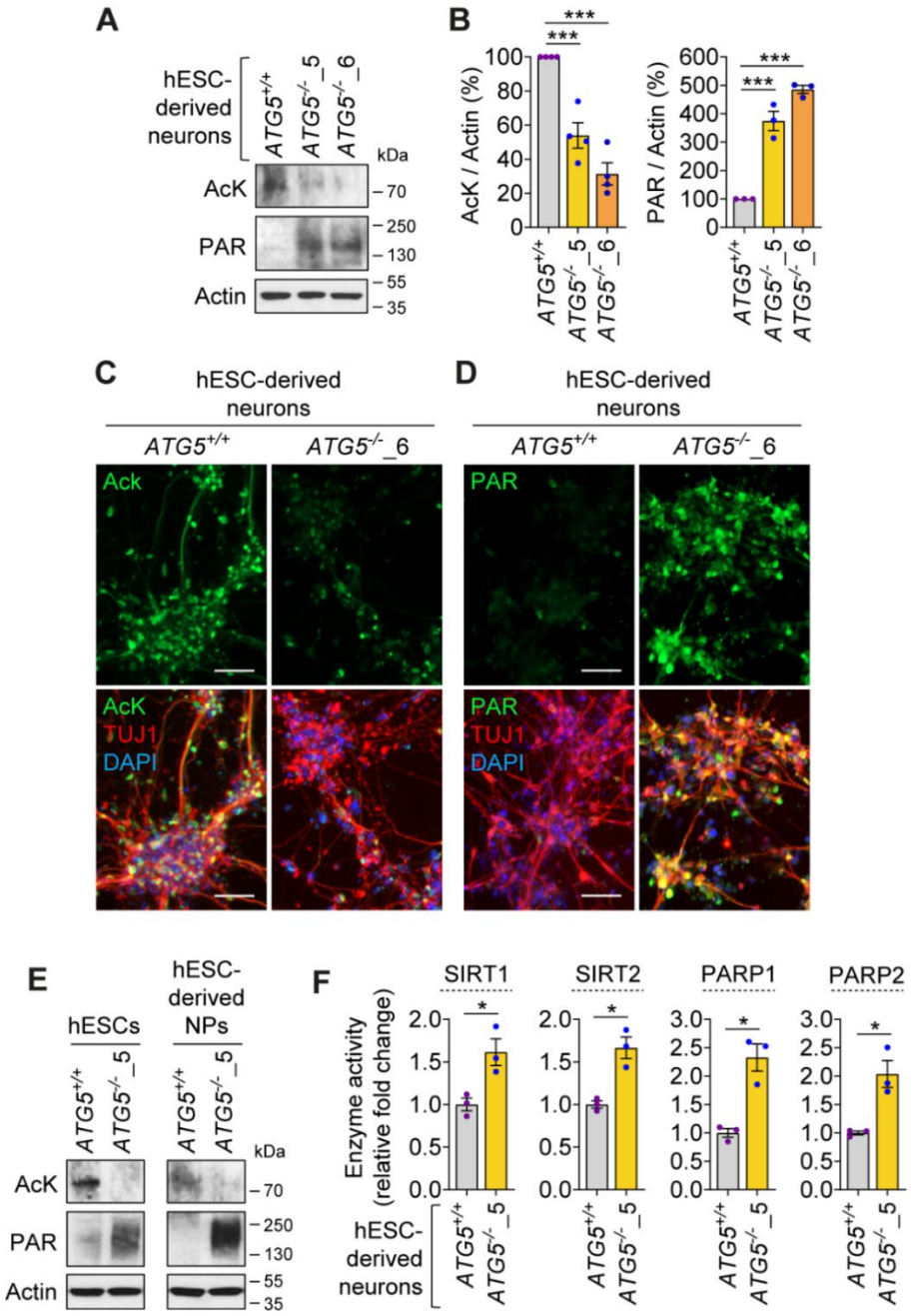

Figure 2.16. Increased NADase activity in *ATG5*$^{-/-}$ hESC-derived neurons.

(A-D) Immunoblotting analyses of acetylated lysine (AcK) and poly(ADP-ribose) (PAR) (A and B), immunofluorescence images of TUJ1 with AcK (C) or PAR (D) in *ATG5*$^{+/+}$ and *ATG5*$^{-/-}$ hESC-derived neurons (3 weeks).

(E) Immunoblotting analyses of acetylated lysine (AcK) and poly(ADP-ribose) (PAR) in *ATG5*$^{+/+}$ and *ATG5*$^{-/-}$_5 hESCs , hESC-derived neural precursors (NPs).

(F) Enzymatic activity of SIRT1, SIRT2, PARP1, and PARP2 in *ATG5*$^{+/+}$ and *ATG5*$^{-/-}$ hESC-derived neurons (3 weeks).

Graphical data are mean ± SEM of n = 3–6 biological replicates as indicated (B, F). P values were calculated by one-way ANOVA followed by multiple comparisons with two-stage linear step-up procedure of Benjamini, Krieger, and Yekutieli (B) or unpaired two-tailed Student's t-test (F) on 3 independent experiments. ∗∗∗p < 0.001; ∗p < 0.05. Scale bars: 10 μm (G), 50 μm (C, D).

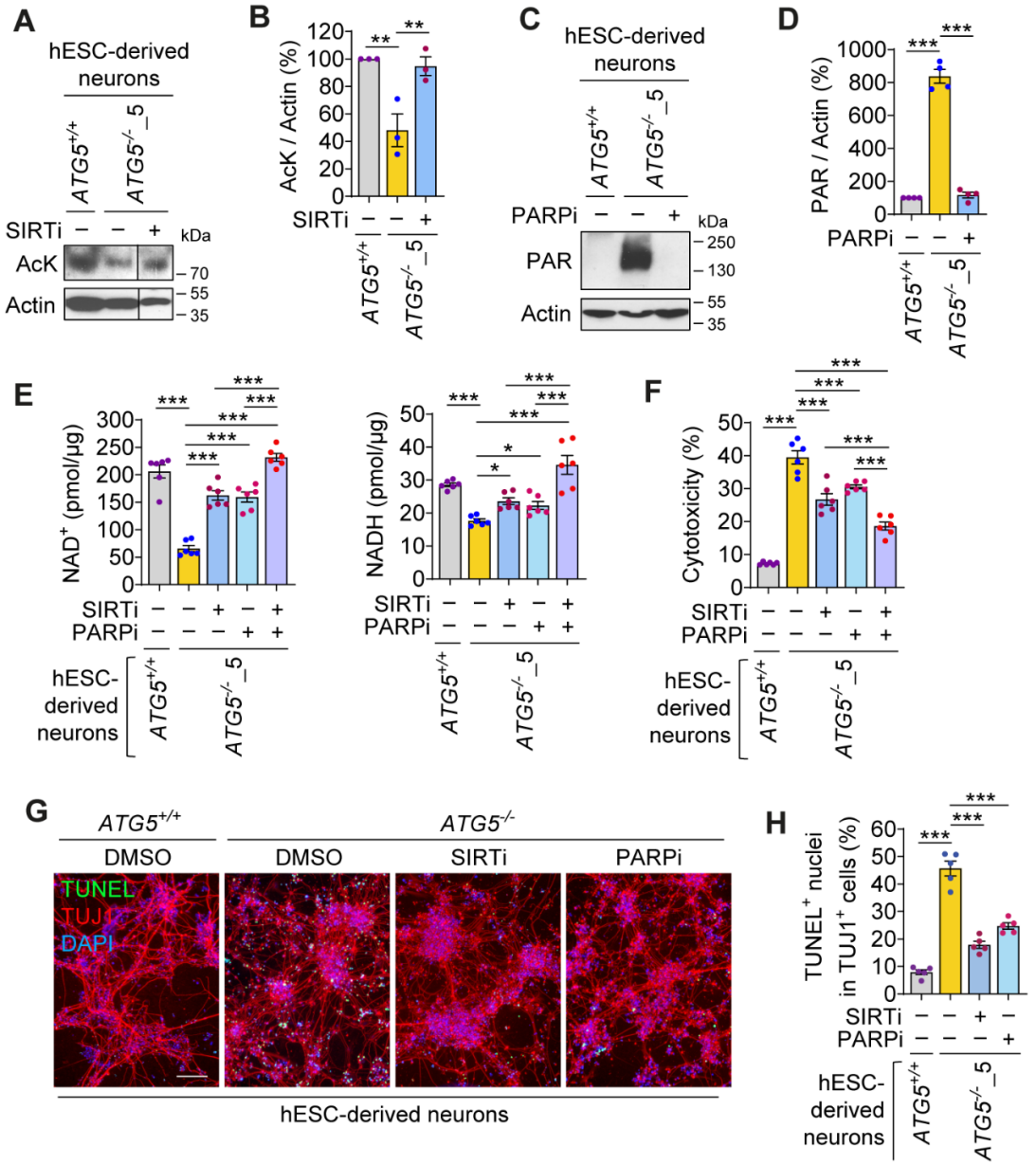

Figure 2.17. Inhibition of SIRTs and PARPs rescues NAD levels and cell viability in *ATG5*$^{-/-}$ hESC-derived neurons.

(A-D) Immunoblotting analyses of acetylated lysine (AcK) (A, B) and poly(ADP-ribose) (PAR) (C, D) in *ATG5*$^{+/+}$ and *ATG5*$^{-/-}$_5 hESC-derived neurons (3 weeks), where *ATG5*$^{-/-}$ neurons were treated with or without 20 µM sirtinol (SIRTinhibitor) (A, B) or 10 µM olaparib (PARP inhibitor) (C, D) for the last 3 (PARPi) or 6 (SIRTi) days of neuronal differentiation period.

(E-H) Measurements of NAD$^+$ and NADH levels (E), cytotoxicity assay (F), immunofluorescence images of TUJ1 with TUNEL staining (G), and quantification of TUNEL$^+$ apoptotic nuclei (H) in *ATG5*$^{+/+}$ and *ATG5*$^{-/-}$_5 hESC-derived neurons (3 weeks), where *ATG5*$^{-/-}$ neurons were treated with or without 20 µM sirtinol (SIRT inhibitor), 10 µM olaparib (PARP inhibitor), or both for the last 3 days of neuronal differentiation period.

Graphical data are mean ± SEM of n = 3–6 biological replicates as indicated. P values were calculated by one-way ANOVA followed by multiple comparisons with two-stage linear step-up procedure of Benjamini, Krieger, and Yekutieli (B, D, E, F, H) on 3 independent experiments. ∗∗∗p < 0.001; ∗p < 0.05. Scale bar: 100 µm (G).

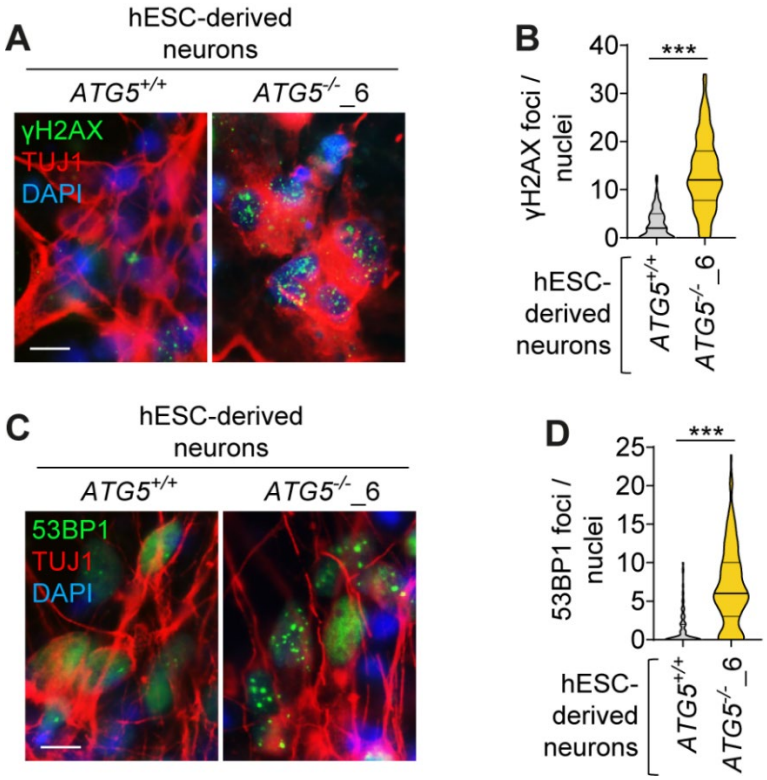

Figure 2.18. Increased DNA damage in *ATG5*$^{-/-}$ hESC-derived neurons.

(A, B) Immunofluorescence images of TUJ1 with phospho-γH2AX (A), and quantification of phospho-γH2AX foci (B) in *ATG5*$^{+/+}$ and *ATG5*$^{-/-}$_6 hESC-derived neurons (3 weeks).

(C, D) Immunofluorescence images of TUJ1 with 53BP1 (C) and quantification of 53BP1 foci (D) in *ATG5*$^{+/+}$ and *ATG5*$^{-/-}$_6 hESC-derived neurons (3 weeks).

Graphical data are displayed as violin plot (lines at median and quartiles) from ~200 cells per condition of n = 3 biological replicates (A, C). P values were calculated by unpaired two-tailed Student's t test (B, D) on 3 independent experiments. ***p < 0.001; *p < 0.05. Scale bars: 10 µm (A, C).

2.3.8. NAD depletion triggers cell death via mitochondrial depolarization in autophagy-deficient neurons

The mechanistic link between NAD depletion and cell death was next investigated in autophagy-deficient human neurons. While NAD^+ was substantially decreased in the cytosolic fraction, NADH was predominantly detected and found to be depleted in the mitochondrial fraction of *ATG5*$^{-/-}$ neurons (**Figure 2.19 A**). Oxidation of NADH mediates the generation of mitochondrial membrane potential ($\Delta\Psi_m$), in which the flow of electrons (donated by NADH) through the mitochondrial electron transport chain (ETC) coupled to proton pumping across the inner mitochondrial membrane create an electrochemical proton gradient, which eventually drives ATP production by the mitochondrial F_0F_1 ATP synthase [179]. Depletion of NADH in autophagy- deficient cells could thus dissipate $\Delta\Psi_m$ and mediate cytotoxicity [180].Supporting this hypothesis, *ATG5*$^{-/-}$ neurons displayed a reduction in $\Delta\Psi_m$ as measured by TMRE fluorescence intensity (**Figure 2.19 B**). Moreover, *ATG5*$^{-/-}$ neurons had elevation in reactive oxygen species (ROS) and mitochondrial fragmentation (**Figures 2.19 C-E**), and an increase in oxidative stress could contribute to SIRT activation in these cells (**Figures 2.16 A-C, F**) [80]. Furthermore, loss of autophagy will lead to inefficient mitophagy resulting in the accumulation of damaged mitochondria [181], which was confirmed by the increase in mitochondrial load in *ATG5*$^{-/-}$ neurons as assessed by elevated Tom20 levels (**Figure 2.19 F, G**).

Collectively, these data raise the possibility that the deficit in NADH links autophagy deficiency to cell death via mitochondrial dysfunction and the loss of $\Delta\Psi_m$. To test this hypothesis, mitochondrial NADH consumption was pharmacologically suppressed with CP2, which reversibly inhibits mitochondrial ETC complex I and partially prevents the use of NADH as a substrate (**Figure 2.12 D**) [182]. CP2 increased NAD levels and rescued cell viability in *ATG5*$^{-/-}$ neurons (**Figures 2.20 A-D**), and these cytoprotective effects were associated with the rescue of $\Delta\Psi_m$ in *ATG5*$^{-/-}$ neurons (**Figure 2.21 A**). Additional NAD boosting agents were tested for their effects in attenuating mitochondrial depolarization. NAM, NR, NMN, and L-tryptophan, all of which improved NAD levels and cell viability in *ATG5*$^{-/-}$ neurons (**Figures 2.12 B-E**, **2.14 A-D** and **2.15 A-D**), also rescued $\Delta\Psi_m$ in these cells (**Figures 2.21 A, B**).

Furthermore, analysis of mitochondrial respiration by measuring the oxygen consumption rate showed severe impairment in *ATG5*$^{-/-}$ neurons compared with WT neurons, as seen by reduction in basal respiration, maximal respiration, and ATP production (**Figures 2.21**

C, D). Boosting intracellular NAD levels with NAM, NR, and NMN restored these mitochondrial respiratory parameters in *ATG5*$^{-/-}$ neurons to the levels in WT neurons (**Figures 2.21 C, D**). These data suggest that restoration of $\Delta\Psi_m$ and mitochondrial bioenergetics underlies the cytoprotective effects of enhancing NAD levels in *ATG5*$^{-/-}$ neurons. This is particularly important for differentiated cells like neurons, which have high energy demand and are greatly reliant on mitochondrial oxidative phosphorylation for energy production [183].

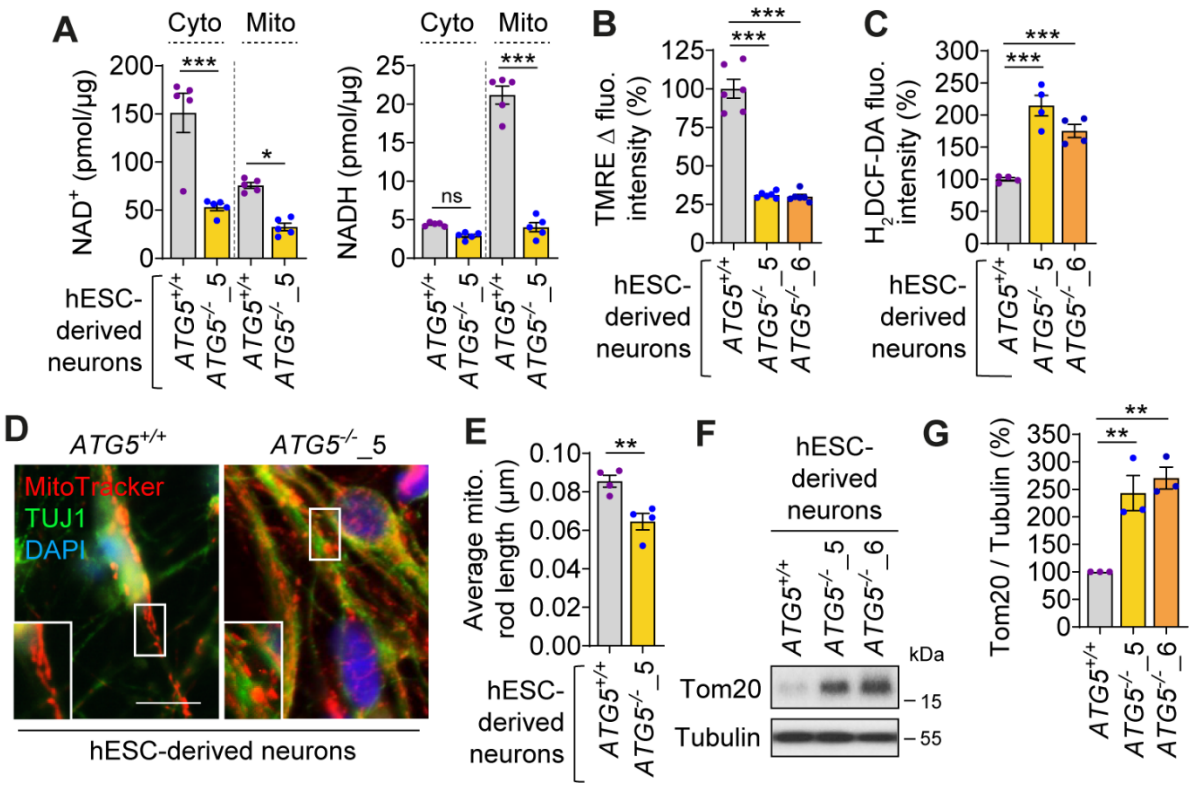

Figure 2.19. NAD depletion triggers cell death via mitochondrial depolarisation in *ATG5*$^{-/-}$ hESC-derived neurons.

(A–E) Measurements of NAD^+ and NADH levels in cytoplasmic (cyto) and mitochondrial (mito) fractions (A), TMRE Δ fluorescence intensity (pre- and post-FCCP treatment) for ΔΨm (B) and H_2DCF-DA fluorescence intensity for ROS (C), immunofluorescence images of TUJ1 with MitoTracker staining (D), and analysis of average mitochondrial rod length per image (E) in *ATG5*$^{+/+}$ and *ATG5*$^{-/-}$ hESC-derived neurons (3 weeks).

(F, G) Immunoblotting analysis of Tom20 (F) and quantification relative to Tubulin (G) in *ATG5*$^{+/+}$, *ATG5*$^{-/-}$_5 and *ATG5*$^{-/-}$_6 hESC-derived neurons (3 weeks).

Graphical data are mean ± SEM of n = 3–5 biological replicates as indicated. P values were calculated by one-way ANOVA followed by multiple comparisons with two-stage linear step-up procedure of Benjamini, Krieger, and Yekutieli (A, C, G) or unpaired two-tailed Student's t test (E) on 3 independent experiments. ∗∗∗p < 0.001; ∗∗p < 0.01; ∗p < 0.05; ns (non-significant). Scale bar: 10 µm (D). *Data in C–G generated together with Elena Seranova.*

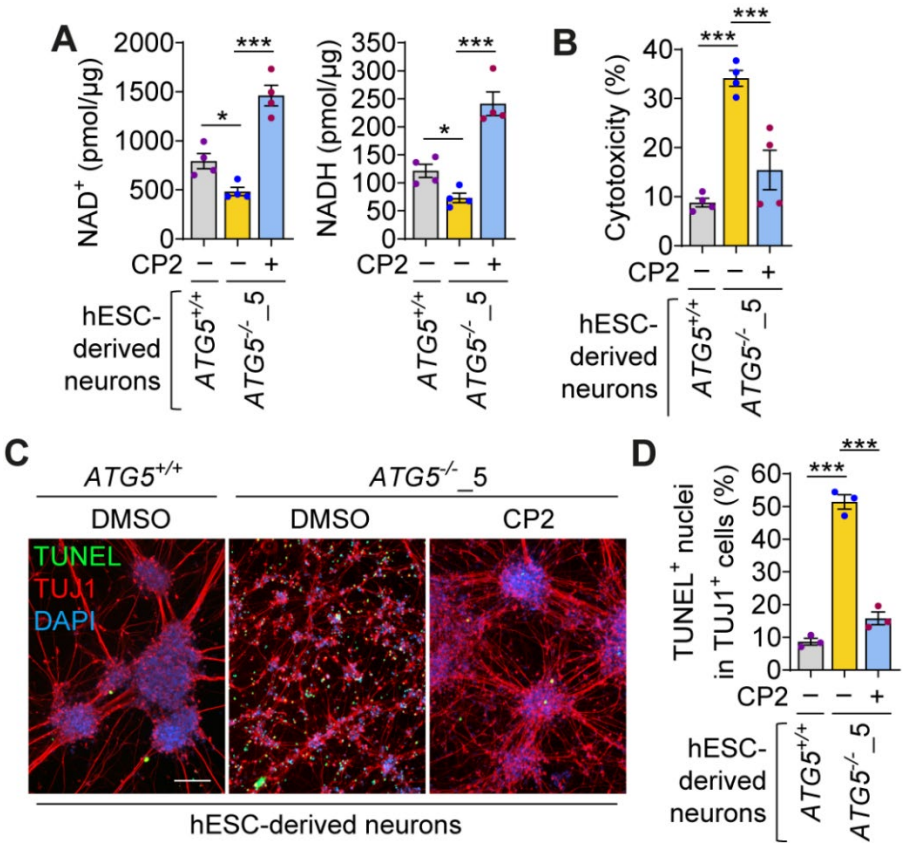

Figure 2.20. Suppression of NADH consumption by CP2 rescues NAD levels and cell viability in *ATG5*$^{-/-}$ hESC-derived neurons.

(A–D) Measurements of NAD+ and NADH levels (A), cytotoxicity assay (B), immunofluorescence images of TUJ1 with TUNEL staining (C) and quantification of TUNEL^{+} apoptotic nuclei (D) in *ATG5*$^{+/+}$ and *ATG5*$^{-/-}$_5 hESC-derived neurons (3 weeks), where *ATG5*$^{-/-}$ neurons were treated with or without 1 µM CP2 for the last 6 days of neuronal differentiation period.

Graphical data are mean ± SEM of n = 3–4 biological replicates as indicated. P values were calculated by one-way ANOVA followed by multiple comparisons with two-stage linear step-up procedure of Benjamini, Krieger, and Yekutieli (A, B, D) on 3 independent experiments. ***p < 0.001; **p < 0.01; *p < 0.05; ns (non-significant). Scale bar: 100 µm (C).

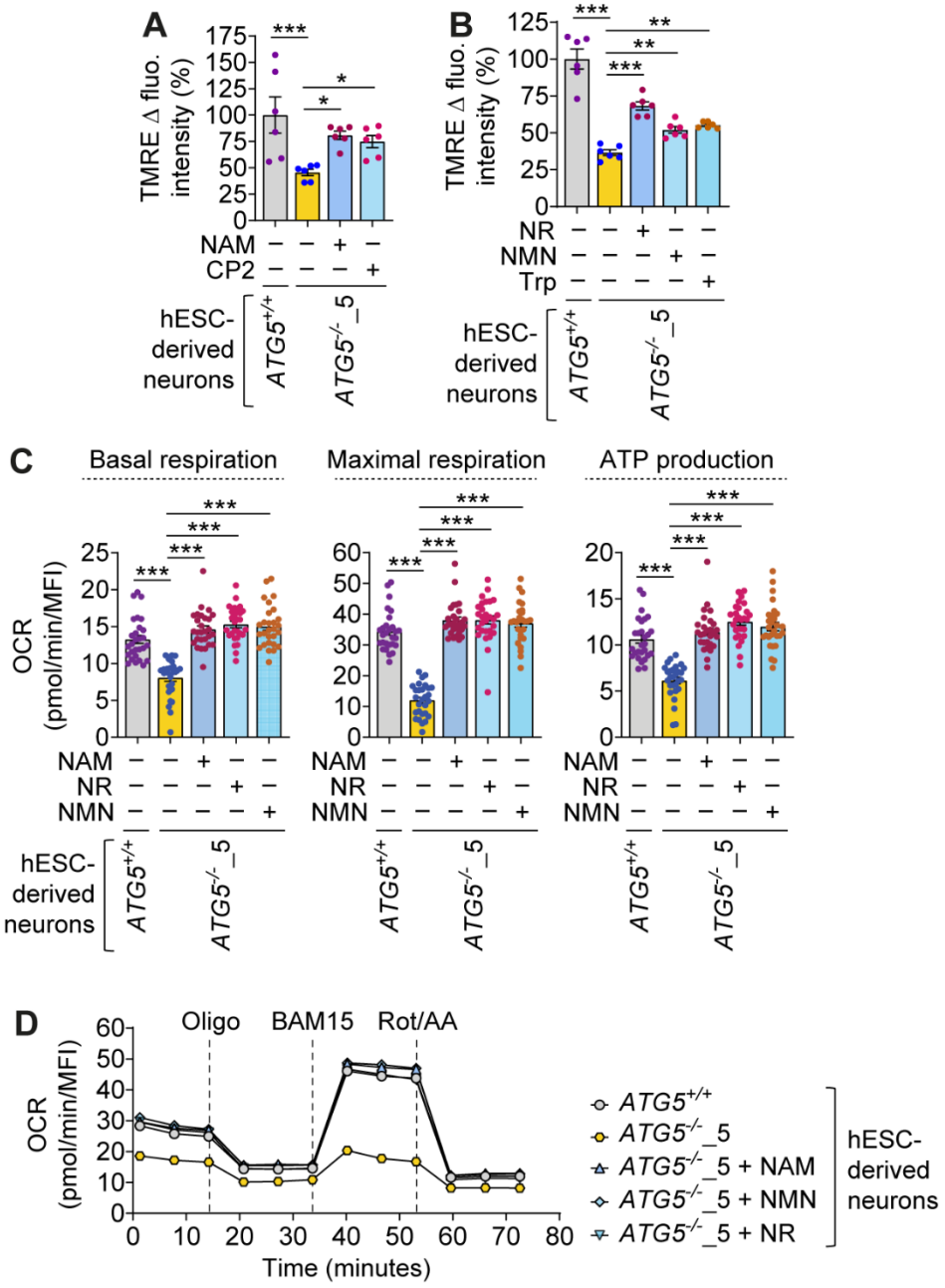

Figure 2.21. NAD boosters restore mitochondrial membrane potential and respiration in *ATG5*$^{-/-}$ hESC-derived neurons.

(A–D) Measurements of TMRE Δ fluorescence intensity (A, B), and post-mitochondrial stress test measurement by Seahorse analyzer of basal respiration, maximal respiration, ATP production (C), and oxygen consumption rate (OCR) levels (D) after addition of oligomycin (Oligo), BAM15, and rotenone (Rot)/antimycin A (AA) in *ATG5*$^{+/+}$ and *ATG5*$^{-/-}$_5 hESC-derived neurons (3 weeks), where *ATG5*$^{-/-}$ neurons were treated with or without 1 μM CP2 (A), 1 mM NAM (A, C, D), 1 mM NR (B-D), 1 mM NMN (B–D), 1 mM L-Trp (B) for the last 6 days of neuronal differentiation period. *Seahorse analysis in C and D was done with Samuel Lara-Reyna*.

Graphical data are mean ± SEM of n = 3–28 biological replicates as indicated. P values were calculated by one-way ANOVA followed by multiple comparisons with two-stage linear step-up procedure of Benjamini, Krieger, and Yekutieli (A-C) on 3 independent experiments. ***p < 0.001; **p < 0.01; *p < 0.05; ns (non-significant). MFI, mean fluorescent intensity.

2.3.9. Mitochondrial dysfunction perturbs proteostasis in autophagy-deficient neurons

Since autophagy is the primary clearance route for aggregated proteins, malfunction of this degradative process leads to proteotoxic stress during aging and neurodegenerative diseases [95, 158, 184]. Recent studies have demonstrated a crosstalk between mitochondrial and protein homeostasis, also involving NAD homeostasis, wherein NAD boosters enhanced mitochondrial function and attenuated amyloid accumulation in aged worms and mice [185-188].

Therefore, this phenomenon was studied in autophagy-deficient human neurons using ProteoStat staining, which can detect aggresomes that are accumulation of aggregated proteins [189]. As expected, *ATG5*$^{-/-}$ hESCs and hESC-derived NPs and neurons displayed a substantial increase in ProteoStat signal compared with the respective WT cell types (**Figures 2.22 A-F**), indicating accumulation of aggresomes in autophagy-deficient cells. Remarkably, increasing NAD levels with NAM, NR, and NMN markedly reduced the ProteoStat signal in *ATG5*$^{-/-}$ cells (**Figures 2.22 A-F**), suggesting that NAD boosters improved proteostasis, which is concomitant with restoring mitochondrial function (**Figures 2.21 A-D**).

To further study this crosstalk, a non-reducing disaccharide called trehalose was used that prevents protein aggregation [190].Trehalose reduced the ProteoStat signal and also restored $\Delta\Psi_m$ in *ATG5*$^{-/-}$ neurons (**Figures 2.22 A, B, G**), suggesting that suppression of aggresomes improved $\Delta\Psi_m$. Overall, our data show that NAD boosters could improve cell survival by restoring mitochondrial and protein homeostasis during loss of autophagy.

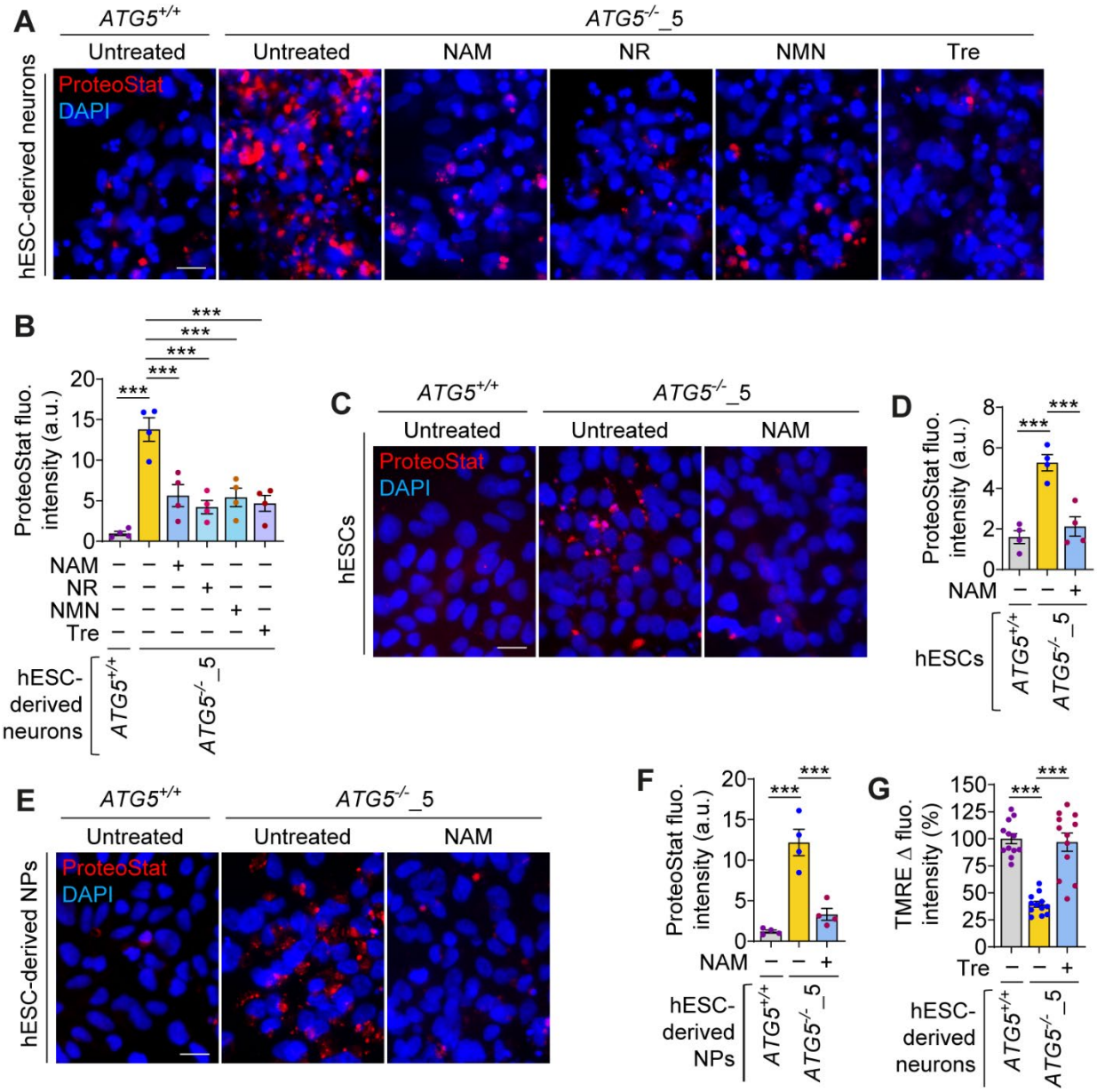

Figure 2.22. NAD boosters reduce aggresomes in *ATG5*$^{-/-}$ hESCs and hESC-derived neuronal cells.

(A, B) Measurements of fluorescence images of ProteoStat staining for aggresome detection (A) and quantification of ProteoStat fluorescence intensity in arbitrary units (a.u.) (B) in *ATG5*$^{+/+}$ and *ATG5*$^{-/-}$_5 hESC-derived neurons (3 weeks), where *ATG5*$^{-/-}$ neurons were treated with or without 1 mM NAM, 1 mM NR, 1 mM NMN, 1 mM L-Trp, or 100 mM trehalose (Tre) for the last 6 days of neuronal differentiation period.

(C-G) Fluorescence images of ProteoStat staining for aggresome detection (C, E), quantification of ProteoStat fluorescence (fluo) intensity (in arbitrary units; a.u.) (D, F), and measurement of TMRE Δ fluorescence intensity (pre and post FCCP treatment) for ΔΨm (G) in *ATG5*$^{+/+}$ and *ATG5*$^{-/-}$_5 hESCs (C, D) and hESC-derived NPs (E, F) and neurons (3 weeks) (G), where *ATG5*$^{-/-}$ cells were treated with or without 1 mM NAM for 48 h (C-F) or 100 mM trehalose (Tre) (G) for the last 6 days of neuronal differentiation period.

Graphical data are mean ± s.e.m. of n = 3–12 biological replicates as indicated. P values were calculated by one-way ANOVA followed by multiple comparisons with two-stage linear step-up procedure of Benjamini, Krieger and Yekutieli (B, D, F, G) on 4 independent experiments. ***P<0.001; **P<0.01; *P<0.05. Scale bar: 20 µm (A, C, E).

Chapter 3

Targeting the autophagy-NAD axis rescues disease phenotypes in iPSC-derived neuronal model of Wolfram syndrome

Chapter 3: Targeting the autophagy-NAD axis rescues disease phenotypes in iPSC-derived neuronal model of Wolfram sydrome

3.1 Introduction

Neurodegenerative diseases are associated with impaired autophagic activity, accumulation of misfolded protein aggregates, lower NAD^+ levels, and mitochondrial dysfunction [2]. Wolfram Sydrome (WS) is a rare autosomal recessive neurodegenerative disease that results from mutations in *WFS1* gene, encoding a mitochondria-associated ER membrane (MAM) protein called Wolframin (WFS1) located on the ER membrane. The mutant WFS1 protein causes ER dysregulation, which results in misfolded protein accumulation, increased ER stress, and stress-induced apoptosis [121]. Sarkar lab recently demonstrated that cell viability in WS patient iPSC-derived cortical neurons associated with loss of WFS1 protein was significantly reduced compare to control neurons, and that genetic restoration of the wild-type WS1 protein rescued neuronal viability [126]. Preliminary findings in the lab indicate autophagy dysfunction in WS arising from inhibition of autophagosome formation (unpublished data). Malfunction of autophagy is one of the hallmarks in a range of neurodegenerative diseases, whereas pharmacological upregulation of autophagy is beneficial in a various transgenic neurodegenerative disease models by [95, 137]. Moreover in Chapter 2, genetic evidence has been provided related to NAD depletion mediating cell death during autophagy deficiency whilst NAD boosters are cytoprotective by restoring mitochondrial bioenergetics and proteostasis [134, 191]. Furthermore, Sarkar lab recently reported mitochondrial dysfunction in WS patient iPSC-derived cortical neurons [126]. It is plausible that the autophagy defect is causing NAD depletion and affecting mitochondrial membrane potential ($\Delta\Psi_m$) in WS that could contribute to neurotoxicity in WS. Therefore, it is necessary to investigate the autophagy–NAD axis for targeting this process to develop novel therapeutic interventions for WS. Towards this, WS cell models including human neuroblastoma cell line with *WFS1* knockdown (*WFS1*^{KD}) and patient iPSC-derived cortical neurons with *WFS1* depletion were utilised.

3.2. Objectives

(1) Confirm autophagy dysfunction and assess the effects of autophagy inducers in rescuing disease-relevant phenotypes in WS iPSC-derived cortical neurons.

(2) Investigate NAD depletion and the effects on NAD boosters in rescuing disease-relevant phenotypes in WS iPSC-derived cortical neurons.

(3) Evaluate the effects of NAD boosters in a zebrafish model of WS (in collaboration with Benjamin Delprat in France).

3.3 Results

3.3.1. Autophagy inducers rescue defective autophagic flux in WS patient iPSC-derived neurons

Preliminary data in Sarkar lab generated by Malgorzata Zatyka and colleagues reveal impairment of autophagy at the level of autophagosome biogenesis. This was characterized by decrease in autophagosomes (LC3-II) and accumulation of autophagy substrate (p62) in WS neuroblastoma cell model, patient fibroblasts, and patient iPSC-derived cortical neurons (unpublished data; not shown). To study the biomedical importance of autophagy in clinically relevant WS cellular platforms, three WS patients (WS1, WS2, WS5) and two healthy controls (CT1, CT2) iPSC lines were utilised [192-194] to generate cortical neurons that were recently characterized by Sarkar lab for disease modelling and drug testing [126]. CT1 and WS1 lines were used for testing the effects of autophagy inducers. After 4 weeks of neuronal differentiation, the cellular identity of iPSC-derived neurons was confirmed by immunostaining of the neuronal markers, TUJ1 and MAP2 (**Figures 3.1 A, C**). Immunofluorescence analysis showed that WS1 iPSC-derived neurons had marked reduction of LC3 puncta (**Figures 3.1 A, B**) and substantial accumulation of p62 puncta (**Figures 3.1 C, D**) in TUJ^{+} or $MAP2^{+}$ neurons, compared to CT1 iPSC-derived neurons. These data confirm the defective autophagy phenotype in accordance to what was observed in various WS cell models (unpublished data by Zatyka and colleagues in Sarkar lab).

To evaluate the effects of autophagy inducers, two FDA-approved drugs that are blood-brain-barrier penetrant were used for proof-of-principle study. These include rapamycin (induces autophagy by mTORC1 inhibition) [4, 45, 47] and carbamazepine (which induces

mTOR-independent autophagy by lowering inositol and IP_3 levels) [4, 49] , both of which were protective in another rare, neurodegenerative, lysosomal storage disorder called Niemann-Pick type C1 (NPC1) disease [195]. Rapamycin and carbamazepine induced autophagy in WS1 neurons as evident from increase in LC3 puncta (**Figures 3.1 A, B**), concomitant to reduction of p62 puncta in WS1 neurons to levels that of control neurons (**Figures 3.1 C, D**). These data suggest that autophagy inducers could rescue the defective autophagic flux in WS patient-derived, disease-affected neuronal cells.

3.3.2. Autophagy inducers restore proteostasis and mitochondrial membrane potential in WS patient iPSC-derived neurons

As per the findings from Chapter 2, some of the deleterious consequences arising from loss of autophagy include impairment in proteostasis and mitochondrial function [134, 191]. Autophagy is the primary clearance route for aggregated proteins (by aggrephagy) and damaged mitochondria (by mitophagy), and therefore malfunction of this degradative process leads to accumulation and these unwanted cellular materials that evoke proteotoxic stress and mitochondrial dysfunction as seen in many neurodegenerative diseases [95, 158, 184]. Since autophagy dysfunction occurs in WS, preliminary data generated by Malgorzata Zatyka and colleagues in Sarkar lab show that this phenotype is associated with aggresome accumulation and mitochondrial depolarisation in WS neuroblastoma cell model (unpublished). Moreover, mitochondrial dysfunction has been also reported by Zatyka and colleagues in WS patient iPSC-derived neuronal cell models [126]. Thus, the effects of autophagy inducers on these disease-relevant cellular phenotypes were next analysed in WS patient iPSC-derived cortical neurons.

As expected, aggresome accumulation (by ProteoStat fluorescence) and mitochondrial depolarisation (by TMRE fluorescence) were observed in WS1 neurons as compared to CT1 neurons (**Figures 3.2 A-C**). Both rapamycin and carbamazepine significantly rescued these phenotypes in WS1 neurons to levels comparable to that in CT1 neurons (**Figures 3.2 A-C**). Collectively, these data suggest that autophagy dysfunction, aggresome accumulation. and mitochondrial depolarisation in WS could be rescued to normal levels after autophagy induction.

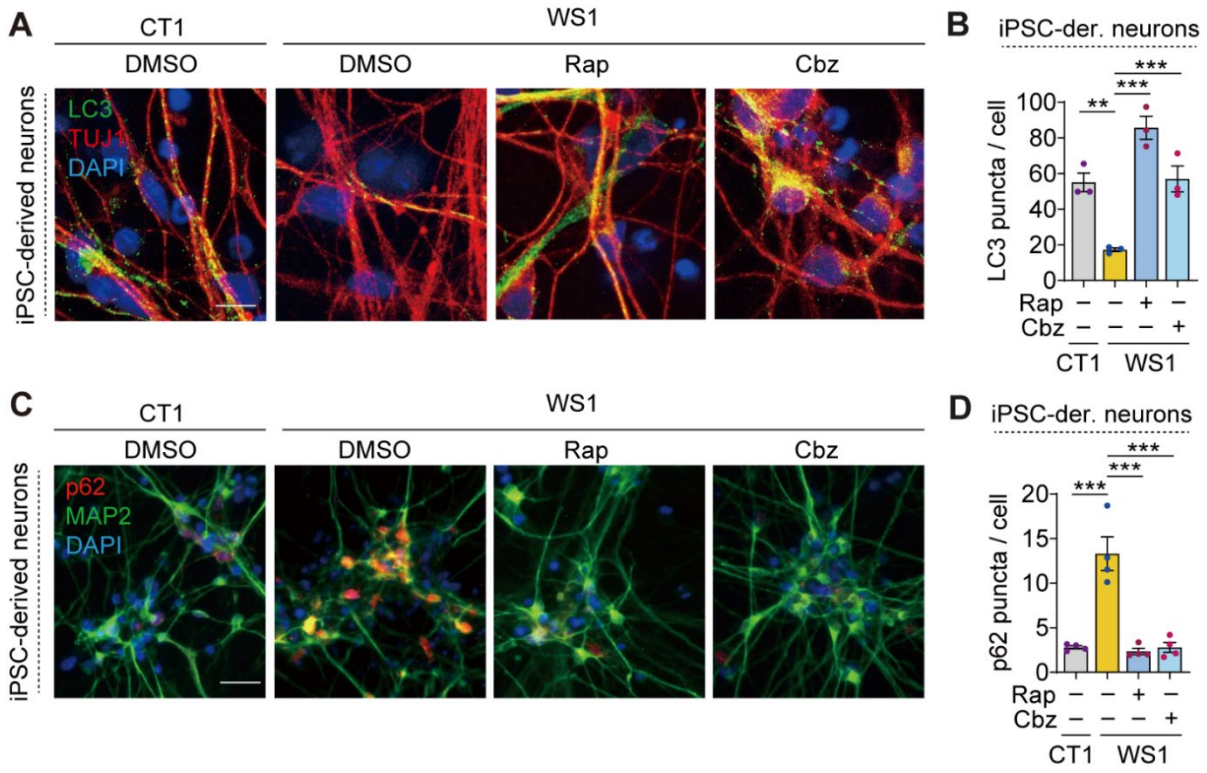

Figure 3.1. Autophagy inducers rescue the defective autophagic flux in WS patient iPSC-derived neurons.

(A, B) Immunofluorescence images (A) and quantification (B) of LC3 puncta in TUJ1⁺ cells in CT1 and WS1 iPSC-derived cortical neurons, where WS1 neurons were treated with or without 200 nM rapamycin (Rap) or 50 μM carbamazepine (Cbz) for the last 6 days of the 4-weeks neuronal differentiation period.

(C, D) Immunofluorescence images (C) and quantification (D) of LC3 puncta in MAP2⁺ cells in CT1 and WS1 iPSC-derived cortical neurons, where WS1 neurons were treated with or without 200 nM rapamycin (Rap) or 50 μM carbamazepine (Cbz) for the last 6 days of the 4-weeks neuronal differentiation period.

Graphical data are mean ± SEM of n = 3-4 biological replicates as indicated (B, D). P values were calculated by one-way ANOVA followed by multiple comparisons with two-stage linear step-up procedure of Benjamini, Krieger and Yekutieli on three independent experiments (B, D). *p < 0.05; **p < 0.01; ***p < 0.001. Scale barS: 50 μm (A), 100 μm (C).

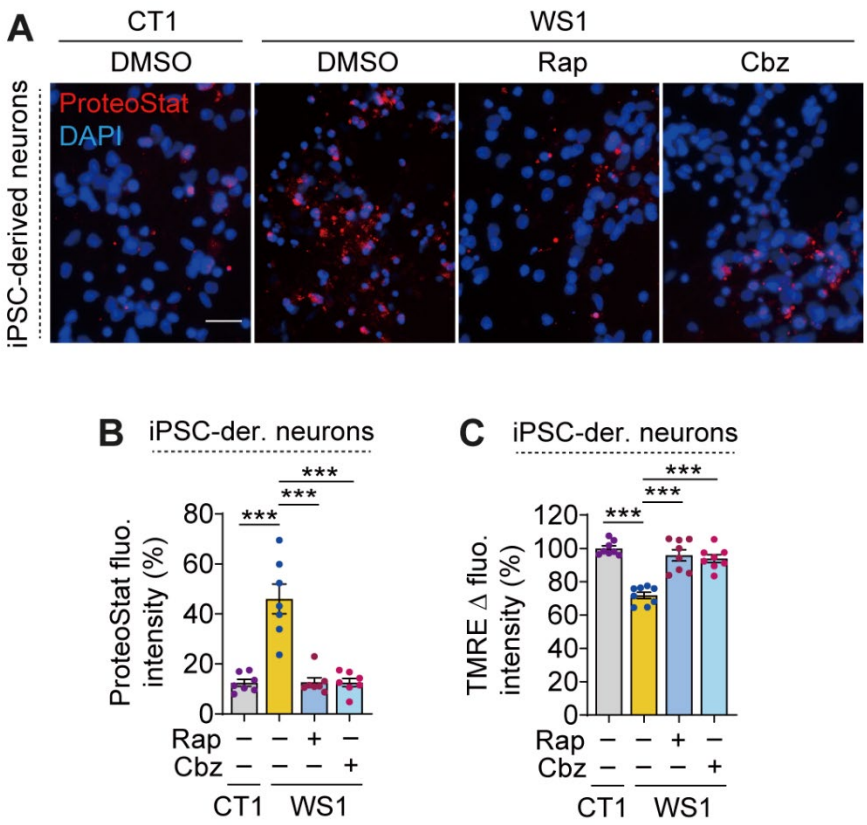

Figure 3.2. Autophagy inducers rescue aggresome accumulation and mitochondrial depolarisation WS patient iPSC-derived neurons.

(A, B) Fluorescence images of ProteoStat staining for aggresome detection (A) and quantification of ProteoStat fluorescence intensity in arbitrary units (a.u.) (B) in CT1 and WS1 iPSC-derived cortical neurons, where WS1 neurons were treated with or without 200 nM rapamycin (Rap) or 50 µM carbamazepine (Cbz) for the last 6 days of the 4-weeks neuronal differentiation period.

(C) Measurement of mitochondrial membrane potential by TMRE Δ fluorescence intensity in CT1 and WS1 iPSC-derived cortical neurons, where WS1 neurons were treated with or without 200 nM rapamycin (Rap) or 50 µM carbamazepine (Cbz) for the last 6 days of the 4-weeks neuronal differentiation period.

Graphical data are mean ± SEM of n = 7-8 biological replicates as indicated (B, C). P values were calculated by one-way ANOVA followed by multiple comparisons with two-stage linear step-up procedure of Benjamini, Krieger and Yekutieli on three independent experiments (B, C). ***p < 0.001. Scale bar: 20 µm (A).

3.3.3. Autophagy inducers improve cell viability in WS patient iPSC-derived neurons

Having demonstrated that pharmacological induction of autophagy could rescue various disease-related phenotypes in WS patient iPSC-derived cortical neurons, the cytoprotective effects of FDA-approved autophagy inducers on neuronal survival were further analysed. Cell death was measured by TUNEL staining for apoptotic nuclei in $TUJ1^+$ neurons and luminescence-based cytotoxicity assay, which showed that WS1 neurons exhibited much higher $TUNEL^+$ apoptotic nuclei and cytotoxicity compared to CT1 neurons (**Figures 3.3 A-C**). Concomitant to rapamycin and carbamazepine restoring autophagic flux (**Figures 3.1 A-D**), both these autophagy inducers reduced $TUNEL^+$ apoptotic nuclei and cytotoxicity in WS1 neurons to basal cell death level as seen in CT1 neurons (**Figures 3.3 A-C**). These data suggest that induction of autophagy is cytoprotective in improving the survival of WS patient-derived neurons, and thus could be a potential therapeutic strategy.

3.3.4. NAD depletion in WS patient iPSC-derived neurons

In Chapter 2, the cytotoxicity underlying autophagy deficiency in *ATG5*$^{-/-}$ hESC-derived neurons was attributed to depletion of total NAD pool and the consequent mitochondrial depolarisation [134]. Recent study from Sarkar lab and the data above demonstrate mitochondrial dysfunction in WS patient iPSC-derived neurons [126]. Therefore, the levels of intracellular NAD was examined in WS cell models that are associated with autophagy malfunction. NAD levels were measured by a colorimetric assay that has been previously used [134]. Both NAD^+ and NADH levels were substantially lower in *WFS1*^{KD} neuroblastoma cells and WS patient iPSC-derived cortical neurons, compared to their respective control counterparts (**Figures 3.4 A, B**). For the data in iPSC-derived neuronal cell model, 2 controls and 3 WS lines were used (**Figure 3.4 B**). These data demonstrate NAD depletion in WS that is possibly arising from the autophagy defect since autophagy is involved in the maintenance of cellular NAD levels [134, 191]. Overall, these findings highlight that the NAD depletion phenotype is a common feature between the genetic model of autophagy deficiency (*ATG5*$^{-/-}$) and the disease model of autophagy dysfunction (such as WS). Indeed, NAD depletion has also been reported in ageing and other neurodegenerative conditions associated with defective autophagy [76, 95].

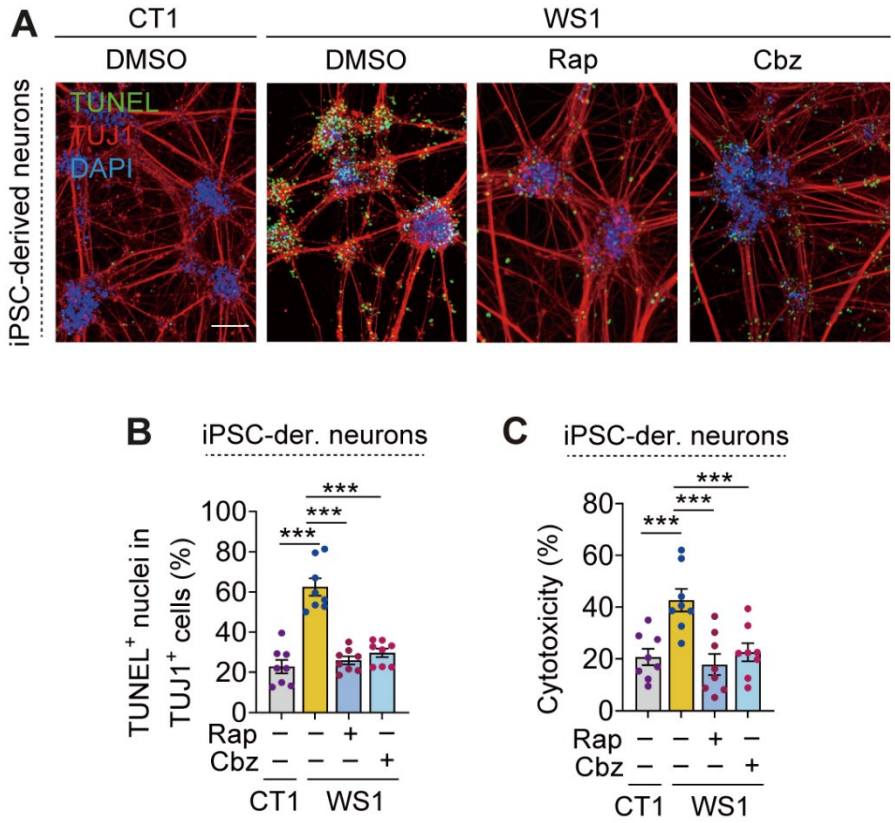

Figure 3.3. Autophagy inducers rescue cell death in WS patient iPSC-derived neurons.

(A-C) Immunofluorescence images (A) and quantification (B) of TUNEL⁺ apoptotic nuclei in TUJ1⁺ cells, and cytotoxicity assay (C) in CT1 and WS1 iPSC-derived cortical neurons, where WS1 neurons were treated with or without 200 nM rapamycin (Rap) or 50 μM carbamazepine (Cbz) for the last 6 days of the 4-weeks neuronal differentiation period.

Graphical data are mean ± SEM of n = 8 biological replicates as indicated (B, C). P values were calculated by one-way ANOVA followed by multiple comparisons with two-stage linear step-up procedure of Benjamini, Krieger and Yekutieli on three independent experiments. ***p < 0.001. Scale bar: 100 μm (A).

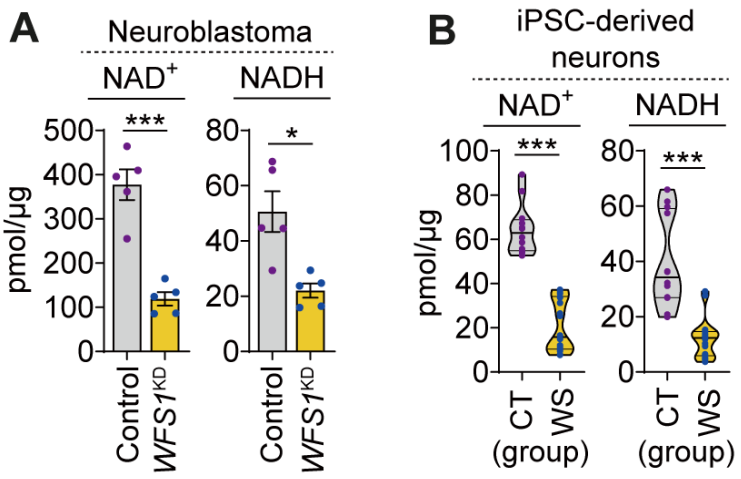

Figure 3.4. Depletion of intracellular NAD levels in WS neuroblastoma cell model and patient iPSC-derived neurons.

(A) Measurement of NAD^+ and NADH levels by colorimetric assay in control and *WFS1*^{KD} (*WFS1* knockdown) human neuroblastoma cell lines.

(B) Measurements of NAD^+ and NADH levels by colorimetric assay in CT1 and WS1 iPSC-derived cortical neurons after 4 weeks of neuronal differentiation.

Graphical data are mean ± SEM (A) or violin plots with line at median (B) of n = 5–8 biological replicates as indicated. P values were calculated by unpaired two-tailed Student's t test between the sample groups on three independent experiments (A, B). *p < 0.05; ***p < 0.001.

3.3.5. NAD boosters rescue defective autophagy and improve proteostasis in WS patient iPSC-derived neurons

Boosting intracellular NAD levels via NAD biosynthetic pathways by supplementation with NAD precursors rescued the abnormal mitochondrial and proteostasis phenotypes, and improved cell survival in autophagy-deficient cells [134, 191]; as described in Chapter 2. Therefore, the effects of various NAD boosting compounds were investigated in the context of WS patient-derived, disease-affected neurons that are associated with autophagy and NAD deficits. This study has the potential to enable the development of new therapeutic intervention for WS and related rare neurodegenerative diseases. The NAD supplementation strategy used involves nicotinamide (NAM), nicotinamide mononucleotide (NMN), nicotinamide riboside (NR), and dihydronicotinamide riboside (NRH) (**Figure 3.5 A**). These NAD boosters, some of which are used as nutritional supplements, have been shown to elevate intracellular NAD levels *in vitro* or *in vivo* in various cell and animal models [172, 196, 197].

Initial study was done to analyse the effects of NAD boosters on the defective autophagy phenotype in WS patient iPSC-derived cortical neurons. Interestingly, all the NAD boosters significantly increased LC3 puncta and decreased p62 puncta in WS1 neurons compared to untreated WS1 neurons (**Figures 3.5 B, C**), suggesting that boosting NAD improved autophagic flux in WS neurons. Next, the effects of NAD boosters on aggresome accumulation in WS neurons was analysed by ProteoStat staining. The rescue effect of the NAD boosters on autophagy was concomitant to reduction in ProteoStat staining in WS1 neurons (**Figures 3.5 E, F**), suggesting that increasing cellular NAD levels lower the aggresome buildup and improve proteostasis in WS neurons. Collectively, these findings are of biomedical relevance not only for WS but also for a range of neurodegenerative diseases that are associated with autophagy and NAD deficits.

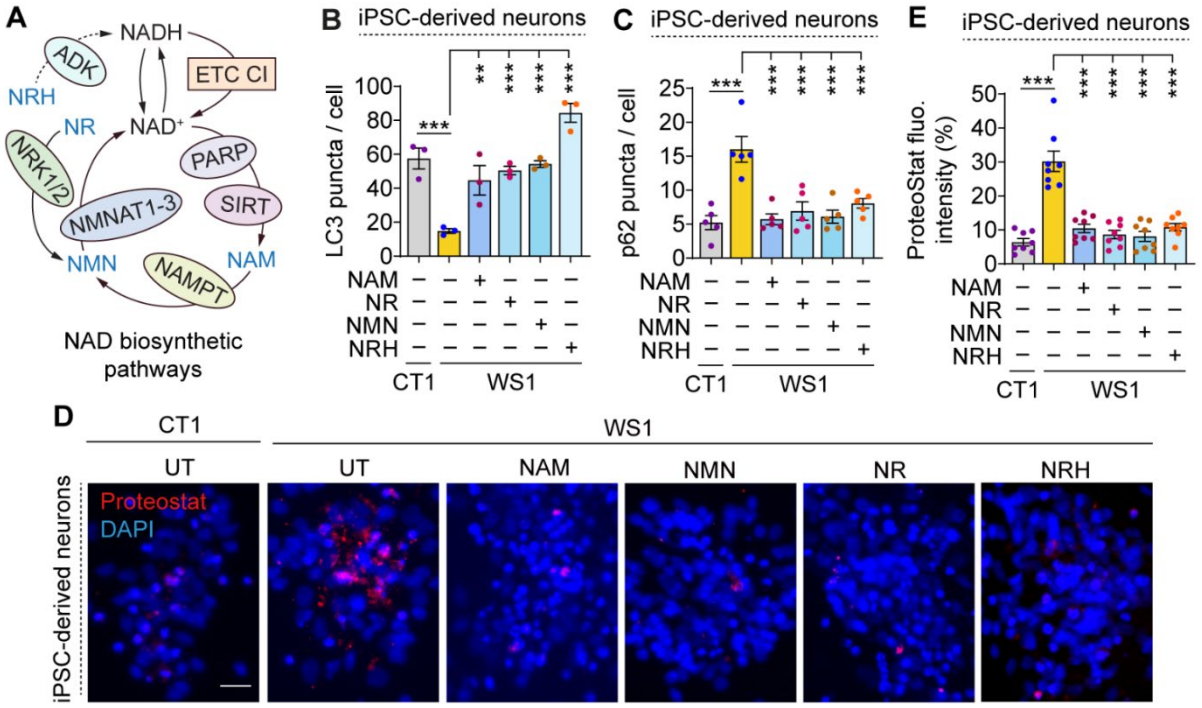

Figure 3.5. NAD boosters rescue the defective autophagic flux and proteostasis in WS patient iPSC-derived neurons.

(A) Schematic representation of NAD biosynthetic pathways where compounds used for modulating intracellular NAD levels are indicated.

(B, C) Quantification of LC3 (B) and p62 (C) puncta in CT1 and WS1 iPSC-derived cortical neurons, where WS1 neurons were treated with or without 1 mM NAM, 1 mM NMN, 1mM NR or 100 μM NRH for the last 6 days of the 4-weeks neuronal differentiation period.

(D, E) Fluorescence images of ProteoStat staining for aggresome detection (D) and quantification of ProteoStat fluorescence intensity in arbitrary units (a.u.) (E) in CT1 and WS1 iPSC-derived cortical neurons, where WS1 neurons were treated with or without 1 mM NAM, 1 mM NMN, 1mM NR or 100 μM NRH for the last 6 days of the 4-weeks neuronal differentiation period..

Graphical data are mean ± s.e.m. of n = 3–8 biological replicates as indicated. P values were calculated by one-way ANOVA followed by multiple comparisons with two-stage linear step-up procedure of Benjamini, Krieger and Yekutieli on 3 independent experiments (B, C, E). **p < 0.01; ***p < 0.001. Scale bar: 20 μm (D).

3.3.6. NAD boosters improve mitochondrial bioenergetics and cell survival in WS patient iPSC-derived neurons

Loss of autophagy was shown to mediate cytotoxicity via NAD depletion and the consequent mitochondrial dysfunction, whereas NAD precursor supplementation improved mitochondrial bioenergetics and cell viability in autophagy-deficient cells [134, 191]; as described in Chapter 2. Since impairment of autophagy (unpublished data) and mitochondrial function [126] occur in WS, the effects of NAD boosters on $\Delta\Psi_m$ and mitochondrial bioenergetics were analysed in WS patient iPSC-derived cortical neurons. Measurement of mitochondrial respiration by Seahorse analyzer (performed by Samuel Lara Reyna at University of Birmingham) revealed that WS1 neurons exhibited a marked reduction in basal and maximal respiration, ATP production, and spare respiratory capacity compared to the control CT1 neurons (**Figure 3.6 A**), suggesting a deficit in mitochondrial bioenergetics in WS as recently reported [126]. Treatment with NAD boosters such as NAM, NR, NMN, and NRH significantly improved these mitochondrial respiratory parameters in WS1 neurons, as seen in comparison to the untreated WS1 neurons (**Figure 3.6 A**). Moreover, these NAD boosters completely restored $\Delta\Psi_m$ in WS1 neurons that was associated with mitochondrial depolarisation, as measured by TMRE fluorescence (**Figure 3.6 B**). These data suggest that supplementation with NAD precursors rescued mitochondrial dysfunction in WS.

Finally, the effects of NAD boosters on cell viability was analysed in WS1 neurons, which exhibited higher cytotoxicity compared to CT1 neurons (**Figure 3.6 C**). All the NAD boosters significantly reduced cytotoxicity in WS1 neurons as compared to untreated WS1 neurons (**Figure 3.6 C**), suggesting that boosting NAD increased the survival of WS patient-derived neuronal cells. The cytoprotective effects of NAD boosters in WS1 neurons was effective in lowering cytotoxicity to basal levels as seen in CT1 neurons (**Figure 3.6 C**). In a nutshell, these data collectively highlight the potential of NAD boosting compounds for the treatment of WS that could be generalisable to related neurodegenerative diseases.

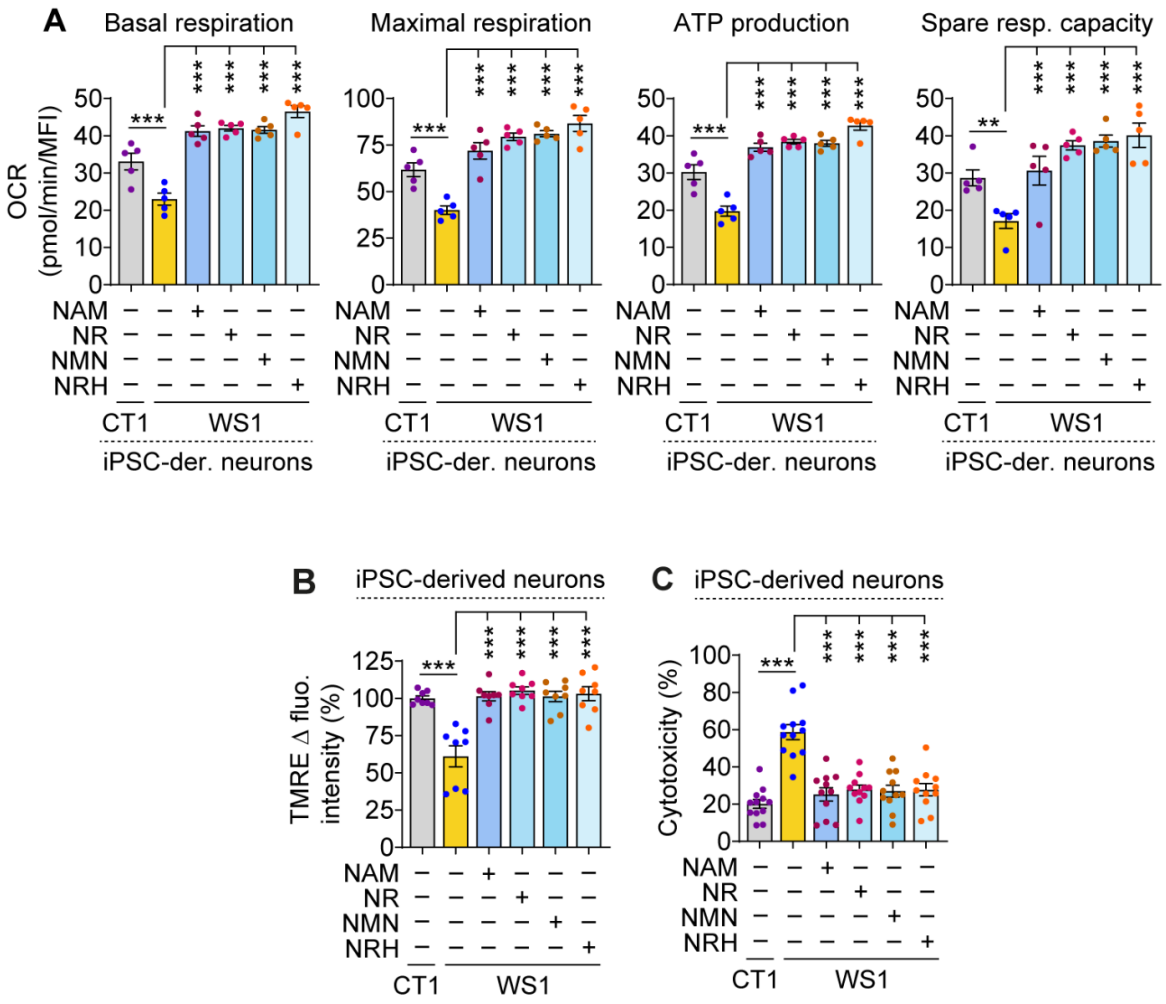

Figure 3.6. NAD boosters rescue mitochondrial bioenergetics and cell viability in WS patient iPSC-derived neurons.

(A) Measurements of post-mitochondrial stress test of the basal respiration, maximal respiration, ATP production, and spare respiratory capacity by Seahorse analyzer in CT1 and WS1 iPSC-derived cortical neurons, where WS1 neurons were treated with or without 1 mM NAM, 1 mM NMN, 1mM NR or 100 µM NRH for the last 6 days of the 4-weeks neuronal differentiation period *(Seahorse analysis done with Samuel Lara-Reyna).*

(B, C) Measurement of $\Delta\Psi_m$ by TMRE Δ fluorescence intensity (B) and cytotoxicity assay (C) in CT1 and WS1 iPSC-derived cortical neurons, where WS1 neurons were treated with or without 1 mM NAM, 1 mM NMN, 1mM NR or 100 µM NRH for the last 6 days of the 4-weeks neuronal differentiation period.

Graphical data are mean ± s.e.m. of n = 5-12 biological replicates as indicated. P values were calculated by or one-way ANOVA followed by multiple comparisons with two-stage linear step-up procedure of Benjamini, Krieger and Yekutieli on three independent experiments (A-C). **p < 0.01; ***p < 0.001.

3.3.7. NAD boosters rescue disease-relevant phenotype in WS zebrafish model

Having demonstrated the therapeutic benefits of NAD boosters in patient-derived neuronal cell model of WS, their efficacy in an *in vivo* model of WS was further investigated. Drug testing experiments were carried out in a zebrafish model of WS with knockout (KO) of *wfs1* gene (*wfs1ab*^{KO}) [198], in collaboration with Benjamin Delprat at the University of Montpellier in France. The use of zebrafish model for rare genetic diseases offers unique advantage over other *in vivo* models pertaining to high-throughput phenotypic capacity for therapeutic screening [199].

WS zebrafish larvae at 5 days post fertilization (dpf) had the deleterious phenotype of hyperlocomotion when their response to light variation was assessed using a visual motor response test, compared to the wild-type (WT; *wfs1ab*^{WT}) zebrafish larvae [198] (**Figures 3.7 A-D**). This is a disease-relevant phenotype since WS is associated with optic atrophy causing vision loss, apart from widespread brain atrophy [200, 201]. The NAD boosters assessed in the WT and WS zebrafish models include NAM, NMN, NR, and NRH [172, 202]. Supplementation with these NAD precursors significantly reduced the hyperlocomotion phenotype in *wfs1* KO animals at multiple doses without affecting the locomotion in WT animals (**Figures 3.7 A-D**). Such a rescue effect is expected from an efficient drug in this assay, which was the case for the NAD boosting compounds. Collectively, the findings from *in vitro* and *in vivo* models of WS suggest that NAD boosters are beneficial and could be used as a potential treatment strategy. In future, the effects of autophagy inducers will be tested in the WS zebrafish model.

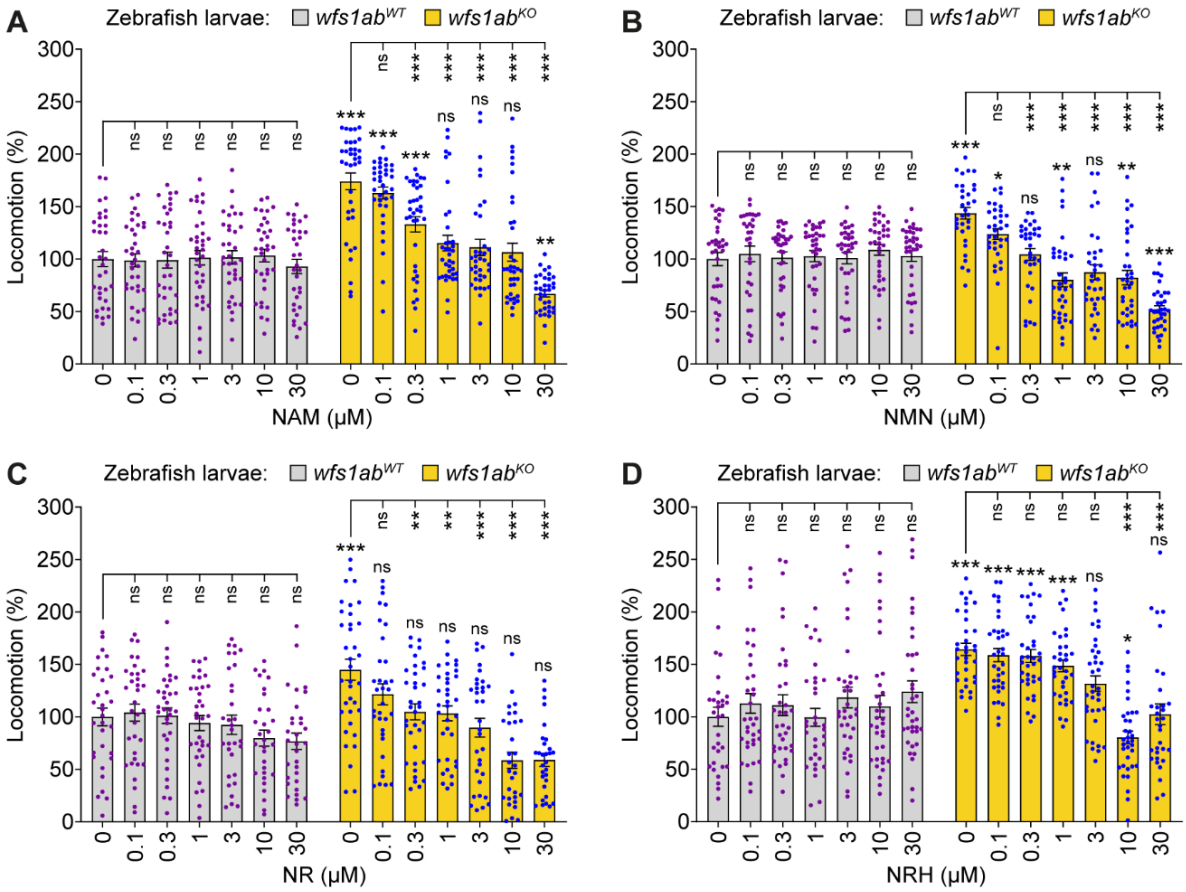

Figure 3.7. NAD boosters rescue hyperlocomotion phenotype on visual motor response (VMR) test in WS zebrafish model.

(A-D) Wild-type (WT) and *wfs1ab*^{KO} (WS) zebrafish larvae were tested for VMR at 5 dpf after 24 h treatment with NAM (A), NMN (B), NR (C), or NRH (D) at various concentrations as indicated from 4 dpf to 5 dpf. Results expressed as percentage of WT non-treated zebrafish larvae locomotion difference between light-off sessions and light-on sessions. NAD boosters reduced hyperlocomotion phenotype in WS zebrafish. For each condition, experiments were performed in 3 different sessions (n = 32-36 per condition). *Data generated and provided by Benjamin Delprat and colleagues (University of Montpellier, France).*

Graphical data are mean ± s.e.m. P values calculated by Boniferroni's multiparametric test after two-way ANOVA. Significance shown between WT vs WS groups with same treatment, and between non-treated vs drug treated groups with same genotype. ***p<0.001; **p<0.01; *p<0.05; ns: non-significant.

Chapter 4 :

Chemical screen to identify FDA-approved autophagy inducers for biomedical applications

Chapter 4: Chemical screen to identify FDA-approved autophagy inducers for biomedical applications

4.1. Introduction

Neurodegeneration is one of the most significant unmet medical need affecting society [1]. There are >100 rare inherited, early on-set neurodegenerative condition with no specific treatments [203]. Autophagy dysfunction has been demonstrated in several neurodegenerative diseases. Therefore, defective autophagy could be targeted as a shared mechanism to develop therapeutics for rare or common neurodegenerative conditions [1, 95, 104, 137]. Multiple lines of evidence have demonstrated that pharmacological modulation of autophagy is beneficial in cellular and transgenic animal models of neurodegenerative disease [1, 45, 47, 95]. Therefore, development of potent or cell-specific autophagy inducers is of tremendous biomedical relevance. Emerging studies indicate that there could be cell type-specific regulation of autophagy [152, 204], and hence it is pertinent to identify autophagy modulators in a manner relevant for human biology and disease.

Sarkar, Cohen and colleagues have previously generated a hESC model stably expressing a pH-sensitive fluorescent autophagy reporter (mCherry-EGFP-LC3) via genome engineering with zinc finger nuclease (ZFN) (unpublished data). The autophagy reporter hESC line can be differentiated into various isogenic human cellular platforms to study autophagy and identify autophagy inducers that are effective in the desired cell types. This hESC-based autophagy reporter system provides a physiologically relevant screening platform for identifying genetic and chemical modulators of autophagy by high-content microscopy. The high-confidence hits identified through this screening platform could be tested in clinically relevant iPSC-based disease models for potential clinical translation in future.

4.2. Objectives

(1) Generate and characterize autophagy reporter hESC-derived neural precursors (NPs) and neurons.

(2) Undertake chemical screen with FDA-approved drugs in autophagy reporter hESC-derived NPs to identify potent autophagy inducers for drug repurposing.

(3) Evaluate the therapeutic efficacy of FDA-approved autophagy-inducing drugs in WS patient iPSC-derived neurons.

4.3 Results

4.3.1 Characterisation of autophagy reporter hESC line

Sarkar, Cohen and colleagues have previously used ZFN to engineer the mCherry-EGFP-LC3 construct into the *AAVS1* (adeno-associated virus integration site 1) locus on chromosome 19 of the human genome to create a stable autophagy reporter hESC line (**Figure 4.1 A**). This pH-sensitive, tandem fluorescent-tagged autophagy reporter allowed the assessment of autophagic flux by monitoring autophagosome turnover [63]. In mCherry-EGFP-LC3 reporter system, the autophagosomes emit red $mCherry^{+}$ and green $EGFP^{+}$ signals that could be detected as yellow puncta ($mCherry^{+}/EGFP^{+}$) under fluorescent microscopy. After the autophagosomes fuse with lysomsomes, the acid-labile EGFP signal is quenched in the acidic enviroment and so the autolysosomes emit only red $mCherry^{+}$ signal ($mCherry^{+}/EGFP^{-}$) (**Figure 4.1 B**).

The pluripotency of the genome-edited mCherry-EGFP-LC3 hESCs was confirmed by immunofluorescence analysis of the pluripotency markers, such as NANOG, OCT4, SOX2, and SSEA4 (**Figure 4.1 C**), suggesting that genome editing probably did not affect the pluripotency of the autophagy reporter hESC line. Additional characterization for pluripotency and autophagy reporter readout of the mCherry-EGFP-LC3 hESC line has been previously done by Elena Seranova and co-workers in Sarkar lab (unpublished data).

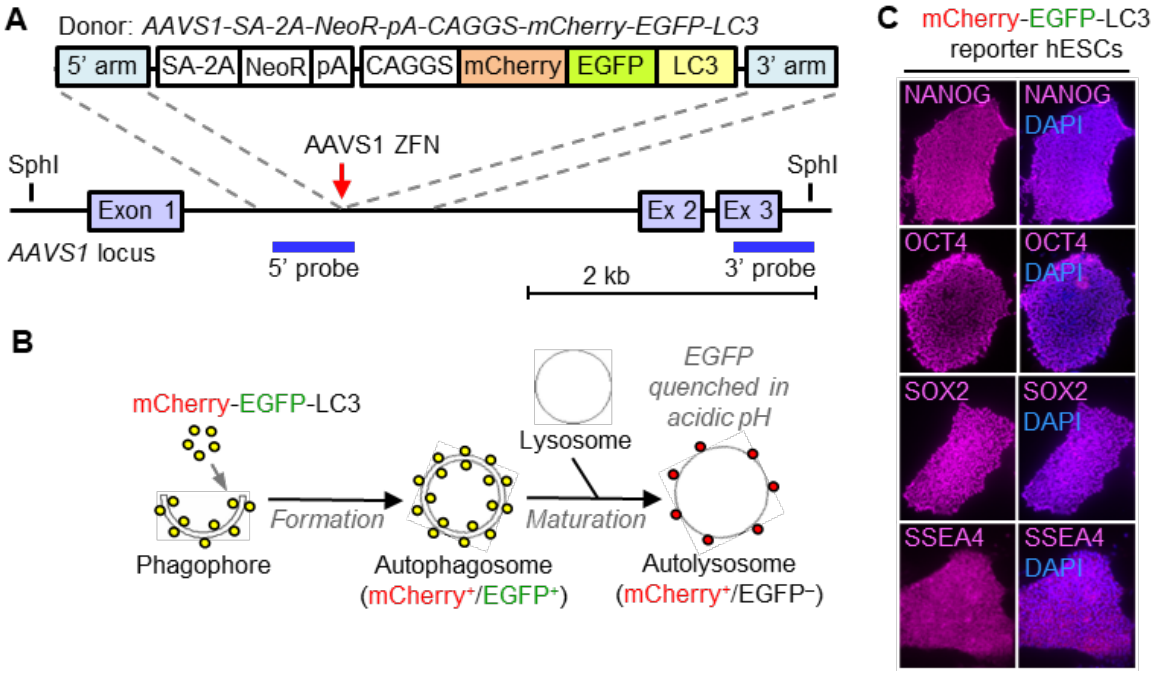

Figure 4.1. Generation and characterization of autophagy reporter hESC line.

(A) Schematic illustration of the genome editing strategy using ZFN for the generation of mCherry-EGFP-LC3 hESC line *(previously done by Sarkar, Cohen and colleagues)*.

(B) Schematic illustration of the pH-sensitive mCherry-EGFP-LC3 autophagy reporter, wherein autophagosomes and autolysosomes emit $mCherry^{+}/EGFP^{+}$ or $mCherry^{+}/EGFP^{-}$ signals, respectively.

(C) Immunofluorescence analysis of pluripotency markers, such as NANOG, OCT4, SOX2, and SSEA4 in mCherry-EGFP-LC3 hESCs. *Data generated with Elena Seranova*.

4.3.2. Generation and characterisation of autophagy reporter neural precursors and neurons from hESCs

Having established the autophagy reporter hESC model, the next step was to generate neuronal platforms for drug screening. The mCherry-EGFP-LC3 hESCs were initially differentiated into NPs via the 'dual-SMAD inhibition' method, and then into neurons, via the differentiation protocol as previously used and described in Chapter 2 (**Figure 2.4 A**) [1, 163, 205]. The morphology of mCherry-EGFP-LC3 hESCs and hESC-derived cells at different stages of the differentiation process was assessed and acquired via a fluorescent microscope (**Figures 4.2 A-D**). Briefly, mCherry-EGFP-LC3 hESCs cultured in StemFlex medium (**Figure 4.2 A**) were transferred to AggreWells (non-adherent microwell culture plates) for the production of defined-sized embryo bodies (EBs) on relatively large-scale (**Figure 4.2 B**). The EBs were cultured in NP medium (NPM) supplemented with human recombinant Noggin and SB431542 for the first 4 days (0-4). From day 5 to day 6, NPM supplemented with Noggin and bFGF was used. NPM supplemented with only bFGF was used sequentially in the following 7 days (days 7–14) for further NP differentiation. On day 14, NPs clusters were dissociated and plated onto poly-L-ornithine and laminin pre-coated culture dishes in NPM with bFGF and EGF. The NPs derived from hESCs via the dual SMAD inhibition method carry an anterior identity and commit to forebrain fates when cultured in the presence of bFGF and EGF. The mCherry-EGFP-LC3 hESC-derived NPs (**Figure 4.2 C**) were then terminally differentiated for 4 weeks into neurons (**Figure 4.2 D**) by growth factor withdrawal in the NP medium.

The cellular identity of the autophagy reporter hESC-derived NPs and neurons was confirmed by the immunostaining of cell-specific markers, such as NESTIN (for NPs) (**Figure 4.2 E**) and TUJ1 (neurons) (**Figure 4.2 F**). The differentiation of autophagy reporter hESCs into neuronal cells also imply that the genome editing procedure did not overtly affect the ability of this hESC line to be differentiated into somatic cell types. The hESC-derived neuronal cells provide a human-relevant experimental platform for compound screening to identify autophagy inducers for biomedical applications.

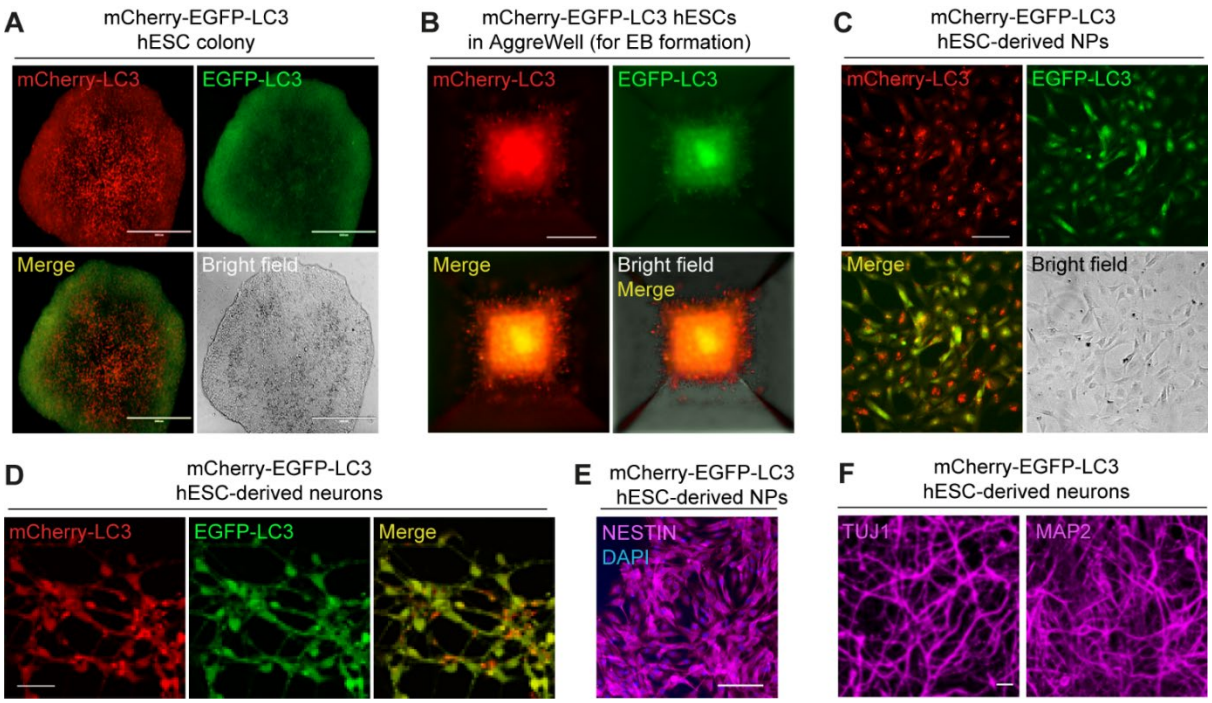

Figure 4.2. Differentiation of mCherry-EGFP-LC3 hESCs into neural precorsors and neurons.

(A-D) Brightfield and fluorescent images of mCherry-EGFP-LC3 hESCs (A) and hESC-derived embryoid body (EB) formation (B), neural precursors (C), and neurons (D).

(E, F) Immunofluorescence images of NESTIN (E), TUJ1 and MAP2 (F) in mCherry-EGFP-LC3 hESC-derived NPs (E) and neurons (F).

Scale bars: 400 μm (A-D), 100 μm (E, F).

4.3.3. Chemical screen to identify FDA-approved autophagy-inducing drugs in autophagy reporter hESC-derived neural precursors

After establishing the autophagy reporter hESC-derived cellular platforms, a mini compound screen was performed in the hESC-derived NPs to identify autophagy modulators for biomedical applications in neurodegenerative diseases (**Figure 4.3 A**). The choice of NPs over neurons was done because of the technical difficulty encountered in undertaking high-content imaging on neuronal cultures. Prior to drug screening, assessment was done for the autophagy reporter readout being amenable to chemical perturbations with known autophagy modulators. Treatment of the autophagy reporter NPs with rapamycin (autophagy inducer) showed an increase in autolysosomes ($mCherry^+/EGFP^-$), whereas bafilomycin A1 (autophagy blocker) treatment showed an increase in autophagosomes ($mCherry^+/EGFP^+$) and decrease in autolysosomes ($mCherry^+/EGFP^-$) (**Figure 4.3 B**).

For drug repurposing in rare early-onset neurodegenerative diseases, 24 FDA-approved and investigational drugs were selected based on their ability to cross the blood-brain-barrier and also for their autophagy induction capability reported in other systems (**Table 8**). The goal was to identify already-licensed drugs that are potent inducers of neuronal autophagy to enable clinical translation to patients in the future. Four different concentrations (0.1 µM, 1 µM, 10 µM, 100 µM) of each drug were used for treatment on the autophagy reporter hESC-derived NPs for 24 h. Some of the drugs exhibited toxicity at higher doses, mostly at 100 µM (**Figure 4.3 C**).

Additionally, a technical problem related to EGFP fluorescence was often encountered. The autophagy reporter NPs predominantly displayed mCherry fluorescence without much detectable EGFP fluorescence. One possibility for this issue could be due to the differentiation of the cells that affected the EGFP signal. Therefore, only the mCherry signal was quantified for the chemical screen. This approach is fine because it allowed measurement of all the autophagic vesicles including autophagosomes and autolysosomes. Moreover, since the drug library consisted of autophagy-inducing compounds, the high-confidence hits are expected to increase mCherry-LC3 signals as an indicator for upregulation of autophagy.

For the drug screening, mCherry-EGFP-LC3 hESC-derived NPs were seeded at a density of 3 x 10^4 cells per well in 96-well plates, followed by vehicle control (DMSO) or drug

treatment at different concentrations for 24 h, then fixed with 4 % formaldehyde and stained with DAPI nuclear staining. The cells were imaged by CX5 High-Content Screening (HCS) microscope using HCS Studio Cell Analysis software. Analysis was done for mCherry$^+$ puncta area instead of puncta number because the overlapping spots in the small cell size of NPs were difficult to separate for individual spot counting. The mCherry$^+$ puncta area per cell was quantified by Fiji ImageJ software. The quantification approach was automated using a Fiji groovy script [206], and individual nuclei >250 pixels were identified from the DAPI channel using a convolutional neural network-based approach called StarDist [arXiv:1806.03535]. The ilastik [207] pixel classifiers were trained to assist with segmentation of the cellular boundaries (cytoplasm) and the localization spots. Cell segmentations were refined by filling in holes smaller than 1000 pixels and discarding objects smaller than 2500 pixels. Two complementary approaches were used to obtain the measurement of mCherry$^+$ area per cell: (i) the number of objects (connected components) in the ilastik simple segmentation for the spot class was counted excluding objects smaller than 5 pixels; and (ii) the TrackMate plugin [208], which is a Laplacian of Gaussian detector and a quality threshold, was used to perform spot detection on the raw data with median filtering. The data (mCherry$^+$ puncta area/cell) was expressed as a percentage of the control condition (DMSO-treated) fixed at 100 %. Quantification was performed on >1000 cells per sample.

Amongst the various concentrations analysed, the screening data with 1 μM drug concentration, which is considered a clinically relevant dose in cell culture experiments, is presented here. The screen results showed that 20 out of 24 compounds at 1 μM concentration significantly increased mCherry$^+$ spot area per cell that is indicative of an upregulation of autophagy (**Figure 4.4 A**). For drug repurposing, the top 4 FDA-approved drugs that significantly increased mCherry$^+$ spot area were selected. These include carbamazepine, nimodipine, sodium valproate, and verapamil (**Figures 4.4 A, B**). These CNS-penetrant, FDA-approved drugs were also chosen because of their mTOR independency for autophagy induction, oral deliverability, and most importantly for known paediatric use (**Figure 4.4 C**), in order to treat children with rare early-onset neurodegenerative diseases such as Wolfram Syndrome (WS).

4.3.4. FDA-approved autophagy-inducing drugs are cytoprotective in WS patient iPSC-derived neurons

The therapeutic efficacy of the high-confidence screen hits, which include carbamazepine, nimodipine, sodium valproate, and verapamil, were analysed in WS patient-derived neuronal cells. These CNS-penetrant, FDA-approved, autophagy-inducing drugs have been previously reported for paediatric use (**Figure 4.4 C**), and therefore constitute potential drug candidates for the treatment of WS and other neurodegenerative diseases associated with autophagy dysfunction. The key disease-relevant phenotypes assessed were cell death and aggresomes, which were sunstantially elevated in the WS disease-affected neurons (**Figures 3.2 A, B and 3.3 A-C**). Carbamazepine, nimodipine, sodium valproate, and verapamil at 1 μM significantly reduced cell death and aggresome levels in WS patient iPSC-derived neurons (**Figures 4.4 D, E**), suggesting that all these FDA-approved autophagy inducers are cytoprotective in WS neurons.

Additional disease phenotypes and generalisability in other neurodegenerative diseases will be investigated in future. Overall, these data highlight the potential of repurposing already-licensed drugs for the treatment of WS. This drug repurposing approach could be of interest for developing therapy for rare diseases where therapeutic discovery is hampered due to the scarcity of patient population and their wide geographical spread, lack of disease mechanism knowledge, low commercial incentive, and long regulatory time-period for development of novel drugs.

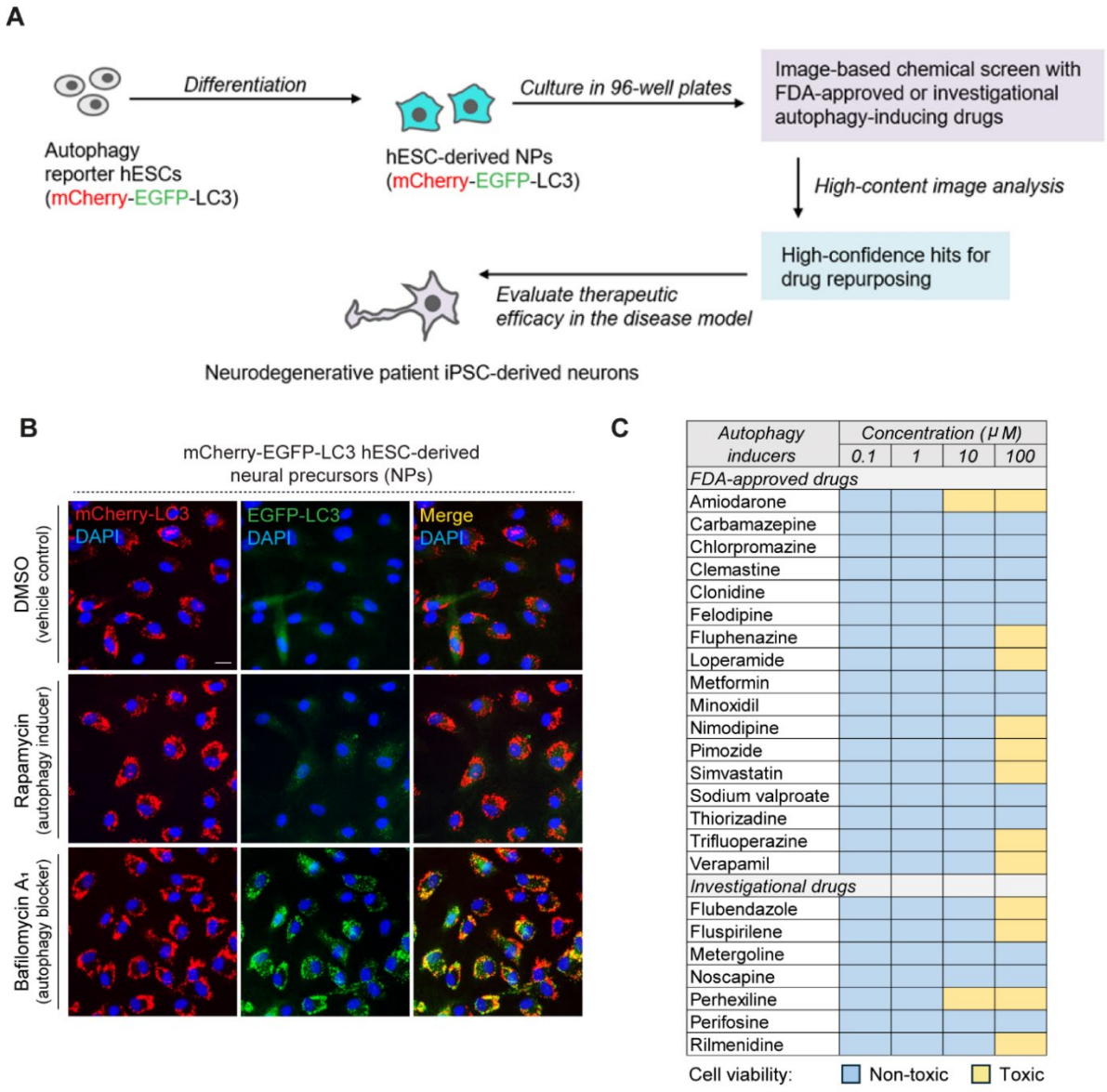

Figure 4.3. Image-based chemical screen with FDA-approved and investigational autophagy-inducing drugs in autophagy reporter hESC-derived neuronal precursors.

(A) Schematic illustration of the chemical screening approach and validation in disease models.

(B) Fluorescence images of mCherry-EGFP-LC3 hESC-derived NPs, treated with 0.1% DMSO (vehicle control), 200 nM rapamycin (autophagy inducer) or 400 nM bafilomycin A_1 (autophagy blocker) for 4 h.

(C) Table summarizing drug toxicity after 24 h treatment with the selected drug library at 4 different testing concentrations (0.1 μM, 1 μM, 10 μM, and 100 μM) in mCherry-EGFP-LC3 hESC-derived NPs. Blue: Not toxic; Yellow: Toxic.

Scale bar: 20 μm (B).

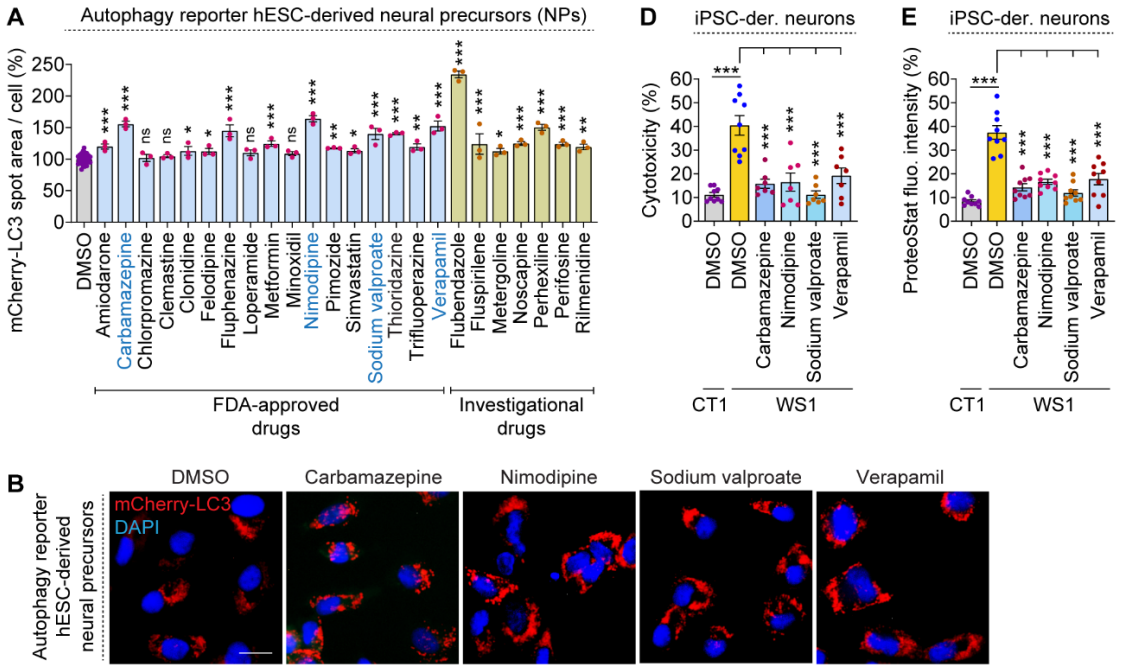

C CNS penetrance and peadiatric use of FDA-approved autophagy-inducing drugs from our chemical screen hits

FDA-approved drugs	CNS penetrant	Pediatric use		Key references	
		Yes / No	Dosage	For CNS	For pediatric use
Amiodarone	Yes	Yes (not licensed <3yr)	5-20 mg/kg/d	PMID: 26026931	https://bnfc.nice.org.uk/drugs/amiodarone-hydrochloride/
Carbamazapine	Yes	Yes	10-20 mg/kg/d (<6yr) 50-800 mg/d (6-12yr)	PMID: 32805338 PMID: 32104380	PMID: 475429 PMID: 27888506 PMID: 28971365
Clonidine	Yes	Yes (unlicensed use)	0.5-25 µg/kg	PMID: 21547166	https://bnfc.nice.org.uk/drugs/clonidine-hydrochloride/
Felodipine	Yes	Yes	2.5-5-10 mg	PMID: 20437557	PMID: 12700955
Fluphenazine	Yes	No	Not recommended	PMID: 30949404	https://www.empr.com/drug/fluphenazine/
Metformin	Yes	Yes	500-2000 mg/d	PMID: 36244266 PMID: 37242599	PMID: 30800563 PMID: 32921782
Nimodipine	Yes	Yes (investigational use)	1 mg/kg	PMID: 31560289	PMID: 25585913
Pimozide	Yes	Yes	0.05-4 mg/kg/d (2-12yr)	PMID: 32275862	https://www.pediatriconcall.com/drugs/pimozide/876
Simvastatine	Yes	Yes	5-40 mg/d	PMID: 22506129	PMID: 22477808
Sodium valproate	Yes	Yes	10-30 mg/kg/d	PMID: 3921665 PMID: 21499426	PMID: 18554460
Thioridazine	Yes	Yes	0.5-3 mg/kg/d (2-12yr)	PMID: 10991922	https://www.pediatriconcall.com/drugs/antipsychotics/thioridazine/96/997
Trifluoperazine	Yes	Yes	1-15 mg/d (6-12yr)	PMID: 38439960 PMID: 30258182	https://www.pediatriconcall.com/drugs/antipsychotics/trifluoperazine/96/1023
Verapamil	Yes	Yes	0.1-0.3 mg/kg	PMID: 23142723	https://www.pediatriconcall.com/drugs/verapamil/1041

Figure 4.4. Chemical screen hits that are FDA-approved autophagy-inducing drugs suitable for paediatric use rescue disease-relevant phenotypes in WS patient iPSC-derived neurons.
(A) Quantification of mCherry$^+$ spot area per cell in EGFP-LC3 hESC-derived NPs, treated with 0.1% DMSO (vehicle control) or 1 µM of FDA-approved or investigational drugs for 24 h. Quantification was performed on >1000 cells per sample. Key hits are highlighed.
(B) Fluorescence images of mCherry-EGFP-LC3 hESC-derived NPs, treated with 0.1% DMSO (vehicle control) or 1 µM of carbamazepine, nimodipine, sodium valproate or verapamil for 24 h.
(C) CNS penetrance and peadiatric use of FDA-approved autophagy inducers from screen hits.
(D, E) Cytotoxicity assay (D) and quantification of ProteoStat fluorescence for aggresome detection (E) in CT1 and WS1 iPSC-derived cortical neurons, where WS1 neurons were treated with DMSO or 1 µM of autophagy inducers for the last 6 days of the 4-weeks neuronal differentiation period.
Graphical data are mean ± SEM of n = 3–9 biological replicates. P values were calculated by one-way ANOVA followed by multiple comparisons with two-stage linear step-up procedure of Benjamini, Krieger, and Yekutieli on 3 independent (A, D, E). ***p < 0.001; **p < 0.01; *p < 0.05; ns: non-significant. Scale bar: 25 µm (B).

Chapter 5:

Discussion

Chapter 5: Discussion

5.1. Overview of key research findings

Some of the materials presented in this chapter has previously been published in my first-author research paper where I generated majority of the data:

Sun C, Seranova E, Cohen MA et al. and Sarkar S. NAD depletion mediates cytotoxicity in human neurons with autophagy deficiency. Cell Rep. 42(5): 112372 (2023) [134].

5.1.1. NAD depletion mediates cell death underlying autophagy deficiency

In summary, a human neuronal platform with autophagy deficiency was established by harnessing the differentiation potential of the hESC-based system. This human-relevant genetic model was used to study a fundamental question pertaining to how abrogation of autophagy compromises cell survival. Initially, a causal link was shown between loss of autophagy and cytotoxicity in human neurons [134], consistent with the genetic studies in mice demonstrating brain-specific abrogation of autophagy leading to neurodegeneration [154, 155]. This implies that dysfunctional autophagy reported in a range of neurodegenerative diseases contributes to disease pathology [1, 4, 95, 158].

Next, the possible cellular mechanisms behind this phenomenon were investigated. *ATG5*$^{-/-}$ hESC-derived neurons were associated with metabolic defects underlying cell death at the basal state. Increased glucose uptake and greater use of glucose in glycolysis and TCA cycle were found in *ATG5*$^{-/-}$ neurons as an attempt to deal with their metabolic stress, but this was inadequate to restore the depleted metabolites in these metabolic networks. The overall data in Chapter 2 suggest a specific metabolic defect, attributed to NAD depletion due to hyperactivation of NADases like PARPs and SIRTs, and the consequent mitochondrial depolarisation and bioenergetic deficit, as a potential mechanism leading to cell death due to autophagy deficiency (**Figure 5.1**) [134].

These observations are supported by the results that boosting intracellular NAD levels with bioavailable NAD precursors or other pharmacological agents improved mitochondrial function and cell viability in *ATG5*$^{-/-}$ neurons [134]. Moreover, loss of autophagy is associated with increased DNA damage and ROS [80, 178], which in turn can activate

PARPs and SIRTs to cause NAD exhaustion in *ATG5*$^{-/-}$ neurons. Interestingly, NAD boosters were also found to reduced aggresomes that are accumulated in autophagy-deficient cells [134], thereby supporting an extensive crosstalk between mitochondrial and protein homeostasis as reported in recent studies [185-188].

The phenomenon of NAD depletion and increased cell death was found to be common in proliferating *ATG5*$^{-/-}$ hESCs and post-mitotic *ATG5*$^{-/-}$ hESC-derived neurons [134]. Importantly, another recent study in collaboration further supports an evolutionarily conserved role of autophagy in maintaining NAD levels, where boosting NAD improved the survival of yeast, mouse cells and neurodegenerative disease patient-derived neurons with loss or malfunction of autophagy [191]. Additionally, it is plausible that other metabolic changes could also have detrimental effects [71], such as nucleic acid recycling defect in autophagy-deficient tumour-derived cell lines [166], and hyperactivation of the stress responsive transcription factor Nrf2 in autophagy-deficient mouse hepatocytes [155]. Despite the inability to maintain the intracellular pools of building blocks and energy carriers due to loss of autophagy, complex metabolic alterations can also occur, such as metabolic reprogramming in cancer cells via constitutive activation of Nrf2 [209, 210], which is induced by accumulation of p62 in autophagy-deficient cells [211]. Further studies are warranted to understand how these and other mechanisms integrate with the critical role of NAD depletion during autophagy deficiency.

Ageing and neurodegenerative diseases are associated with impaired autophagic activity, accumulation of misfolded protein aggregates, lower NAD levels and mitochondrial dysfunction [76, 95, 174, 184, 212, 213], whereas supplementation with NAD precursors is beneficial in transgenic animal and patient-derived iPSC models [75, 174, 214]. Moreover, enhancing NAD synthesis improves mitochondrial function and reduces protein aggregation [186, 188], which was also observed in *ATG5*$^{-/-}$ neurons [134]. Collectively, the data provide a mechanistic link between loss of autophagy, NAD depletion and cell death, and explain how pharmacologically boosting NAD levels can be cytoprotective in human neurons with autophagy deficiency by restoring mitochondrial function and proteostasis (**Figure 5.1**) [134].

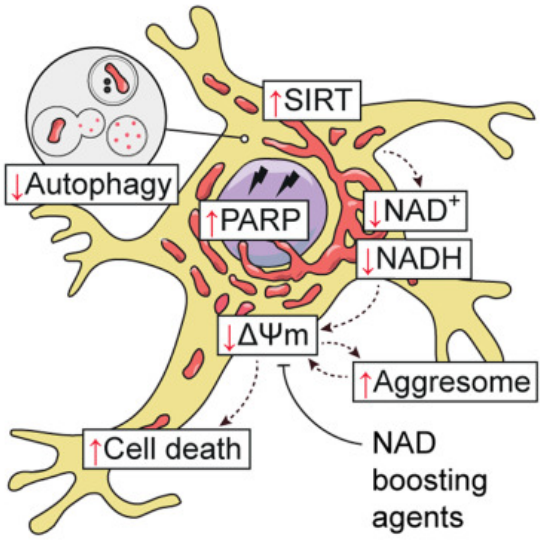

Figure 5.1. Summary of findings in Chapter 2.

Schematic representation of cell death cascade mediated by NAD depletion in human neurons with loss of autophagy, and the cytoprotective effects of NAD boosting agents.

5.1.2. Autophagy and NAD enhancers are cytoprotective in Wolfram Syndrome

Ongoing studies in Sarkar lab found defective autophagy in Wolfram syndrome (WS) due to inhibition of autophagosome formation in a human neuroblastoma cell model of WS with *WFS1* knockdown (*WFS1*^{KD}) and in patient-derived primary dermal fibroblasts (unpublished).To undertake biomedical studies in pre-clinical experimental systems, defective autophagy (unpublished) and increased cell death [126] were modelled as phenotypic readouts in disease-affected neurons differentiated from WS patient-derived iPSCs. Genetic rescue by restoration of the wild-type WFS1 protein ameliorated the autophagy defect (unpublished) and increased cell survival [126] of WS patient iPSC-derived neurons. Furthermore, autophagy inducers rescue various disease-related phenotypes in WS neuroblastoma cell model (unpublished).

In Chapter 3, pharmacological induction of autophagy with rapamycin (mTOR inhibitor) or carbamazepine (mTOR-independent autophagy inducer) in WS patient iPSC-derived neurons was found to restore autophagic flux, proteostasis, and $\Delta\Psi_m$, along with improvement in neuronal viability. These data suggest that autophagy induction could be a potential therapeutic strategy for WS. In agreement with this notion, multiple line of evidence have shown that such strategy is beneficial in transgenic models of various neurodegenerative diseases associated with autophagy dysfunction [1, 4, 94-96, 158].

As per the findings in Chapter 2 showing loss of autophagy mediating cell death via NAD depletion and the consequent mitochondrial dysfunction [134], this was also found to be the case for WS. In accordance with NAD deficit driving the cytotoxicity underlying autophagy deficiency [134, 191], NAD depletion was also observed in WS neuroblastoma cell model and patient iPSC-derived neurons. The defective autophagy–NAD axis was associated mitochondrial depolarisation [126] and aggresome accumulation (unpublished) in WS patient hiPSC-derived neurons. Similar findings were recently reported in collaboration for another rare, neurodegenerative, lysosomal storage disease called Niemann-Pick type C1 (NPC1) disease [215], which is also associated with autophagy dysfunction and NAD depletion [151, 191, 195].

Of biomedical relevance, boosting intracellular NAD levels by supplementation with NAD precursors, such as NAM, NMN, NR and NRH, restored NAD levels, proteostasis and $\Delta\Psi_m$, and improved neuronal survival in WS patient iPSC-derived neurons. Moreover, NAD boosters also rescued disease-relevant phenotype *in vivo* in a zebrafish model of WS. NAD boosting strategy has been demonstrated to be beneficial in certain neurodegenerative diseases [2, 215], and therefore, this approach could also be a therapeutic intervention for WS. Interestingly, augmenting cellular NAD levels also restored defective autophagic flux in WS patient-derived neurons. This could be possibly due to NAD impacting on metabolic pathways or modulating cellular enzymes for influencing autophagy. Nonetheless, this property of NAD boosters provide added benefit for their biomedical application in neurodegenerative diseases affected by autophagy.

Autophagy malfunction, NAD depletion, mitochondrial dysfunction, and protein aggregation are common phenotypes that are shared in many neurodegenerative diseases [2, 95, 104, 137]. Therefore, targeting the defective autophagy–NAD axis could be a potential therapeutic strategy in these pathological conditions. The findings from Chapter 3, demonstrating the therapeutic benefits with autophagy and NAD enhancers in WS patient-derived neuronal model, reinforce this idea as well as the generalisability of the therapeutic intervention involving autophagy and NAD enhancers.

5.1.3. Chemical screen identifies FDA-approved autophagy inducers for drug repurposing in neurodegenerative diseases

An autophagy reporter hESC model was established for chemical screening to identify autophagy inducers for biomedical applications. The neuronal cells generated from autophagy reporter hESC line provides a physiologically relevant human cellular platform. For drug repurposing in rare early-onset neurodegenerative diseases, a tailored library of FDA-approved or investigational drugs that are known to induce autophagy and cross the blood-brain-barrier was used for the high-content image-based drug screen. Due to technical difficulty with high-content imaging in neurons, the screen was undertaken in hESC-derived NPs.

Four high-confidence hits that are FDA-approved drugs were selected by taking into account their potency in inducing autophagy at clinically-relevant cell culture dose (1μM), suitability for paediatric use, and mTOR independency. These drugs were found to exert cytoprotective effects in reducing cell death and aggresomes in WS patient-derived neurons, highlighting potential new candidate drugs for the treatment of WS. These findings also warrant further investigation of rescuing other disease phenotypes in WS, and testing in additional neurodegenerative disease models to demonstrate generalisability. Collectively, the establishment of the autophagy reporter hESC-based experimental platforms and the preliminary drug screen informed potential candidate drugs for drug repurposing, and could also be useful for large-scale chemical screening to identify novel compounds. This is of biomedical relevance for therapeutic intervention using autophagy induction strategy in neurodegenerative diseases [1, 4, 94-96, 158].

5.2. Limitations of research

In Chapter 2, activation of SIRTs and PARPs were found to mediate NAD depletion, as determined by using chemical inhibitors and measuring the enzyme activity of SIRT1, SIRT2, PARP1 and PARP2. However, it was not feasible to confirm the role of these NADases by genetic approaches because gene knockdown in human neurons is technically challenging. Moreover, creating knockouts of the individual NADases in hESCs containing *ATG5* gene deletion and then differentiating the respective double knockout clones into neurons will be extremely challenging and time-consuming. It is also unclear

how this additional genetic manipulation will impact on the genome-edited *ATG5*$^{-/-}$ hESCs, which are already in stress exhibiting higher basal cytotoxicity.

In Chapter 3, the therapeutic benefits of autophagy and NAD enhancers were analysed in WS patient iPSC-derived cortical neurons. However, this 2D experimental system lacked any other brain cell types that could have a role in exerting non-cell autonomous effects. It was not possible to generate 3D cerebral organoids (mini brain) in the time frame of this PhD project because generation of this system is time-consuming and technically challenging. Nonetheless, the preclinical, patient-derived neuronal platform is generally used till now for disease modelling and drug testing [1].

In Chapter 4, the drug screen was undertaken in hESC-derived NPs instead of neurons. This is because high-content imaging in neurons cultured in 96-well plates was found to be technically challenging, such as loss of focus from well to well that affected proper image generation. Moreover, there were problems with EGFP signals in the differentiated cells like NPs. Since EGFP-LC3 expression was not always observed, the screen was done based on the mCherry-LC3 signals. Nonetheless, the high-confidence hits identified in NPs were effective in rescuing disease-relevant phenotypes in neurodegenerative disease patient-derived neurons.

5.3. Further work

Since autophagy promotes metabolic homeostasis by recycling cytoplasmic macromolecules and supplying the breakdown products into cellular anabolic processes [70, 165], loss of autophagy led to cell death and metabolic stress including NAD depletion as demonstrated in Chapter 2 [134]. Autophagy and NAD deficits along with compromised cell viability was also found in WS patient-derived neurons, as described in Chapter 3. Therefore, future work could involve unbiased LC-MS based metabolomics in patient-derived neurons of two rare, early-onset neurodegenerative disease like WS and NPC1 associated with defective autophagy, to further characterize the metabolic perturbations. This will enable to identify a common metabolic signature arising from autophagy deficiency in genetic model and autophagy dysfunction in disease model.

Another area of future research involve the identification of specific SIRTs and PARPs that are mediating NAD depleting underlying loss of autophagy, and further study their involvement in mediating NAD depletion in rare neurodegenerative disease models

including WS and NPC1. This will uncover specific targets for boosting cellular NAD by preventing NAD consumption. Further metabolic and mechanistic studies in patient-derived preclinical neuronal system will allow the identification of new targets for therapeutic intervention.

The defective autophagy–NAD axis is likely to be a shared patho-mechanism across a range of early-onset or late-onset neurodegenerative disease [2]. It will be interesting to investigate the correlation between autophagy and NAD deficits in these conditions. Importantly, evaluating the therapeutic efficacy of autophagy and NAD enhancers in these neurodegenerative disease models will demonstrate the generalisability of the therapeutic approach. This will have the potential to enable cluster trials in future involving groups of patients with more than one neurodegenerative disease conditions.

An important tool to develop in the near future is the establishment of cerebral organoid system for research [216]. This will be a more relevant system for disease modelling and drug testing. However, it is worth noting that the brain organoid system is time-consuming and technically challenging, and therefore it is more realistic to use this experimental platform for confirming the key findings from neuronal cells. Additionally, testing of candidate drugs could be done via collaboration in animal models of rare neurodegenerative diseases.

Chapter 6:

Materials and methods

Chapter 6: Materials and methods

Some of the materials presented in this chapter have been previously published in the following research and review articles where I contributed to the text as a first-author or co-author:

1. *Sun C, Seranova E, Cohen MA et al. and Sarkar S. NAD depletion mediates cytotoxicity in human neurons with autophagy deficiency. Cell Rep. 42(5):112372 (2023)* [134].
2. *Korsgen ME, Sun C, Seranova E et al. and Sarkar S. Analysis of autophagy deficiency and cytotoxicity in autophagy-deficient human embryonic stem cell-derived neurons. STAR Protoc. 4(3): 102529 (2023)* [217].
3. *Sun C, Rosenstock TR, Cohen MA and Sarkar S. Autophagy dysfunction as a phenotypic readout in hiPSC-derived neuronal cell models of neurodegenerative diseases. Methods Mol Biol. 2549: 103-136 (2022)* [218].
4. *Rosenstock TR, Sun C, Hughes GW, Winter K and Sarkar S. Analysis of mitochondrial dysfunction by microplate reader in hiPSC-derived neuronal cell models of neurodegenerative disorders. Methods Mol Biol. 2549: 1-21 (2022)* [219].

6.1. Culture of human embryonic stem cells

WIBR3 human embryonic stem cells (hESCs; *ATG5*$^{+/+}$) [220] and *ATG5*$^{+/-}$ (clone #1) and *ATG5*$^{-/-}$ (clones #1, #3, #4, #5 and #6) hESC lines [134] were cultured on a feeder layer or feeder-free. Briefly, hESCs were cultured on a feeder layer of inactivated mouse embryonic fibroblasts (MEFs) in hESC medium consisting of DMEM/F12 (Gibco), 15 % fetal bovine serum (HyClone), 5 % KnockOut Serum Replacement (Gibco), 1 % penicillin/streptomycin (Gibco), 1 % L-glutamine (Gibco), 1 % non-essential amino acids (Gibco), 4 ng/mL human recombinant basic fibroblast growth factor (bFGF; R&D Systems) and 0.1 mM β-mercaptoethanol (Sigma-Aldrich). For experimentation, the hESCs were cultured feeder-free on Geltrex (Gibco) basement membrane matrix in StemFlex Basal Medium supplemented with StemFlex 10X Supplement (Gibco) and 1 % penicillin/streptomycin (Gibco), or on Matrigel (Stem Cell Technologies) basement membrane matrix in mTeSR1 medium supplemented with mTeSR1 5X supplement (Stem Cell Technologies) and 1 % penicillin/streptomycin (Gibco). The hESCs were maintained on feeders or feeder-free in a humidified incubator with 5 % CO_2 and 5 % O_2 at 37 °C. For starvation-induced autophagy, hESCs and hESC-derived neural precursors were cultured in Hank's Balanced Salt Solution (HBSS; Gibco) as indicated. See the key resources table for further information on hESC lines, medium and reagents used in this study.

6.2. Genome editing for *ATG5* gene knockout in hESCs

The genome editing methodology was previously performed by Haoyi Wang and Sovan Sarkar. A pair of TALENs (transcription activator-like effector nucleases) targeting *ATG5* gene was designed and constructed as per the TALEN construct assembly guidelines.[63] The sequence recognized by *ATG5* TALEN F is GAAATGGTGAGTGAAT, and *ATG5* TALEN R binds to AGTATATACTTAATGCT, with a 15 bp spacer sequence between these two binding sites. Targeting donor vector was designed as PGK-Puro-pA or PGK-Neo-pA cassette flanked by ~700 bp homology arms lying upstream and downstream of *ATG5* exon 3. The WIBR3 hESC line was cultured in 10 μM ROCK inhibitor Y-27632 (Stemgent) for 24 h prior to electroporation. Cells were harvested and resuspended in phosphate buffered saline (PBS), and then electroporated with 40 μg of donor plasmids together with 5 μg of each TALEN-encoding plasmid via Gene Pulser Xcell System (Bio-Rad) at 250 V and 500 μF in 0.4 cm cuvettes. Cells were then plated on DR4 MEF feeders in hESC medium supplemented with ROCK inhibitor. Individual colonies were picked and expanded after 0.5 μg/mL puromycin (Gibco) or 400 μg/mL G418 selection (Gibco) for 10 to 14 days following electroporation. The correctly targeted clones were confirmed by Southern blot (NdeI digested) and Sanger sequencing.

6.3. Differentiation of hESCs into neural precursors and neurons

Differentiation of hESCs into neural precursor (NPs) and terminally differentiated human neurons was performed via the ‘dual SMAD inhibition’ method [163]. The hESC colonies were collected using 1.5 mg/mL collagenase type IV (Thermo Fisher Scientific), separated from the MEF feeder cells by gravity, and cultured in non-adherent suspension culture dishes (Corning) in NP medium (NPM) comprising of DMEM/F12 supplemented with 2 % B27, 1 % penicillin/streptomycin, 1 % L-glutamine and 1 % non-essential amino acids (all from Gibco) supplemented with 500 ng/mL human recombinant Noggin (Peprotech) and 10 μM SB431542 (Stemgent) for the first 4 days. NPM supplemented with 500 ng/mL Noggin and 20 ng/mL bFGF (R&D Systems) was used sequentially in the next 2 days (days 6–7), and NPM supplemented with only 20 ng/mL bFGF were used sequentially in the following 7 days (days 7–14) for further NP differentiation. At day 14, NPs clusters were dissociated and plated onto 100 μg/mL poly-L-ornithine (Sigma-Aldrich) and 14 μg/mL laminin (Sigma-Aldrich) pre-coated culture dishes in N2–B27 medium comprising of DMEM/F12 supplemented with 1 % N2, 2 % B27, 1 % penicillin/ streptomycin, 1 % L-

glutamine and 1 % non-essential amino acids (all from Gibco) supplemented with 20 ng/mL bFGF (R&D systems) and 20 ng/mL EGF (Gibco). After 7 days in culture, neural rosette-bearing cultures were dissociated using StemPro Accutase (Thermo Fisher Scientific) and subsequently expanded on poly-L-ornithine and laminin coated cell culture dishes at the density of ~1.5×10^6 cells per well (of 6-well plate) in N2B27 medium supplemented with 20 ng/mL bFGF and 20 ng/mL EGF. The NPs derived from hESCs via the dual SMAD inhibition method carry an anterior identity, and commit to forebrain fates when cultured in the presence of bFGF and EGF [164]. Proliferating NPs were passaged up to 4 times before induction of terminal differentiation into neurons by growth factor withdrawal in N2–B27 medium. Differentiated neurons were used for analysis 3–4 weeks after differentiation. See the key resources table for further information of the medium and reagents used for generation of NPs and neuronal differentiation.

6.4. Neuronal differentiation of Wolfram syndrome patient-derived hiPSC lines

The NPs and neurons were generated from previously established control (CT1, CT2), WS patient-derived (WS1, WS2, WS5), and rescued (WS5R) hiPSC lines [126, 193, 194] (**Table 2**). The hiPSCs were cultured and differentiated into NPs and then into neurons. NPs were seeded on poly-L-ornithine and Laminin coated plate and cultured in NP culture medium with DMEM/F12, neurobasal, N2B27 supplements, 0.1% β-mercaptoethanol, and 0.1% penicillin/streptomycin (Thermo Fisher Scientific) supplemented with 10 ng/mL of FGF-2 and epidermal growth factor (EGF) (Peprotech) and 10 μM of Y-27632 (StemCell Technologies). The medium was changed after 24 hours without Y-27632, then changed every 48 hours. The NPs were split when confluent with Trypsin-EDTA 0.05% (Thermo Fisher Scientific). Neuronal differentiation was induced by seeding the NSCs in poly-L-ornithine and Laminin plates in N2B27 medium without FGF-2 and EGF. On day 4, 10 μM DAPT (R&D Systems) was added to the medium to prevent cell proliferation, then change medium every 4 days [193, 194]. Neuronal differentiation is carried out for 4 weeks, and this differentiation protocol generates cortical neurons [126, 193].

6.5. Compound treatment and amino acid supplementation

Compounds used for modulating cellular NAD levels (**Table 3**): 1 mM Nicotinamide (NAM) (Sigma-Aldrich), 1 mM Nicotinamide riboside (NR) (ChromaDex), 1 mM Nicotinamide mononucleotide (NMN) (NMN Bio), 100 μM dihydronicotinamide riboside (NRH) (Provide

by Prof. Marie Migaud), 10 nM FK866 (Sigma-Aldrich), 20 μM Sirtinol (Cambridge Bioscience), 10 μM Olaparib (Cambridge Bioscience), 1 mM L-Tryptophan (Sigma-Aldrich). Amino acid supplementations include 1 mM of L-Alanine, L-Arginine, L-Glutamic acid, L-Glycine, L-Histidine, L-Leucine, L-Lysine, L-Methionine, L-Phenylalanine, L-Proline and L-Serine (all from Sigma-Aldrich). Compounds used for modulating autophagy were 200 nM Rapamycin and 50 μM Carbamazepine (Sigma-Aldrich). Compound used as chemical chaperone was 100 mM trehalose (Sigma-Aldrich). List of FDA-approved autophagy inducers used in the chemical screen are described in Methods section 6.29. Compound treatment was done in neurons for the last 6 days (with replenishment on day 3) of the 3-weeks (for hESCs) or 4-weeks (for hiPSCs) neuronal differentiation period. Compound treatment was done in hESCs and NPs for 2 days (with replenishment on day 1). See the key resources table for compounds and amino acids used in this study.

6.6. Immunoblotting analysis

Cell lysates were subjected to immunoblot analysis as per established methodology [195, 205, 221]. Cell pellets were lysed on ice in 2X Lysis Buffer comprising of 20 mM Tris-HCl pH 6.8, 137 mM NaCl, 1 mM EGTA, 1 % Triton X-100, 10 % glycerol and 25X Protease Inhibitor Cocktail (all from Sigma-Aldrich) (buffer made to 1X) for 30 min, boiled for 5–10 min at 100 °C. Protein concentration of the lysates was measured by Bio-Rad Protein Assay (Bio-Rad), and equal amounts of protein (10–40 μg) per sample were subjected to SDS–PAGE and immunoblot analysis [205, 221]. The blots were then incubated in Blocking Buffer (6 % non-fat milk powder in PBS-Tween 20) for 1 h at room temperature. For cleaved caspase-3 immunoblotting, cells were lysed with RIPA Lysis Buffer comprising of 50 mM Tris-HCl pH 8.0, 150 mM NaCl, 1 mM EDTA, 0.5 % deoxycholate, 1 % IGEPAL (all from Sigma-Aldrich), 0.1 % SDS (Bio-Rad) and Complete Protease Inhibitor Cocktail (Roche), sonicated and centrifuged at 14000 rpm for 30 min at 4 °C. The samples were subjected to SDS–PAGE on a 16.5 % gel, followed by wet transfer on nitrocellulose membrane, then membrane was blocked in 1 % glutaraldehyde solution (VWR Life Science) in TBS for 30 min and in Blocking Buffer for 1 h at room temperature. All the blots were incubated overnight in primary antibodies (see **Table 4** for the list and dilutions of primary antibodies and the cell types used upon) at 4 °C on an orbital shaker. The immunoblots were then probed with appropriate secondary antibodies (see **Table 4** for the list and dilutions of secondary antibodies) conjugated to horseradish peroxidase

(HRP) for 1 h at room temperature on an orbital shaker. The chemiluminescent signal was visualized using Amersham ECL or ECL Prime Western Blotting Detection Reagent and Amersham Hyperfilm ECL (GE Healthcare) via ECOMAX X-ray Film Processor (PROTEC). Densitometry analyses of immunoblots for the protein of interest relative to the loading control were done using ImageJ v1.48 (NIH) software. The data was expressed as a percentage of the control condition [151, 195, 205, 221]. See the key resources table for further information on primary and secondary antibodies used for immunoblotting analysis.

6.7. Immunofluorescence

Immunofluorescence analysis was performed as per established methodology [195, 205, 221]. Cells were washed in PBS, fixed with 4 % formaldehyde (Thermo Fisher Scientific) at room temperature for 15 min, permeabilised with 0.5 % Triton X-100 (Sigma-Aldrich) for 10 min (for all primary antibodies except LC3 antibody) or with pre-chilled methanol for 5 min (for LC3 antibody), and incubated with Blocking Buffer (5 % goat or donkey serum (Sigma-Aldrich) in PBS with or without 0.05 % Tween-20 depending on the antibody specifications) for 1 h at room temperature. Cells were then incubated overnight with primary antibodies (see **Table 5** for the list and dilutions of primary antibodies and the cell types used upon) at 4 °C, followed by incubation with appropriate Alexa Fluor conjugated secondary antibodies (see **Table 5** for the list and dilutions of secondary antibodies) for 1 h at room temperature. The coverslips were mounted on glass slides with ProLong Gold antifade reagent with DAPI (Invitrogen). See the key resources table for further information on the primary and secondary antibodies used for immunofluorescence analysis.

6.8. Image acquisition of fixed cells

Fluorescence images of fixed cells were acquired using EVOS FL Cell Imaging System (Thermo Fisher Scientific) with AMG 10x Plan FL and AMG 40x Plan FL lens, Leica DM6000 B (Leica Microsystems) with Leica DFC 350 FX R2 camera and with HC PL APO 40x/1.25 or HC PL APO 100x/1.40 oil immersion lens with Leica Application Suite X software (Leica Microsystems), or with Perkin Elmer UltraView spinning disk confocal system (Perkin Elmer) with an Orca-ER cooled–CCD camera (Hamamatsu) on a Zeiss Axiovert 200 (Carl Zeiss Inc.) with 63× 1.4NA plan-apochromat oil immersion lens using Volocity v6.1 software (Improvision).

6.9. Image analysis of pluripotency markers

Cells immunostained with antibodies for the respective pluripotency markers were imaged and analyzed for their fluorescence intensity relative to hESC colony area using ImageJ v1.41 software (NIH). The data was expressed relative to the control (*ATG5*$^{+/+}$) condition. Quantification was performed on ~25 colonies per sample.

6.10. Gene expression analysis

Total RNA from cells was extracted using Trizol (Ambion) followed by DNase treatment using the RNase-free DNase set (Qiagen) [222]. Reverse transcription PCR (RT-PCR) was performed using M-MLV Reverse Transcriptase (Promega) and quantitative PCR (qPCR) was performed using the CFX Connect Real-Time System (Bio-Rad) [222]. 25 µM of primers (primer sequences listed in **Table 6**) (Merck) were used in SYBR Green mastermix (Applied Biosystems) that was added to 5 ng of cDNA. Results were analysed using $2^{-\Delta\Delta Ct}$ method and were normalised to the expression of the housekeeping gene *GAPDH*.

6.11. TUNEL assay for apoptotic cells

Cells were stained with Click-iT Plus TUNEL Assay for in situ apoptosis detection, Alexa Fluor 488 dye (Invitrogen) (see key resources table), according to manufacturer's protocol. Cells were fixed with 4 % formaldehyde (Thermo Fisher Scientific) for 15 min, permeabilised with 0.25 % Triton X-100 (Sigma-Aldrich) for 20 min at room temperature and then washed with deionized water. Cells were incubated at 37 °C for 10 min in TdT reaction buffer, followed by incubation with TdT reaction mixture containing TdT reaction buffer, EdUTP, TdT enzyme for 60 min at 37 °C, washed with 3 % BSA, and finally incubated with Click-iT Plus TUNEL reaction cocktail for 30 min at 37 °C followed by washes with 3 % BSA. For detection of TUNEL^{+} apoptotic nuclei in neurons, cells were subjected to immunofluorescence by blocking with 3 % BSA (in PBS) followed by incubation with TUJ1 antibody (in 3 % BSA in PBS) overnight at 4 °C, and thereafter incubated with Alexa Fluor 594 secondary antibody for 1 h at room temperature. Coverslips were mounted on glass slides with ProLong Gold antifade reagent with DAPI (Invitrogen). The quantification of TUNEL^{+} apoptotic nuclei in TUJ1^{+} neuronal cells was performed via fluorescence microscopy [151]. The percentage of TUNEL^{+} nuclei was

calculated from the total number of TUJ1^{+} cells analysed (~200–300 cells per sample were analysed).

6.12. Cytotoxicity Assay

Cytotoxicity was measured with CytoTox-Glo Cytotoxicity Assay (Promega) (see key resources table), according to manufacturer's protocol. This luminescence-based cytotoxicity assay measures the extracellular activity of a distinct dead-cell protease when it is released from membrane-compromised cells. Cells were incubated with CytoTox-Glo Assay Reagent (comprising of Assay Buffer and AAF-Glo Substrate) for 15 min at room temperature in the dark, then luminescence was measured using EnSpire Multimode plate reader (Perkin Elmer) and the readings obtained were attributed to the basal cytotoxicity per well (first reading). To estimate cell population per well, cells were further incubated with Lysis Reagent (comprising of Assay Buffer and Digitonin) for 30 min at room temperature in the dark, after which luminescence was measured again (second reading). Cytotoxicity data were normalised by dividing the first reading (basal cytotoxicity per well) to the second reading (indicative of cell population per well) and expressed as a percentage.

6.13. DAPI staining for apoptotic nuclear morphology

For analyzing apoptotic nuclei morphology by DAPI staining in neuronal cells immunostained with TUJ1 antibody (neuronal marker), the percentage of apoptotic nuclei was calculated from the total number of TUJ1^{+} cells. Quantification was performed on ~150–200 cells per sample.

6.14. DNA damage analysis

Cells were immunostained with phospho-Histone H2A.X$^{(Ser139)}$ or 53BP1 along with TUJ1 (neuronal marker), and the frequency of γH2AX or 53BP1 puncta (DNA damage markers) was assessed by ImageJ v1.41 (NIH). Quantification was performed on ~200 cells per condition.

6.15. Cell proliferation analysis

Cells immunostained with antibodies for Ki-67 (cell proliferation marker) and OCT4 (pluripotency marker) were imaged and assessed for the percentage of Ki-67$^+$ cells in OCT4$^+$ hESCs using the ImageJ v1.41 software (NIH). Quantification was performed on ~100 cells per sample.

6.16. Proteostat aggresome assay

Analysis of aggresomes, which are inclusion bodies of aggregated proteins, was performed in cells using ProteoStat Aggresome Detection Kit (Enzo) (see key resources table) [186, 189]. Cells were fixed with 4 % formaldehyde (Thermo Fisher Scientific) for 15 min at room temperature and then permeabilised with 0.5 % Triton X-100 (Sigma-Aldrich) for 1 h. After washing with DPBS, cells were stained with ProteoStat Aggresome Dye (1:2000 in 1X Assay Buffer) and Hoechst 33342 Nuclear Stain (1:1000 in 1X Assay Buffer) overnight at 4 °C. Cells were washed with DPBS followed by mounting the cover slips onto glass slides with ProLong Gold antifade reagent (Invitrogen). Images were acquired using EVOS fluorescence microscope (Thermo Fisher Scientific) with a Texas Red filter for ProteoStat dye and a DAPI filter for nuclear signal. Quantification of ProteoStat fluorescence intensity was done in ~150–200 cells per sample using ImageJ v1.41 software (NIH).

6.17. Measurement of SIRT1, SIRT2, PARP1 and PARP2 enzyme activity

Cells were lysed with Lysis Buffer (20 mM Tris-HCl pH 7.4, 135 mM NaCl, 1.5 mM $MgCl_2$, 1 mM EGTA, 10 % glycerol, 0.1 % IGEPAL) followed by immunoprecipitation (IP) of SIRT1, SIRT2, PARP1 or PARP2 with the respective anti-SIRT1 (Abcam), anti-SIRT2 (Proteintech), anti-PARP1 or anti-PARP2 (Santa Cruz Biotechnology) antibody conjugated to Protein A Agarose beads (Invitrogen) (see **Table 7** for the list and concentrations of primary antibodies). For each IP reaction, the agarose beads were washed with lysis buffer, then incubated with 6 µg of the primary antibody in lysis buffer for 4 h at 4 °C, after which the beads–antibody complex was washed with lysis buffer and incubated with cell lysate (300 µg of total protein) overnight at 4 °C. The immunoprecipitate was centrifuged and washed, then directly used for SIRT1 and SIRT2 activity assay using Fluorometric SIRT1 or SIRT2 Activity Assay Kit (Abcam), or for PARP1 and PARP2 activity assay using HT Universal Colorimetric PARP Assay Kit (R&D Systems), according to manufacturers'

instructions. For SIRT1 and SIRT2 activity, measurement of fluorescence readout was performed for 30 min with 2 min interval to detect the saturating fluorescence reading by EnSpire Multimode microplate reader (Perkin Elmer). For PARP1 and PARP2 activity, measurement of absorbance was done using Infinite F50 microplate reader and data was processed using Magellan F50 Software (Tecan). Data were obtained as relative fluorescence (for SIRTs) or absorbance (for PARPs) units, and expressed as fold change relative to the control condition. See the key resources table for further information of the primary antibodies used for immunoprecipitation and the reagents used for enzyme activity assays.

6.18 NAD^+ and NADH measurements

NAD^+ and NADH measurements were done using NAD/NADH Quantitation Colorimetric Kit (BioVision) (see key resources table), according to manufacturer's instructions. Cells were washed with cold PBS, then lysed with NADH/NAD Extraction Buffer and immediately freeze-thawed twice on dry ice, centrifuged at 14000 rpm for 5 min at 4 °C. Half of the supernatant was incubated at 60 °C for 30 min to decompose the NAD and detect the NADH. Both halves of the supernatants were then cooled on ice, transferred into a 96-well plate, followed by incubation in Reaction Mix comprising of NAD Cycling Buffer and NAD Cycling Enzyme Mix for 5 min at room temperature. Then NADH Developer was added to each well and the reaction was left to cycle for 1–2 h at room temperature. Measurements of optical density (OD) at 450 nm using the EnSpire Multimode plate reader (Perkin Elmer) were performed every 20–30 min to detect the saturating OD, then normalized to protein concentration via Bio-Rad Protein Assay (Bio-Rad) to measure pmol/µg of NAD^+ and NADH.

6.19 ATP and ADP measurements

Measurements of ATP and ADP were done using ApoSENSOR ADP/ATP RatioBioluminescent Assay Kit (BioVision) (see key resources table), as per manufacturer's instructions. A Reaction Mix containing Nucleotide Releasing Buffer (NRB) and ATP monitoring enzyme was added in the wells of a white-walled 96-well plate and kept at room temperature for a few hours to burn residual ATP levels. Cells cultured in another 96-well plate were incubated with NRB for 5 min at room temperature to release

the ATP, and then the supernatant was transferred to appropriate wells of the white-walled 96-well plate. Luminescence was measured using EnSpire Multimode microplate reader (Perkin Elmer) for determining ATP levels, and again measured after adding ADP Converting Enzyme for determining ADP levels. Data were normalised to protein concentration via Bio-Rad Protein Assay (Bio-Rad) and expressed as a percentage of the control condition.

6.20. Mitochondrial $\Delta\Psi_m$ and ROS measurements

Measurements of mitochondrial membrane potential ($\Delta\Psi_m$) and reactive oxygen species (ROS) were performed with TMRE (Invitrogen) and CM-H_2DCFDA (Invitrogen), respectively [223, 224] . Briefly, cells were loaded with Microscopy Medium comprising of 120 mM NaCl, 3.5 mM KCl, 0.4 mM KH_2PO_4, 5 mM $NaHCO_3$, 1.2 mM $NaSO_4$, 20 mM HEPES and 15 mM glucose in dH_2O adjusted to pH 7.4 and supplemented with 1 mM $CaCl_2$ (all from Sigma-Aldrich), and incubated with 500 nM TMRE (for $\Delta\Psi_m$ measurement) and 20 µM CM-H_2DCFDA (for ROS measurement) for 1 h at 37 °C. The fluorescence signals of TMRE and CM-H_2DCFDA were acquired using EnSpire Multimode microplate reader (Perkin Elmer) for a period of 5 min to get basal fluorescence, and again for TMRE for another 5 min after the addition of 10 µM FCCP (fluorocarbonyl cyanide phenylhydrazone). The baseline fluorescence was calculated as the mean of the last 5 fluorescence readings before the addition of FCCP (for TMRE and CM-H_2DCFDA), and the delta (Δ) fluorescence was calculated by subtracting the basal fluorescence from the average of first 5 fluorescence readings after FCCP treatment (for TMRE only) [223, 224]. Data were obtained as relative fluorescence units, normalised to protein concentration via Bio-Rad Protein Assay (Bio-Rad), and expressed as a percentage of the control condition. See the key resources table for further information of the reagents used for mitochondrial $\Delta\Psi_m$ and ROS measurements.

6.21. Mitochondrial respiration measurement

Cells were seeded into an initial density of 8×104 cells per well in XF96 cell-culture microplates previously coated with PO-L. Neurons were generated from the NPs after differentiation for 4 weeks, amounting to ~6.5×10^4 cells per well in XF96 cell-culture microplates. Prior to the experiment, the original culture medium was replaced with Seahorse XF DMEM medium without phenol red supplemented with 2.5 mM L-glutamine,

0.5 mM sodium pyruvate and 17.5 mM glucose (all from Agilent) (supplemented to match the levels of these components in the DMEM/F-12 medium in which the neurons were cultured), and the cells were incubated for 1 h in a non-CO_2 incubator. Preparation of all the regents was done while the cells were in the incubation period and following the manufacturer's instructions. Basal levels of oxygen consumption rates (OCR) were measured on an XFe96 Extracellular Flux Analyzer (Agilent). Cells were stimulated with 2 μM oligomycin, 3 μM BAM15 and 1 μM rotenone/antimycin A (all from Sigma-Aldrich), as per the instructions of XF Cell Mito Stress Test Kit (Agilent). A range of mitochondrial respiratory parameters were calculated, such as basal respiration, maximal respiration and ATP production, as per the equations below. CyQUANT Direct Cell proliferation assay (Thermo Fisher Scientific) was used to normalise cell number as per manufacturer's instructions. Fluorescence was measured in a FLUOstar Omega Plate Reader (BMG Labtech). See the key resources table for further information of the reagents used for mitochondrial respiration measurement.

Basal respiration = (measurement before oligomycin stimulation) – (rate measurement after rotenone/antimycin A stimulation);

Maximal respiration = (maximum rate measurement after BAM15 stimulation) – (minimum rate measurement after rotenone/antimycin A stimulation);

ATP production = (basal respiration) – (minimum rate measurement after oligomycin stimulation).

6.22. MitoTracker staining and mitochondrial rod/branch length analysis

MitoTracker Red CMXRos (Invitrogen) (see key resources table) was used to label mitochondria as per manufacturer's protocol. Cells were incubated with 100 nM MitoTracker Red CMXRos for 45 min at 37 °C, after which the cells were either fixed and imaged for analysis or subjected to immunofluorescence with cell-specific markers. Mitochondrial rod/branch length analysis (after MitoTracker staining or Tom20 immunofluorescence) was done per cell in hESCs (~40 cells per sample and 5-50 fragments per cell were analysed) and per field of view in neurons (~4 images per sample and 200-4000 fragments per image were analysed) using the Analyze Skeleton plugin from the Mitochondrial Network Analysis (MiNA) toolset in ImageJ v1.41 (NIH) [225].

6.23. Mitochondrial and cytosolic fractionation

Mitochondrial and cytosolic fractions were prepared from cells using Mitochondria Isolation Kit (Thermo Fisher Scientific) (see key resources table), according to the manufacturer's instructions. 2×10^7 cells were pelleted for each sample from which cytoplasmic and mitochondrial fractions were separated by centrifugation at 13,000 g at 4 °C for 20 min, after which these subcellular fractions were immediately used for the measurements of NAD^+ and NADH.

6.24. Analysis of glucose concentration in the medium

Glucose concentrations in the medium of cells, and also in cell-free medium (blank), were measured using a Contour™ XT meter. Medium (10 µL) was applied to the test strip and a reading taken after a 5 s equilibration period. Data were normalised to the protein concentration of the samples (via Bio-Rad Protein Assay), and fold changes of different time-points (days 1, 2 and 3) were calculated relative to day 0. For cell-free medium, the concentration of glucose was shown at different time-points.

6.25. Analysis of amino acid concentrations in the medium by GC–MS

The medium of cells and also in cell-free medium (blank) were collected for analysis of amino acid concentrations. Medium samples were extracted using a modified Bligh–Dyer procedure [226] where equal volumes of MeOH/H_2O/$CHCl_3$ (Sigma-Aldrich; Honeywell Research Chemicals) were used to partition small molecule metabolites into a biphasic solution. The upper polar layer was removed and dried down for gas chromatography–mass spectrometry (GC–MS) analysis. Dried extracts were derivatised using a two-step protocol. Samples are first treated with 2 % methoxamine in pyridine (40 µL; 1 h at 60 °C) (Sigma-Aldrich), followed by addition of MTBSTFA (50 µL; 1 h at 60 °C) (Restek). Samples were centrifuged and the solution was transferred to glass vials for GC–MS analysis. GC–MS analysis was undertaken using an Agilent 7890B GC and 5977A MSD. 1 µL of sample was injected in splitless mode with helium carrier gas at a rate of 1 mL/min. Initial oven temperature was held at 100 °C for 1 min before ramping to 180 °C at a rate of 20 °C/min, followed by a ramp to 235 °C at a rate of 10 °C/min, and a final ramp to 320 °C at a rate of 100 °C/min with a 3 min hold. Compound detection was carried out in scan mode. Total ion count of each metabolite was normalised to the internal standard D_6-Glutaric acid (CDN Isotopes). Data were normalised to the protein concentration of the

samples (via Bio-Rad Protein Assay), and fold changes of different time-points (days 1, 2 and 3) were calculated relative to day 0. For cell-free medium, the concentrations of metabolites were shown at different time-points. See the key resources table for further information of the reagents used for analysis of amino acid concentrations.

6.26. [U-$^{13}C_6$]-Glucose tracer labelling and analysis of metabolites by GC–MS

After 3 weeks of neuronal differentiation as described in previous section, cells were cultured in a customized DMEM/F-12 neuronal medium lacking D-Glucose and Phenol Red (Cell Culture Technologies), supplemented with [U-$^{13}C_6$]-Glucose tracer (Cambridge Isotope Laboratories), for 24 h. Cell and medium samples of hESC-derived neurons were extracted using a modified Bligh–Dyer procedure ,[73] and samples were prepared for GC–MS analysis, as described above. Samples were analysed using an Agilent 8890/5977B GC–MS. 1 µL of sample was injected in splitless mode with helium carrier gas at a rate of 1 mL/min. Initial oven temperature was held at 100 °C for 1 min before ramping to 170 °C at a rate of 10 °C/min, followed by a ramp to 220 °C at a rate of 3 °C/min and a final ramp to 300 °C at a rate of 10 °C/min with a 5 min hold. Compound detection was carried out in scan mode. Total ion counts of each metabolite were normalised to the internal standard D6-Glutaric acid. The ^{13}C tracer data was corrected for natural abundance using in-house MATLAB scripts. Data were normalised to the protein concentration of the samples via Bio-Rad Protein Assay (Bio-Rad). See the key resources table for reagents used for analysis of [U-$^{13}C_6$]-Glucose tracer labelling.

6.27. LC–MS-based metabolomics

Liquid chromatography–mass spectrometry (LC–MS)-based metabolomics [227] was performed in hESC-derived neurons after 3 weeks of neuronal differentiation. Briefly, cells were washed with cold PBS and lysed on ice at 2×10^6 cells/mL concentration in Metabolite Extraction Buffer comprising of 30 % acetonitrile (Sigma-Aldrich), 50 % methanol (Fisher Scientific) and 20 % Milli-Q water. Samples were vortexed for 45 s, centrifuged at 13000 rpm for 5 min at 4 °C, and the supernatants subjected to LC–MS using an Accela 600 LC system and Exactive mass spectrometer (Thermo Scientific). For separation of metabolites, a Sequant ZIC-pHILIC column (4.6 mm × 150 mm, 5 µm; Merck) was used with the mobile phase mixed by A = 20 mM ammonium carbonate in water and B = acetonitrile. A gradient program starting at 20 % of A and linearly increasing to 80 % at 30

min was used, followed by washing (92 % of A for 5 min) and re-equilibration (20 % of A for 10 min), and the total run time of the method was 45 min. The LC stream was desolvated and ionised in the HESI probe. The Exactive Mass Spectrometer was operated in full scan mode over a mass range of 70–1200 m/z at a resolution of 50000 with polarity switching. The LC–MS raw data was converted into mzML files via ProteoWizard and imported to MZMine 2.10 for peak extraction and sample alignment [228, 229]. A house-made database integrating KEGG, HMDB and LIPID MAPS was used for the assignment of the LC–MS signals by searching the accurate mass, and the metabolites were confirmed by running their commercial standards. Peak areas of different metabolites were normalised to the total ionic count (TIC) minus blank, and were used for comparative quantification. See the key resources table for further information on the reagents and tools used for LC–MS-based metabolomics.

6.28. Metabolomics data analysis

Multivariate statistical analysis on MS-based metabolomics was performed using MetaboAnalyst 4.0 [230].Each of the metabolite peaks was first normalized by auto-scaling (mean-centred and divided by SD of each variable) and then principal component analysis (PCA) was applied. Metabolite fold change was calculated relative to *ATG5*$^{+/+}$ (wild-type) cells, and then converted to Log_2 values. Each metabolite was plotted on a heatmap, and all metabolites were also plotted on a heatmap with hierarchical clustering. Furthermore, a univariate statistical test coupled with fold change of each metabolite or each amino acid were plotted on volcano plots. The significance cut-off was set to an adjusted *P* value of 0.05 ($-Log_{10}$(*P*-adjusted)>1.3) and a fold-change as indicated. Statistical significance was determined using the Student's *t*-test with *P* value corrected with Benjamini and Hochberg (BH) false discovery rate (FDR) method.

6.29. High Content drug screening of FDA-approved and investigational drugs

mCherry-EGFP-LC3 neuronal precursors (NPs) were cultured to reach 80-100% confluency. Cells were dissociated using 0.05 % Trypsin-EDTA and seeded into 96-well, clear bottom black plates pre-coated with PO and LAM in the density of 2 x 10^4, then allowed to settle for 24 h in a 37 ºC, 5 % CO_2 humidified incubator. The library of autophagy-inducing FDA-approved or investigational drugs (**Table 8**) was prepared as 100 mM stock solutions (in DMSO). Using a serial dilution, four concentrations for each

experiment (0.1, 1, 10 and 100 μM) were prepared. Autophagy reporter NPs were treated for 24 h. Cells were fixed with 4 % paraformaldehyde, stained with DAPI at room temperature in the dark or covered with foil, and then immersed in PBS containing 0.02 % sodium azide. The analysis was carried out using CX5 CellInsight High-Content Screening (HCS) microscope and HCS Studio Cell Analysis software (Thermo Scientific). For each treatment condition, fluorescent images were collected for >1000 cells, and the $mCherry^+$ signal/cell was quantified. The quantification approach was automated using a Fiji groovy script [206]. To segment and identify individual nuclei from the DAPI channel we used a convolutional neural network-based approach called StarDist [arXiv:1806.03535]. The "fluorescent nuclei" pre-trained model provided in the Fiji StarDist plugin was used. Objects returned by StarDist that were smaller than 250 pixels were discarded. The number of nuclei gave the estimate for the number of cells in the field of view. To assist with segmentation of the cellular boundaries (cytoplasm) and the localization spots, the ilastik [207] pixel classifiers were trained on each spot channel to split the image into three classes: extra-cellular background, cellular background, and spot. Ilastik trains a random forest classifier on the user provided annotations to predict probabilities for the three classes. All the available default features were used to train the classifiers. The classifiers were run in batch continously and then the "simple segmentation" results were loaded into the Fiji script as needed. The ilastik class segmentations for the cellular background, and spot from both spot channels were combined to give a total cell segmentation. Cell segmentations were refined by filling in holes smaller than 1000 pixels and discarding objects smaller than 2500 pixels. To get an estimate for the number of spots, two complementary approaches were used: (1) The number of objects (connected components) in the ilastik simple segmentation for the spot class was counted excluding objects smaller than 5 pixels. (2) The TrackMate plugin [208] was used to perform spot detection on the raw data with median filtering, a Laplacian of Gaussian detector and a quality threshold. In both classes, spots outside the cellular segmentation were excluded from the final spot counts. The data was expressed as a percentage of the control (DMSO treated) condition fixed at 100 %. Quantification was performed on >1000 cells per sample.

Quantification and statistical analysis

Quantification of data are described under various sections where applicable. Graphical data are shown from n = 3 or more biological replicates from two or three independent experiments, as indicated in the figure legends. Graphical data are depicted by column graph scatter dot plot (mean ± s.e.m.) or violin plot (lines at median and quartiles) using GraphPad Prism v8.3.1 software (GraphPad). Statistical significance (P value) on all graphical data was determined by unpaired two-tailed Student's t-test with Welch correction or by one-way ANOVA followed by multiple comparisons with two-stage linear step-up procedure of Benjamini, Krieger and Yekutieli using GraphPad Prism v8.3.1 software (GraphPad). For metabolomics data analysis, statistical significance was determined by Student's t-test using Benjamini and Hochberg FDR method. ***P<0.001; **P<0.01; *P<0.05; ns (non-significant).

KEY RESOURCES TABLE

REAGENT or RESOURCE	SOURCE	IDENTIFIER
Antibodies		
Acetylated lysine	Cell Signaling Technology	Cat# 9441
Actin	Sigma-Aldrich	Cat# MABT1333
ATG5	Nano Tools	Cat# 0262-100/ATG5-7C6
53BP1	Abcam	Cat# ab36823
LC3B	Novus Biologicals	Cat# NB100-2220
LC3B	NanoTools	Cat# 0231-100/LC3-5F10
Cleaved caspase-3$^{(Asp175)}$	Cell Signaling Technology	Cat# 9661
GAPDH	Sigma-Aldrich	Cat# G8795
GFP	Clontech	Cat# 632375
Goat anti-mouse IgG (H+L), Alexa Fluor 488	Invitrogen	Cat# A-11001
Goat anti-mouse IgG (H+L), Alexa Fluor 594	Invitrogen	Cat# A-11005
Goat anti-rabbit IgG (H+L), Alexa Fluor 488	Invitrogen	Cat# A-11008
Goat anti-rabbit IgG (H+L), Alexa Fluor 594	Invitrogen	Cat# A-11012
Donkey anti-goat IgG (H+L), Alexa Fluor 488	Invitrogen	Cat# A-11055
Goat anti-mouse IgG, H&L chain specific peroxidase conjugate	Calbiochem	Cat# 401253
Goat anti-rabbit IgG, H&L chain specific peroxidase conjugate	Calbiochem	Cat# 401393
Ki-67	Cell Signaling Technology	Cat# 9449
MAP2	Invitrogen	Cat# PA5-17646
NANOG	R&D Systems	Cat# SC009
NESTIN	BioLegend	Cat# 656802
OCT-3/4	R&D Systems	Cat# SC009
p62	BD Biosciences	Cat# 610832
p70 S6 kinase	Cell Signaling Technology	Cat# 9202
PARP1	Santa Cruz	Cat# sc-8007
PARP2	Santa Cruz	Cat# sc-393310
PAX6	BioLegend	Cat# 901301
Phospho-Histone H2A.X$^{(Ser139)}$	Millipore	Cat# 05-636
Phospho-p70 S6 kinase$^{(Thr389)}$	Cell Signaling Technology	Cat# 9206
Phospho-S6 ribosomal protein $^{(Ser235/236)}$	Cell Signaling Technology	Cat# 2211
Poly(ADP-ribose)	Enzo Life Sciences	Cat# ALX-804-220-R100
Rabbit anti-goat IgG, H&L chain specific peroxidase conjugate	Calbiochem	Cat# 401515
S6 ribosomal protein	Cell Signaling Technology	Cat# 2217
SIRT1	Abcam	Cat# ab7343
SIRT2	Proteintech	Cat# 19655-1-AP
SOX2	R&D Systems	Cat# AF2018
SOX2	R&D Systems	Cat# SC009
SSEA4	R&D Systems	Cat# SC009
Tom20	Santa Cruz Biotech.	Cat# sc-17764
TRA-1-60	R&D Systems	Cat# MAB4770
Tubulin	Sigma-Aldrich	Cat# T6793
TUJ1 (TUBB3)	BioLegend	Cat# 801201
Chemicals, peptides and recombinant proteins		
Antimycin A	Sigma-Aldrich	Cat# A8674
Amiodarone	Sigma-Aldrich	Cat# A8423
Bafilomycin A1	Sigma-Aldrich	Cat# 196000
Carbamazepine	Sigma-Aldrich	Cat# C4024
Chlorpromazine	Sigma-Aldrich	Cat# C8138

Clemastine	APExBIO	Cat# B1558
Clonidine	Sigma-Aldrich	Cat# C7897
EGF	Gibco	Cat# PHG0313
bFGF	Invitrogen	Cat# RP8627
Fluspirilene	Sigma-Aldrich	Cat# F100
β-mercaptoethanol	Sigma-Aldrich	Cat# M3148
B27 Supplement	Gibco	Cat# 12587-010
Carbonyl cyanide-p-trifluoromethoxyphenylhydrazone (FCCP)	Sigma-Aldrich	Cat# C2920
Cholesterol	Sigma-Aldrich	Cat# C8667
Collagenase type IV	Gibco	Cat# 17104-019
CM-H_2DCFDA	Invitrogen	Cat# C6827
Customized DMEM/F-12 without D-Glucose and Phenol Red	Cell Culture Technologies	Cat# 12161503
Dihydronicotinamide riboside (NRH)	Provide by Prof. Marie Migaud	N/A
1,2-dimyristoyl-sn-glycero-3-phosphoethanolamine-N-[methoxy(polyethylene glycol)-2000]	Avanti Polar Lipids	Cat# 880150
1,2-dioleoyl-sn-glycero-3-phosphoethanolamine	Avanti Polar Lipids	Cat# 870296
DMEM	Gibco	Cat# 41966-029
DMEM/F12	Gibco	Cat# 11320-074
EDTA	Invitrogen	Cat# 15575-038
FBS	Gibco	Cat# SH30071.03
Felodipine	Cayman Chemical	Cat# CAY17535
FK866	Sigma-Aldrich	Cat# F8557
Flubendazole	Sigma-Aldrich	Cat# SML2510
Fluphenazine	Cayman Chemical	Cat# CAY23555
Geltrex	Gibco	Cat# A1413302
GlutaMAX	Gibco	Cat# 35050061
HPLC Chloroform	Honeywell Research Chemicals	Cat# 15644530
HPLC Methanol	Sigma-Aldrich	Cat# 34860
HPLC Water	Sigma-Aldrich	Cat# 270733
KnockOut Serum Replacement	Gibco	Cat# 10828-028
Laminin	Sigma-Aldrich	Cat# L2020
L-Alanine	Sigma-Aldrich	Cat# A26802
L-Arginine	Sigma-Aldrich	Cat# A5006
L-Glutamic acid	Sigma-Aldrich	Cat# G5667
L-glutamine	Gibco	Cat# 25030-024
L-Glycine	Sigma-Aldrich	Cat# G7126
L-Histidine	Sigma-Aldrich	Cat# H8000
L-Leucine	Sigma-Aldrich	Cat# L8000
L-Lysine	Sigma-Aldrich	Cat# L5501
L-Methionine	Sigma-Aldrich	Cat# M5308
Loperamide	Sigma-Aldrich	Cat# L4762
L-Phenylalanine	Sigma-Aldrich	Cat# W358512
L-Proline	Sigma-Aldrich	Cat# P0380
L-Serine	Sigma-Aldrich	Cat# S4500
L-Tryptophan	Sigma-Aldrich	Cat# T0254
Metergoline	Cayman Chemical	Cat# CAY21336
Metformin	Sigma-Aldrich	Cat# 317240
Methoxyamine hydrochloride	Sigma-Aldrich	Cat# 226904
Minoxidil	Sigma-Aldrich	Cat# M4145
Mitomycin C	Sigma-Aldrich	Cat# M4287
MitoTracker Red CMXRos	Invitrogen	Cat# M7512

MTBSTFA	Restek	Cat# 35610
Nicotinamide (NAM)	Sigma-Aldrich	Cat# N3376
Nicotinamide mononucleotide (NMN)	Provided by NMN Bio	Cat# NMN01-16676
Nicotinamide riboside (NR)	Provided by ChromaDex	N/A
Nimodipine	Sigma-Aldrich	Cat# N149
Non-essential amino acids	Gibco	Cat# 11140-035
Noscapine	Cayman Chemical	Cat# CAY17255
N2 supplement	Gibco	Cat# 17502-048
Olaparib	Cambridge Biosciences	Cat# CAY10621
Oligomycin	Sigma-Aldrich	Cat# 495455
Penicillin/streptomycin	Gibco	Cat# 15070063
Pentanedioic-d_6 Acid (D_6-Glutaric acid)	CDN Isotopes	Cat# D-5227
Perhexiline	Sigma-Aldrich	Cat# SML0120
Perifosine	APExBIO	Cat# A8309
Pimozide	Sigma-Aldrich	Cat# P1793
Poly-L-Ornithine	Sigma-Aldrich	Cat# P4957
ProLong Gold Antifade Mountant with DAPI	Invitrogen	Cat# P36931
Protein A agarose	Invitrogen	Cat# 15918-014
Puromycin	Gibco	Cat# A1113803
Rapamycin	Sigma-Aldrich	Cat# R0395
Recombinant Human Noggin	Peprotech	Cat# 120-10C
Rilmenidine	Sigma-Aldrich	Cat# R134
ROCK inhibitor Y-27632	Stemgent	Cat# 04-0012-02
Rotenone	Sigma-Aldrich	Cat# R8875
SB431542	Stemgent	Cat# 04-0010-10
Simvastatin	Sigma-Aldrich	Cat# S6196
Sirtinol	Cambridge Biosciences	Cat# CAY10523
StemFlex Basal Medium	Gibco	Cat# A33494-01
StemFlex 10X Supplement	Gibco	Cat# A33492-01
StemPro Accutase	Gibco	Cat# A111050
Tetramethylrhodamine, Ethyl Ester, Perchlorate (TMRE)	Invitrogen	Cat# T669
Thioridazine	Cayman Chemical	Cat# CAY14400
Trehalose	Sigma-Aldrich	Cat# T9531
Trifluoperazine	Sigma-Aldrich	Cat# T8516
[U-$13C^6$]-Glucose tracer	Cambridge Isotope Laboratories	Cat# CLM-1396
Valproic acid sodium	Sigma-Aldrich	Cat# P4543
Verapamil	Sigma-Aldrich	Cat# V4629
Critical commercial assays		
ApoSENSOR ADP/ATP Ratio Bioluminescent Assay Kit	BioVision	Cat# K255-200
Bio-Rad Protein Assay Kit II	Bio-Rad	Cat# 5000002
CytoTox-Glo Cytotoxicity Assay Kit	Promega	Cat# G9290
CyQUANT Cell Proliferation Assay	Thermo Fisher Scientific	Cat# C7026
Click-iT Plus TUNEL Assay Kit	Invitrogen	Cat# C10617
HT Universal Colorimetric PARP Assay Kit	R&D Systems	Cat# 4677-096-K
Mitochondria Isolation Kit for Cultured Cells	ThermoFisher	Cat# 89874
NAD/NADH Quantitation Colorimetric Kit	BioVision	Cat# K337-100
PROTEOSTAT Aggresome Detection Kit	Enzo	Cat# ENZ-51035-K100
Quant-iT RiboGreen RNA Assay	Invitrogen	Cat# R11490
RNase-free DNase Set	Qiagen	Cat# 79254
Seahorse XF Cell Mito Stress Test Kit	Agilent	Cat# 103015-100
SIRT1 Activity Assay Kit	Abcam	Cat# ab156065
SIRT2 Activity Assay Kit	Abcam	Cat# ab156066

Deposited data		
LC–MS metabolomics data	Sun et al. [134]	MassIVE accession number MSV000091468; Table S1
Experimental models: Cell lines		
ATG5$^{+/+}$ (WIBR3) hESCs	Lengner et al. [62]	N/A
ATG5$^{+/-}$ (clone #1, #2) hESCs	Sun et al. [134]	N/A
ATG5$^{-/-}$ (clones #1, #3, #4, #5, #6) hESCs	Sun et al. [134]	N/A
Control (CT1,CT2) NSCs	Pourtoy-Brasselet et al.[193]	N/A
Control human neuroblastoma	Gharanei et al.[231]	N/A
Human fibroblasts (line C1)	Hu et al. [63]	N/A
Inactivated mouse embryonic fibroblasts	Lengner et al. [62]	N/A
WFS1^{KD} human neuroblastoma	Gharanei et al. [231]	N/A
WS patient-derived (WS1, WS2, WS5) NSCs	Shang et al [194]; Pourtoy-Brasselet et al. [193]	N/A
Oligonucleotides		
Primers for qPCR	Sun et al.	Table 6
TALENs targeting *ATG5*	Sun et al.	N/A
Recombinant DNA		
ATG5 targeting donor vectors	Sun et al.	N/A
Software and algorithms		
GraphPad Prism v8.3.1	GraphPad Software	https://www.graphpad.com/; RRID:SCR_002798
ImageJ v1.41	NIH	https://imagej.net/ij/index.html; RRID:SCR_003070
Magellan F50	Tecan	https://lifesciences.tecan.com/software-magellan; N/A
MetaboAnalyst 4.0	Xia and Wishart	https://www.metaboanalyst.ca/; RRID:SCR_015539
MZMine 2.10	Pluskal et al.	http://mzmine.github.io/; RRID:SCR_012040
ProteoWizard	Chambers et al.	https://proteowizard.sourceforge.io/; RRID:SCR_012056

Table 1

Metabolite	*ATG5*$^{+/+}$ (1)	*ATG5*$^{+/+}$ (2)	*ATG5*$^{+/+}$ (3)	*ATG5*$^{-/-}$ (1)	*ATG5*$^{-/-}$ (2)	*ATG5*$^{-/-}$ (3)
ADP	58085.28	53519.21	43983.58	17663.96	23900.84	27940.24
AMP	28273.42	17843.57	6765.77	6445.73	7413.84	10647.56
ATP	3428478.13	3289189.48	3209559.79	245607.45	332642.42	347597.22
CDP	25.59	19.13	22.36	424.90	613.43	879.78
CTP	58982.68	54147.52	55556.50	5090.82	6892.72	6605.41
GDP	4835.01	4928.96	5165.43	2306.03	2830.41	2745.14
GTP	319826.41	285553.49	298991.28	18656.23	21674.39	19098.62
UDP	33186.72	34733.48	27961.77	15394.52	21421.97	25534.32
UMP	2461.39	2882.78	3251.70	1245.16	1350.40	1398.35
UTP	612818.43	609720.00	629478.55	28831.42	30177.97	38826.13
NAD+	49394.90	55118.22	70233.54	6544.13	6040.31	5496.19
NADH	32412.14	42681.72	35155.08	20988.96	20637.14	21493.08
L-Alanine	3100490.08	2880667.50	2775813.00	1541836.26	1481109.21	1440196.69
L-Arginine	11527166.89	10998216.66	10895915.94	9418988.00	8407248.63	7339292.12
L-Asparagine	425616.91	431162.86	452888.54	608213.61	612042.81	537539.24
L-Aspartate	220088.73	217026.89	227206.78	382263.35	377059.87	347033.10
Cysteine	3838.17	3270.52	2975.83	8374.96	8472.93	7523.92
L-Glutamine	62306421.59	60872170.14	55690881.93	86502757.19	84476514.28	79490723.29
L-Glutamate	2459056.01	2562537.69	2725849.76	2385897.67	2292096.28	2164015.86
Glycine	1752900.62	1799726.42	1814292.28	551186.75	507501.71	484658.97
L-Histidine	9691808.45	8767121.81	9713134.80	6041431.49	6105084.29	4361708.09
L-Leucine/L-Isoleucine	25921462.76	24092864.70	24123739.83	17962655.95	16592773.03	18818358.47
L-Lysine	3542606.42	3333261.45	3240455.00	2236797.63	2151019.88	1264886.53
L-Methionine	5025330.60	4636089.10	4588520.34	2385737.54	2271851.81	2262046.25
L-Phenylalanine	11518620.72	10531212.94	10167417.34	4671933.20	4423946.59	4322547.87
L-Proline	36186482.64	34660237.57	35624201.09	15223904.62	15223444.46	14916137.65
L-Serine	2019446.84	1944390.97	1934856.43	1473570.94	1440517.17	1364185.50
L-Threonine	1701399.90	1562969.08	1607673.40	4053234.11	3890278.17	3652833.26
L-Tryptophan	1701352.23	1516899.43	1503291.10	627124.94	596703.51	574044.81
L-Tyrosine	2214161.68	2510905.53	3916872.07	2196007.63	2114282.19	1964937.24
L-Valine	7995826.73	7715762.76	8776407.97	7743401.06	6139773.64	5713594.39
D-Glucose	278949.88	294918.42	309396.07	224137.95	250316.07	239110.59
Glucose 6-phosphate	333777.82	353920.05	387258.51	27699.91	33589.84	39450.78
Fructose 1,6-bisphosphate	350677.04	331882.28	257585.40	25803.77	27223.21	26688.06
Dihydroxyacetone phosphate	765490.96	850772.45	797850.68	215107.27	216459.61	193603.81
Glyceraldehyde 3-phosphate	766825.16	849816.99	798027.45	215107.27	216459.61	193603.81
2-Phospho-D-glycerate/3-Phospho-D-glycerate	359349.03	379100.52	242913.06	91039.74	113973.46	123671.30
Phosphoenolpyruvate	18908.89	30257.04	22807.71	4037.91	4567.38	4479.33
Pyruvate	265300.90	268700.81	256698.03	178930.97	187916.01	184971.39
L-Lactate	9271147.81	9439112.32	8843156.85	1780381.17	1774529.98	1748598.95
Acetyl-CoA	1276.48	1008.05	1888.34	236.54	331.54	559.22
Citrate/Isocitrate	3914337.64	3317129.53	3474171.23	762242.33	780557.27	797219.62
cis-Aconitate	165507.71	142533.44	156030.44	24531.30	25546.67	25701.32
2-Oxoglutarate	258855.87	202009.85	231446.89	9444.33	10319.87	9947.10
Succinate	86418.35	114995.92	126627.86	93904.62	84147.80	85619.11
Fumarate	391232.92	347548.48	348057.63	79311.85	85562.06	84479.37
(S)-Malate	3365494.65	3069264.52	3004241.20	832188.30	884937.43	903016.73
Oxaloacetate	1609.45	2351.10	2611.17	9319.54	9676.48	9754.61
Ribulose-5-phosphate/D-Ribose-5-phosphate	24377.30	26847.24	36440.48	5742.50	6920.88	6742.48
D-Sedoheptulose-7-phosphate	4220.57	5201.96	6057.23	1684.65	2202.55	2396.53
CoA	1108.35	1230.38	1486.36	44.46	120.47	125.48
D-Galactose	333681.24	353827.15	409333.05	314244.11	311384.08	297465.34

Table 1. LC–MS based metabolomic data.
LC–MS based metabolomic data in *ATG5*$^{+/+}$ (wild-type; *n* = 3) and *ATG5*$^{-/-}$_5 (autophagy-deficient; *n* = 3) human embryonic stem cells (hESCs)-derived neurons.

Table 2

hiPSC line	hiPSC ID	Gender	Genotype	Disease affected	Mutations in *WFS1* gene
CT1	iPSC 1869	Male	Healthy control	No	wild-type
CT2	iPSC/i90c16	Female	Healthy control	No	wild-type
WS1	iPSC WS1	Male	WS patient	Yes	c.1230-1233delCTCT [V412fs*440]; c.2171C>T [p.P724L]
WS2	iPSC WS2	Female	WS patient	Yes	c.1230-1233delCTCT [p.V412fs*440]
WS5	iPSC/WS5c13	female	WS patient	Yes	c.1060-1062delTTC [p.F354del]; c.1676C>A [p.A559D]

Table 2. List of control (CT) and Wolfram Syndrome (WS) patient-derived hiPSC lines from which neural precursors and neurons were derived.

Table 3

Compound name	Working conc.	Cell type used	Source
CP2	1 μM	hESC-derived neurons	From E. Trushina
FK866	10 nM	hESC-derived neurons	Sigma-Aldrich
L-Tryptophan	1 mM	hESC-derived neurons	Sigma-Aldrich
Nicotinamide (NAM)	1 mM	hESCs, hESC-derived NPs and neurons	Sigma-Aldrich
Nicotinamide mononucleotide (NMN)	1 mM	hESC-derived neurons	NMN Bio Ltd.
Nicotinamide riboside (NR)	1 mM	hESC-derived neurons	ChromaDex
Dihydronicotinamide riboside (NRH)	100 μM	hiPSC-derived neurons	From Prof. Marie Migaud
Olaparib	10 μM	hESC-derived neurons	Cambridge Biosciences
Sirtinol	20 μM	hESC-derived neurons	Cambridge Biosciences

Table 3. Compounds used for modulating NAD levels.
Compounds used for modulating NAD levels in cell culture experiments in human embryonic stem cells (hESCs) and hESC-derived neural precursors (NPs) and neurons, along with their working concentration, cell type used and the source (company), are indicated. See Methods for treatment duration and the key resources table for further information of the compounds.

Table 4

Antigen	Source	Dilution	Cell type used
Primary antibodies			
Acetylated lysine	Cell Signaling Technology	1:1000	hESCs, hESC-derived NPs and neurons
Actin	Sigma-Aldrich	1:4000	hESCs, hESC-derived NPs and neurons
ATG5	NanoTools	1:400	hESCs, hESC-derived NPs and neurons
Cleaved caspase-3$^{(Asp175)}$	Cell Signaling Technology	1:200	hESCs, hESC-derived NPs and neurons
GAPDH	Sigma-Aldrich	1:5000	hESCs, hESC-derived NPs and neurons
GFP	Clontech	1:5000	hESCs, hESC-derived neurons
LC3B	Novus Biologicals	1:2000	hESCs, hESC-derived NPs and neurons
MAP2	Invitrogen	1:5000	hESC-derived neurons
NESTIN	BioLegend	1:2000	hESC-derived NPs
p62	BD Biosciences	1:1000	hESCs, hESC-derived NPs and neurons
p70 S6 kinase	Cell Signaling Technology	1:1000	hESCs
PAX6	BioLegend	1:2000	hESC-derived NPs
Phospho-p70 S6 kinase$^{(Thr389)}$	Cell Signaling Technology	1:1000	hESCs
Phospho-S6 ribosomal protein $^{(Ser235/236)}$	Cell Signaling Technology	1:4000	hESCs
Poly(ADP-ribose)	Enzo Life Sciences	1:1000	hESCs, hESC-derived NPs and neurons
S6 ribosomal protein	Cell Signaling Technology	1:4000	hESCs
SOX2	R&D Systems	1:500	hESC-derived NPs
Tom20	Santa Cruz Biotechnology	1:5000	hESC-derived neurons
Tubulin	Sigma-Aldrich	1:5000	hESCs, hESC-derived NPs and neurons
TUJ1 (TUBB3)	BioLegend	1:5000	hESC-derived neurons
Secondary antibodies			
Goat anti-mouse IgG, H&L chain specific peroxidase conjugate	Merck	1:10000	(as per the primary antibodies used)
Goat anti-rabbit IgG, H&L chain specific peroxidase conjugate	Merck	1:10000	(as per the primary antibodies used)
Rabbit anti-goat IgG, H&L chain specific peroxidase conjugate	Merck	1:10000	(as per the primary antibodies used)

Table 4. List of primary and secondary antibodies for immunoblotting analysis.
The primary and secondary antibodies for immunoblotting analysis in human embryonic stem cells (hESCs) and hESC-derived neural precursors (NPs) and neurons. See the key resources table for further information of the antibodies used for immunoblotting analysis.

Table 5

Antigen	Source	Dilution	Cell type used
Primary antibodies			
Acetylated lysine	Cell Signaling Technology	1:400	hESC-derived neurons
53BP1	Abcam	1:2000	hESC-derived neurons
Ki-67	Cell Signaling Technology	1:400	hESCs
LC3B	NanoTools	1:200	hESCs, hESC-derived NPs and neurons
MAP2	Invitrogen	1:200	hESC-derived neurons
NANOG	R&D Systems	1:100	hESCs
NESTIN	BioLegend	1:100	hESC-derived NPs
OCT-3/4	R&D Systems	1:100	hESCs
PAX6	BioLegend	1:100	hESC-derived NPs
Phospho-Histone H2A.X$^{(Ser139)}$	Millipore	1:2000	hESC-derived neurons
Poly(ADP-ribose)	Enzo Life Sciences	1:100	hESC-derived neurons
SOX2	R&D Systems	1:100	hESCs
SSEA4	R&D Systems	1:100	hESCs
Tom20	Santa Cruz Biotechnology	1:100	hESCs, hESC-derived neurons
TRA-1-60	R&D Systems	1:100	hESCs
TUJ1 (TUBB3)	BioLegend	1:200	hESC-derived neurons
Secondary antibodies			
Goat anti-mouse IgG (H+L), Alexa Fluor 488	Invitrogen	1:1000	(as per the primary antibodies used)
Goat anti-mouse IgG (H+L), Alexa Fluor 594	Invitrogen	1:1000	(as per the primary antibodies used)
Goat anti-rabbit IgG (H+L), Alexa Fluor 488	Invitrogen	1:1000	(as per the primary antibodies used)
Goat anti-rabbit IgG (H+L), Alexa Fluor 594	Invitrogen	1:1000	(as per the primary antibodies used)
Donkey anti-goat IgG (H+L), Alexa Fluor 488	Invitrogen	1:1000	(as per the primary antibodies used)

Table 5. List of primary and secondary antibodies for immunofluorescence analysis. The primary and secondary antibodies used for immunofluorescence analysis in human embryonic stem cells (hESCs) and hESC-derived neural precursors (NPs) and neurons. See the key resources table for further information of the antibodies used for immunofluorescence analysis.

Table 6

Gene	Species	Primer name	Primer sequence	Cell type used
NANOG	Human	*NANOG* Forward	TGTGTACTCAATGATAGATT	hESCs
		NANOG Reverse	GTCTTCACCTGTTTGTAG	
PAX6	Human	*PAX6* Forward	ACACACATGAACAGTCAGCCA	hESC-derived NPs
		PAX6 Reverse	TCAGGTTCACTTCCGGGAAC	
POU5F1	Human	*POU5F1* Forward	TCTATTTGGGAAGGTATTC	hESCs
		POU5F1 Reverse	TTGCATATCTCCTGAAGA	
MAP2	Human	*MAP2* Forward	AGG CCC AAG CTA AAG TTG GT	hESC-derived neurons
		MAP2 Reverse	ATG GTC CAC ACG GGC TTT AG	
NESTIN	Human	*NESTIN* Forward	GTGGCTCCAAGACTTCCCTC	hESC-derived NPs
		NESTIN Reverse	GAAGTTGGGCTCAGGACTGG	
NeuN	Human	*NeuN* Forward	TAC AGC GAC AGT TAC GGC AG	hESC-derived neurons
		NeuN Reverse	TTC CAA TGC TGT AGG TCG CC	
SOX2	Human	*SOX2* Forward	CGGACAGCGAACTGGAGG	hESCs
		SOX2 Reverse	CTGTTTCTTACTCTCCTCTTTTGC	
GAPDH	Human	*GAPDH* Forward	TCGACAGTCAGCCGCATCTTCTTT	hESCs, hESC-derived NPs and neurons
		GAPDH Reverse	ACCAAATCCGTTGACCTT	

Table 6. Primers used for qPCR.
The primers and their sequence used for analyzing the gene expression of cell-specific markers by qPCR in human embryonic stem cells (hESCs) and hESC-derived neural precursors (NPs) and neurons. See the key resources table for further information of the primers used for qPCR.

Table 7

Antigen	Source	Concentration	Cell type used
PARP1	Santa Cruz Biotechnology	6 µg / 50 µL of bead slurry	hESC-derived neurons
PARP2	Santa Cruz Biotechnology	6 µg / 50 µL of bead slurry	hESC-derived neurons
SIRT1	Abcam	6 µg / 50 µL of bead slurry	hESC-derived neurons
SIRT2	Proteintech	6 µg / 50 µL of bead slurry	hESC-derived neurons

Table 7. List of primary and secondary antibodies for immunoprecipitation.
The primary antibodies used for immunoprecipitation to measure the enzyme activity of PARP1, PARP2, SIRT1 and SIRT2 in human embryonic stem cells (hESCs)-derived neurons. See the key resources table for further information of the antibodies used for immunoprecipitation.

Table 8

Compound name	Working conc.	Cell type used	Source
Amiodarone	0.1,1,10,100 μM	hESC-derived NPs	Sigma-Aldrich
Bafilomycin A1	400nM	hESC-derived NPs	Sigma-Aldrich
Carbamazepine	0.1,1,10,100 μM	hESC-derived NPs	Sigma-Aldrich
Chlorpromazine	0.1,1,10,100 μM	hESC-derived NPs	Sigma-Aldrich
Clemastine	0.1,1,10,100 μM	hESC-derived NPs	APExBIO
Clonidine	0.1,1,10,100 μM	hESC-derived NPs	Sigma-Aldrich
Fluspirilene	0.1,1,10,100 μM	hESC-derived NPs	Sigma-Aldrich
Felodipine	0.1,1,10,100 μM	hESC-derived NPs	Cayman Chemical
Flubendazole	0.1,1,10,100 μM	hESC-derived NPs	Sigma-Aldrich
Fluphenazine	0.1,1,10,100 μM	hESC-derived NPs	Cayman Chemical
Loperamide	0.1,1,10,100 μM	hESC-derived NPs	Sigma-Aldrich
Metergoline	0.1,1,10,100 μM	hESC-derived NPs	Cayman Chemical
Metformin	0.1,1,10,100 μM	hESC-derived NPs	Sigma-Aldrich
Minoxidil	0.1,1,10,100 μM	hESC-derived NPs	Sigma-Aldrich
Nimodipine	0.1,1,10,100 μM	hESC-derived NPs	Sigma-Aldrich
Noscapine	0.1,1,10,100 μM	hESC-derived NPs	Cayman Chemical
Perhexiline	0.1,1,10,100 μM	hESC-derived NPs	Sigma-Aldrich
Perifosine	0.1,1,10,100 μM	hESC-derived NPs	APExBIO
Pimozide	0.1,1,10,100 μM	hESC-derived NPs	Sigma-Aldrich
Rapamycin	200nM	hESC-derived NPs	Sigma-Aldrich
Rilmenidine	0.1,1,10,100 μM	hESC-derived NPs	Sigma-Aldrich
Simvastatin	0.1,1,10,100 μM	hESC-derived NPs	Sigma-Aldrich
Thioridazine	0.1,1,10,100 μM	hESC-derived NPs	Cayman Chemical
Trifluoperazine	0.1,1,10,100 μM	hESC-derived NPs	Sigma-Aldrich
Valproic acid sodium	0.1,1,10,100 μM	hESC-derived NPs	Sigma-Aldrich
Verapamil	0.1,1,10,100 μM	hESC-derived NPs	Sigma-Aldrich

Table 8. FDA-approved and investigational compounds used for high-content screening in mCherry-EGFP-LC3 autophagy reporter hESC-derived NPs.
Compounds used in the high-content screening in mCherry-EGFP-LC3 hESC-derived neural precursors (NPs) of 24hrs treatment, along with their working concentration, cell type used and the source (company), are indicated. See Methods for treatment duration and the key resources table for further information of the compounds.

REFERENCES

1. Seranova, E., et al., *Human Induced Pluripotent Stem Cell Models of Neurodegenerative Disorders for Studying the Biomedical Implications of Autophagy.* J Mol Biol, 2020. **432**(8): p. 2754-2798.
2. Wilson, N., et al., *The autophagy-NAD axis in longevity and disease.* Trends Cell Biol, 2023. **33**(9): p. 788-802.
3. Tsukada, M. and Y. Ohsumi, *Isolation and characterization of autophagy-defective mutants of Saccharomyces cerevisiae.* FEBS Lett, 1993. **333**(1-2): p. 169-74.
4. Sarkar, S., *Regulation of autophagy by mTOR-dependent and mTOR-independent pathways: autophagy dysfunction in neurodegenerative diseases and therapeutic application of autophagy enhancers.* Biochem Soc Trans, 2013. **41**(5): p. 1103-30.
5. Ganley, I.G., et al., *ULK1.ATG13.FIP200 complex mediates mTOR signaling and is essential for autophagy.* J Biol Chem, 2009. **284**(18): p. 12297-305.
6. Mizushima, N., et al., *A protein conjugation system essential for autophagy.* Nature, 1998. **395**(6700): p. 395-8.
7. Mizushima, N., *The role of the Atg1/ULK1 complex in autophagy regulation.* Curr Opin Cell Biol, 2010. **22**(2): p. 132-9.
8. Zachari, M. and I.G. Ganley, *The mammalian ULK1 complex and autophagy initiation.* Essays Biochem, 2017. **61**(6): p. 585-596.
9. Russell, R.C., et al., *ULK1 induces autophagy by phosphorylating Beclin-1 and activating VPS34 lipid kinase.* Nat Cell Biol, 2013. **15**(7): p. 741-50.
10. Karanasios, E., et al., *Dynamic association of the ULK1 complex with omegasomes during autophagy induction.* J Cell Sci, 2013. **126**(Pt 22): p. 5224-38.
11. Kim, J., et al., *Differential regulation of distinct Vps34 complexes by AMPK in nutrient stress and autophagy.* Cell, 2013. **152**(1-2): p. 290-303.
12. Karanasios, E., et al., *Autophagy initiation by ULK complex assembly on ER tubulovesicular regions marked by ATG9 vesicles.* Nat Commun, 2016. **7**: p. 12420.
13. Hanada, T., et al., *The Atg12-Atg5 conjugate has a novel E3-like activity for protein lipidation in autophagy.* J Biol Chem, 2007. **282**(52): p. 37298-302.
14. Tanida, I., T. Ueno, and E. Kominami, *Human light chain 3/MAP1LC3B is cleaved at its carboxyl-terminal Met121 to expose Gly120 for lipidation and targeting to autophagosomal membranes.* J Biol Chem, 2004. **279**(46): p. 47704-10.
15. Nakatogawa, H., Y. Ichimura, and Y. Ohsumi, *Atg8, a ubiquitin-like protein required for autophagosome formation, mediates membrane tethering and hemifusion.* Cell, 2007. **130**(1): p. 165-78.
16. Kabeya, Y., et al., *LC3, a mammalian homologue of yeast Apg8p, is localized in autophagosome membranes after processing.* EMBO J, 2000. **19**(21): p. 5720-8.
17. Jahreiss, L., F.M. Menzies, and D.C. Rubinsztein, *The itinerary of autophagosomes: from peripheral formation to kiss-and-run fusion with lysosomes.* Traffic, 2008. **9**(4): p. 574-87.
18. Kimura, S., T. Noda, and T. Yoshimori, *Dynein-dependent movement of autophagosomes mediates efficient encounters with lysosomes.* Cell Struct Funct, 2008. **33**(1): p. 109-22.
19. Liang, C., et al., *Beclin1-binding UVRAG targets the class C Vps complex to coordinate autophagosome maturation and endocytic trafficking.* Nat Cell Biol, 2008. **10**(7): p. 776-87.
20. Matsunaga, K., et al., *Two Beclin 1-binding proteins, Atg14L and Rubicon, reciprocally regulate autophagy at different stages.* Nat Cell Biol, 2009. **11**(4): p. 385-96.

21. McEwan, D.G., et al., *PLEKHM1 regulates autophagosome-lysosome fusion through HOPS complex and LC3/GABARAP proteins.* Mol Cell, 2015. **57**(1): p. 39-54.
22. Wang, Z., et al., *The Vici Syndrome Protein EPG5 Is a Rab7 Effector that Determines the Fusion Specificity of Autophagosomes with Late Endosomes/Lysosomes.* Mol Cell, 2016. **63**(5): p. 781-95.
23. Itakura, E., C. Kishi-Itakura, and N. Mizushima, *The hairpin-type tail-anchored SNARE syntaxin 17 targets to autophagosomes for fusion with endosomes/lysosomes.* Cell, 2012. **151**(6): p. 1256-69.
24. Seglen, P.O., P.B. Gordon, and I. Holen, *Non-selective autophagy.* Semin Cell Biol, 1990. **1**(6): p. 441-8.
25. Feng, Y., et al., *The machinery of macroautophagy.* Cell Res, 2014. **24**(1): p. 24-41.
26. Gatica, D., V. Lahiri, and D.J. Klionsky, *Cargo recognition and degradation by selective autophagy.* Nat Cell Biol, 2018. **20**(3): p. 233-242.
27. Stolz, A., A. Ernst, and I. Dikic, *Cargo recognition and trafficking in selective autophagy.* Nat Cell Biol, 2014. **16**(6): p. 495-501.
28. Kirkin, V., et al., *A role for ubiquitin in selective autophagy.* Mol Cell, 2009. **34**(3): p. 259-69.
29. Johansen, T. and T. Lamark, *Selective Autophagy: ATG8 Family Proteins, LIR Motifs and Cargo Receptors.* J Mol Biol, 2020. **432**(1): p. 80-103.
30. Bjorkoy, G., et al., *p62/SQSTM1 forms protein aggregates degraded by autophagy and has a protective effect on huntingtin-induced cell death.* J Cell Biol, 2005. **171**(4): p. 603-14.
31. Pankiv, S., et al., *p62/SQSTM1 binds directly to Atg8/LC3 to facilitate degradation of ubiquitinated protein aggregates by autophagy.* J Biol Chem, 2007. **282**(33): p. 24131-45.
32. Dikic, I. and Z. Elazar, *Mechanism and medical implications of mammalian autophagy.* Nat Rev Mol Cell Biol, 2018. **19**(6): p. 349-364.
33. Meijer, A.J., et al., *Regulation of autophagy by amino acids and MTOR-dependent signal transduction.* Amino Acids, 2015. **47**(10): p. 2037-63.
34. Sancak, Y., et al., *Ragulator-Rag complex targets mTORC1 to the lysosomal surface and is necessary for its activation by amino acids.* Cell, 2010. **141**(2): p. 290-303.
35. Saxton, R.A. and D.M. Sabatini, *mTOR Signaling in Growth, Metabolism, and Disease.* Cell, 2017. **168**(6): p. 960-976.
36. Nazio, F., et al., *mTOR inhibits autophagy by controlling ULK1 ubiquitylation, self-association and function through AMBRA1 and TRAF6.* Nat Cell Biol, 2013. **15**(4): p. 406-16.
37. Settembre, C., et al., *TFEB links autophagy to lysosomal biogenesis.* Science, 2011. **332**(6036): p. 1429-33.
38. Napolitano, G., et al., *mTOR-dependent phosphorylation controls TFEB nuclear export.* Nat Commun, 2018. **9**(1): p. 3312.
39. Di Malta, C., L. Cinque, and C. Settembre, *Transcriptional Regulation of Autophagy: Mechanisms and Diseases.* Front Cell Dev Biol, 2019. **7**: p. 114.
40. Meley, D., et al., *AMP-activated protein kinase and the regulation of autophagic proteolysis.* J Biol Chem, 2006. **281**(46): p. 34870-9.
41. Gwinn, D.M., et al., *AMPK phosphorylation of raptor mediates a metabolic checkpoint.* Mol Cell, 2008. **30**(2): p. 214-26.
42. Inoki, K., T. Zhu, and K.L. Guan, *TSC2 mediates cellular energy response to control cell growth and survival.* Cell, 2003. **115**(5): p. 577-90.
43. Kim, J., et al., *AMPK and mTOR regulate autophagy through direct phosphorylation of Ulk1.* Nat Cell Biol, 2011. **13**(2): p. 132-41.

44. Egan, D.F., et al., *Phosphorylation of ULK1 (hATG1) by AMP-activated protein kinase connects energy sensing to mitophagy.* Science, 2011. **331**(6016): p. 456-61.
45. Rubinsztein, D.C., P. Codogno, and B. Levine, *Autophagy modulation as a potential therapeutic target for diverse diseases.* Nat Rev Drug Discov, 2012. **11**(9): p. 709-30.
46. Thoreen, C.C., et al., *An ATP-competitive mammalian target of rapamycin inhibitor reveals rapamycin-resistant functions of mTORC1.* J Biol Chem, 2009. **284**(12): p. 8023-32.
47. Ravikumar, B., et al., *Inhibition of mTOR induces autophagy and reduces toxicity of polyglutamine expansions in fly and mouse models of Huntington disease.* Nat Genet, 2004. **36**(6): p. 585-95.
48. Kim, K.W., et al., *Autophagy upregulation by inhibitors of caspase-3 and mTOR enhances radiotherapy in a mouse model of lung cancer.* Autophagy, 2008. **4**(5): p. 659-68.
49. Sarkar, S., et al., *Lithium induces autophagy by inhibiting inositol monophosphatase.* J Cell Biol, 2005. **170**(7): p. 1101-11.
50. Williams, A., et al., *Novel targets for Huntington's disease in an mTOR-independent autophagy pathway.* Nat Chem Biol, 2008. **4**(5): p. 295-305.
51. Ganley, I.G., et al., *Distinct autophagosomal-lysosomal fusion mechanism revealed by thapsigargin-induced autophagy arrest.* Mol Cell, 2011. **42**(6): p. 731-43.
52. Sarkar, S., et al., *Complex inhibitory effects of nitric oxide on autophagy.* Mol Cell, 2011. **43**(1): p. 19-32.
53. Siddiqi, F.H., et al., *Felodipine induces autophagy in mouse brains with pharmacokinetics amenable to repurposing.* Nat Commun, 2019. **10**(1): p. 1817.
54. Sarkar, S., et al., *Trehalose, a novel mTOR-independent autophagy enhancer, accelerates the clearance of mutant huntingtin and alpha-synuclein.* J Biol Chem, 2007. **282**(8): p. 5641-52.
55. DeBosch, B.J., et al., *Trehalose inhibits solute carrier 2A (SLC2A) proteins to induce autophagy and prevent hepatic steatosis.* Sci Signal, 2016. **9**(416): p. ra21.
56. Buzzai, M., et al., *Systemic treatment with the antidiabetic drug metformin selectively impairs p53-deficient tumor cell growth.* Cancer Res, 2007. **67**(14): p. 6745-52.
57. Sarkar, S., et al., *Small molecules enhance autophagy and reduce toxicity in Huntington's disease models.* Nat Chem Biol, 2007. **3**(6): p. 331-8.
58. Morselli, E., et al., *Caloric restriction and resveratrol promote longevity through the Sirtuin-1-dependent induction of autophagy.* Cell Death Dis, 2010. **1**(1): p. e10.
59. Park, D., et al., *Resveratrol induces autophagy by directly inhibiting mTOR through ATP competition.* Sci Rep, 2016. **6**: p. 21772.
60. Eisenberg, T., et al., *Induction of autophagy by spermidine promotes longevity.* Nat Cell Biol, 2009. **11**(11): p. 1305-14.
61. Wang, J., et al., *Vitamin D3 induces autophagy of human myeloid leukemia cells.* J Biol Chem, 2008. **283**(37): p. 25596-25605.
62. Yuk, J.M., et al., *Vitamin D3 induces autophagy in human monocytes/macrophages via cathelicidin.* Cell Host Microbe, 2009. **6**(3): p. 231-43.
63. Kimura, S., T. Noda, and T. Yoshimori, *Dissection of the autophagosome maturation process by a novel reporter protein, tandem fluorescent-tagged LC3.* Autophagy, 2007. **3**(5): p. 452-60.
64. Bejarano, E., et al., *Defective recruitment of motor proteins to autophagic compartments contributes to autophagic failure in aging.* Aging Cell, 2018. **17**(4): p. e12777.
65. Mizushima, N., T. Yoshimori, and B. Levine, *Methods in mammalian autophagy research.* Cell, 2010. **140**(3): p. 313-26.

66. Klionsky, D.J., et al., *Guidelines for the use and interpretation of assays for monitoring autophagy.* Autophagy, 2012. **8**(4): p. 445-544.
67. Zhang, G., V. Gurtu, and S.R. Kain, *An enhanced green fluorescent protein allows sensitive detection of gene transfer in mammalian cells.* Biochem Biophys Res Commun, 1996. **227**(3): p. 707-11.
68. Larsen, K.B., et al., *A reporter cell system to monitor autophagy based on p62/SQSTM1.* Autophagy, 2010. **6**(6): p. 784-93.
69. Panda, P.K., et al., *Chemical Screening Approaches Enabling Drug Discovery of Autophagy Modulators for Biomedical Applications in Human Diseases.* Front Cell Dev Biol, 2019. **7**: p. 38.
70. Rabinowitz, J.D. and E. White, *Autophagy and metabolism.* Science, 2010. **330**(6009): p. 1344-8.
71. Lahiri, V., W.D. Hawkins, and D.J. Klionsky, *Watch What You (Self-) Eat: Autophagic Mechanisms that Modulate Metabolism.* Cell Metab, 2019. **29**(4): p. 803-826.
72. King, K.E., T.T. Losier, and R.C. Russell, *Regulation of Autophagy Enzymes by Nutrient Signaling.* Trends Biochem Sci, 2021. **46**(8): p. 687-700.
73. Rabanal-Ruiz, Y., E.G. Otten, and V.I. Korolchuk, *mTORC1 as the main gateway to autophagy.* Essays Biochem, 2017. **61**(6): p. 565-584.
74. Hofer, S.J., et al., *Mechanisms of spermidine-induced autophagy and geroprotection.* Nat Aging, 2022. **2**(12): p. 1112-1129.
75. Fang, E.F., et al., *NAD(+) in Aging: Molecular Mechanisms and Translational Implications.* Trends Mol Med, 2017. **23**(10): p. 899-916.
76. Lautrup, S., et al., *NAD(+) in Brain Aging and Neurodegenerative Disorders.* Cell Metab, 2019. **30**(4): p. 630-655.
77. Xiao, W., et al., *NAD(H) and NADP(H) Redox Couples and Cellular Energy Metabolism.* Antioxid Redox Signal, 2018. **28**(3): p. 251-272.
78. Cambronne, X.A. and W.L. Kraus, *Location, Location, Location: Compartmentalization of NAD(+) Synthesis and Functions in Mammalian Cells.* Trends Biochem Sci, 2020. **45**(10): p. 858-873.
79. Schmauck-Medina, T., et al., *New hallmarks of ageing: a 2022 Copenhagen ageing meeting summary.* Aging (Albany NY), 2022. **14**(16): p. 6829-6839.
80. Sedlackova, L. and V.I. Korolchuk, *The crosstalk of NAD, ROS and autophagy in cellular health and ageing.* Biogerontology, 2020. **21**(3): p. 381-397.
81. Kaeberlein, M., M. McVey, and L. Guarente, *The SIR2/3/4 complex and SIR2 alone promote longevity in Saccharomyces cerevisiae by two different mechanisms.* Genes Dev, 1999. **13**(19): p. 2570-80.
82. Bjedov, I., et al., *Fine-tuning autophagy maximises lifespan and is associated with changes in mitochondrial gene expression in Drosophila.* PLoS Genet, 2020. **16**(11): p. e1009083.
83. Mitchell, S.J., et al., *Nicotinamide Improves Aspects of Healthspan, but Not Lifespan, in Mice.* Cell Metab, 2018. **27**(3): p. 667-676 e4.
84. Fang, E.F., et al., *NAD(+) augmentation restores mitophagy and limits accelerated aging in Werner syndrome.* Nat Commun, 2019. **10**(1): p. 5284.
85. Fang, E.F., et al., *NAD(+) Replenishment Improves Lifespan and Healthspan in Ataxia Telangiectasia Models via Mitophagy and DNA Repair.* Cell Metab, 2016. **24**(4): p. 566-581.
86. Fang, E.F., et al., *Defective mitophagy in XPA via PARP-1 hyperactivation and NAD(+)/SIRT1 reduction.* Cell, 2014. **157**(4): p. 882-896.

87. Fang, E.F. and J. Tao, *Targeting on the NAD(+)-mitophagy axis to treat cardiovascular disease.* Aging Med (Milton), 2020. **3**(3): p. 151-152.
88. Aman, Y., et al., *The NAD(+)-mitophagy axis in healthy longevity and in artificial intelligence-based clinical applications.* Mech Ageing Dev, 2020. **185**: p. 111194.
89. Fang, E.F., *Mitophagy and NAD(+) inhibit Alzheimer disease.* Autophagy, 2019. **15**(6): p. 1112-1114.
90. Levine, B., N. Mizushima, and H.W. Virgin, *Autophagy in immunity and inflammation.* Nature, 2011. **469**(7330): p. 323-35.
91. Jiang, T., et al., *Temsirolimus attenuates tauopathy in vitro and in vivo by targeting tau hyperphosphorylation and autophagic clearance.* Neuropharmacology, 2014. **85**: p. 121-30.
92. Mizushima, N., et al., *Autophagy fights disease through cellular self-digestion.* Nature, 2008. **451**(7182): p. 1069-75.
93. Jiang, P. and N. Mizushima, *Autophagy and human diseases.* Cell Res, 2014. **24**(1): p. 69-79.
94. Levine, B. and G. Kroemer, *Autophagy in the pathogenesis of disease.* Cell, 2008. **132**(1): p. 27-42.
95. Menzies, F.M., et al., *Autophagy and Neurodegeneration: Pathogenic Mechanisms and Therapeutic Opportunities.* Neuron, 2017. **93**(5): p. 1015-1034.
96. Seranova, E., et al., *Dysregulation of autophagy as a common mechanism in lysosomal storage diseases.* Essays Biochem, 2017. **61**(6): p. 733-749.
97. Sarkar, S., *Chemical screening platforms for autophagy drug discovery to identify therapeutic candidates for Huntington's disease and other neurodegenerative disorders.* Drug Discov Today Technol, 2013. **10**(1): p. e137-44.
98. Erkkinen, M.G., M.O. Kim, and M.D. Geschwind, *Clinical Neurology and Epidemiology of the Major Neurodegenerative Diseases.* Cold Spring Harb Perspect Biol, 2018. **10**(4).
99. Dugger, B.N. and D.W. Dickson, *Pathology of Neurodegenerative Diseases.* Cold Spring Harb Perspect Biol, 2017. **9**(7).
100. Prusiner, S.B., *Shattuck lecture--neurodegenerative diseases and prions.* N Engl J Med, 2001. **344**(20): p. 1516-26.
101. Jucker, M. and L.C. Walker, *Self-propagation of pathogenic protein aggregates in neurodegenerative diseases.* Nature, 2013. **501**(7465): p. 45-51.
102. Taylor, J.P., J. Hardy, and K.H. Fischbeck, *Toxic proteins in neurodegenerative disease.* Science, 2002. **296**(5575): p. 1991-5.
103. Rubinsztein, D.C., *The roles of intracellular protein-degradation pathways in neurodegeneration.* Nature, 2006. **443**(7113): p. 780-6.
104. Wilson, D.M., 3rd, et al., *Hallmarks of neurodegenerative diseases.* Cell, 2023. **186**(4): p. 693-714.
105. Krainc, D., *Clearance of mutant proteins as a therapeutic target in neurodegenerative diseases.* Arch Neurol, 2010. **67**(4): p. 388-92.
106. Johri, A. and M.F. Beal, *Mitochondrial dysfunction in neurodegenerative diseases.* J Pharmacol Exp Ther, 2012. **342**(3): p. 619-30.
107. Nunnari, J. and A. Suomalainen, *Mitochondria: in sickness and in health.* Cell, 2012. **148**(6): p. 1145-59.
108. Nguyen, T.N., et al., *Atg8 family LC3/GABARAP proteins are crucial for autophagosome-lysosome fusion but not autophagosome formation during PINK1/Parkin mitophagy and starvation.* J Cell Biol, 2016. **215**(6): p. 857-874.
109. Doblado, L., et al., *Mitophagy in Human Diseases.* Int J Mol Sci, 2021. **22**(8).

110. Guo, C., et al., *Oxidative stress, mitochondrial damage and neurodegenerative diseases.* Neural Regen Res, 2013. **8**(21): p. 2003-14.
111. Maleki, N., et al., *Diabetes mellitus, diabetes insipidus, optic atrophy, and deafness: A case of Wolfram (DIDMOAD) syndrome.* J Curr Ophthalmol, 2015. **27**(3-4): p. 132-5.
112. Page, M.M., A.C. Asmal, and C.R. Edwards, *Recessive inheritance of diabetes: the syndrome of diabetes insipidus, diabetes mellitus, optic atrophy and deafness.* Q J Med, 1976. **45**(179): p. 505-20.
113. Cremers, C.W., P.G. Wijdeveld, and A.J. Pinckers, *Juvenile diabetes mellitus, optic atrophy, hearing loss, diabetes insipidus, atonia of the urinary tract and bladder, and other abnormalities (Wolfram syndrome). A review of 88 cases from the literature with personal observations on 3 new patients.* Acta Paediatr Scand Suppl, 1977(264): p. 1-16.
114. Fraser, F.C. and T. Gunn, *Diabetes mellitus, diabetes insipidus, and optic atrophy. An autosomal recessive syndrome?* J Med Genet, 1977. **14**(3): p. 190-3.
115. Barrett, T.G., S.E. Bundey, and A.F. Macleod, *Neurodegeneration and diabetes: UK nationwide study of Wolfram (DIDMOAD) syndrome.* Lancet, 1995. **346**(8988): p. 1458-63.
116. Kumar, S., *Wolfram syndrome: important implications for pediatricians and pediatric endocrinologists.* Pediatr Diabetes, 2010. **11**(1): p. 28-37.
117. Inoue, H., et al., *A gene encoding a transmembrane protein is mutated in patients with diabetes mellitus and optic atrophy (Wolfram syndrome).* Nat Genet, 1998. **20**(2): p. 143-8.
118. Takeda, K., et al., *WFS1 (Wolfram syndrome 1) gene product: predominant subcellular localization to endoplasmic reticulum in cultured cells and neuronal expression in rat brain.* Hum Mol Genet, 2001. **10**(5): p. 477-84.
119. Fonseca, S.G., et al., *Wolfram syndrome 1 gene negatively regulates ER stress signaling in rodent and human cells.* J Clin Invest, 2010. **120**(3): p. 744-55.
120. Fonseca, S.G., et al., *WFS1 is a novel component of the unfolded protein response and maintains homeostasis of the endoplasmic reticulum in pancreatic beta-cells.* J Biol Chem, 2005. **280**(47): p. 39609-15.
121. Yamada, T., et al., *WFS1-deficiency increases endoplasmic reticulum stress, impairs cell cycle progression and triggers the apoptotic pathway specifically in pancreatic beta-cells.* Hum Mol Genet, 2006. **15**(10): p. 1600-9.
122. Hetz, C., *The unfolded protein response: controlling cell fate decisions under ER stress and beyond.* Nat Rev Mol Cell Biol, 2012. **13**(2): p. 89-102.
123. Rutkowski, D.T. and R.S. Hegde, *Regulation of basal cellular physiology by the homeostatic unfolded protein response.* J Cell Biol, 2010. **189**(5): p. 783-94.
124. Li, Y., S. Li, and H. Wu, *Ubiquitination-Proteasome System (UPS) and Autophagy Two Main Protein Degradation Machineries in Response to Cell Stress.* Cells, 2022. **11**(5).
125. Senft, D. and Z.A. Ronai, *UPR, autophagy, and mitochondria crosstalk underlies the ER stress response.* Trends Biochem Sci, 2015. **40**(3): p. 141-8.
126. Zatyka, M., et al., *Depletion of WFS1 compromises mitochondrial function in hiPSC-derived neuronal models of Wolfram syndrome.* Stem Cell Reports, 2023. **18**(5): p. 1090-1106.
127. Paillusson, S., et al., *There's Something Wrong with my MAM; the ER-Mitochondria Axis and Neurodegenerative Diseases.* Trends Neurosci, 2016. **39**(3): p. 146-157.
128. Wobus, A.M. and K.R. Boheler, *Embryonic stem cells: prospects for developmental biology and cell therapy.* Physiol Rev, 2005. **85**(2): p. 635-78.
129. Zhang, S.C., et al., *In vitro differentiation of transplantable neural precursors from human embryonic stem cells.* Nat Biotechnol, 2001. **19**(12): p. 1129-33.

130. Lamba, D.A., et al., *Efficient generation of retinal progenitor cells from human embryonic stem cells.* Proc Natl Acad Sci U S A, 2006. **103**(34): p. 12769-74.
131. Lim, U.M., K.S. Sidhu, and B.E. Tuch, *Derivation of Motor Neurons from three Clonal Human Embryonic Stem Cell Lines.* Curr Neurovasc Res, 2006. **3**(4): p. 281-8.
132. Anderson, J.S., et al., *Derivation of normal macrophages from human embryonic stem (hES) cells for applications in HIV gene therapy.* Retrovirology, 2006. **3**: p. 24.
133. Lavon, N., O. Yanuka, and N. Benvenisty, *Differentiation and isolation of hepatic-like cells from human embryonic stem cells.* Differentiation, 2004. **72**(5): p. 230-8.
134. Sun, C., et al., *NAD depletion mediates cytotoxicity in human neurons with autophagy deficiency.* Cell Rep, 2023. **42**(5): p. 112372.
135. Sartipy, P., et al., *The application of human embryonic stem cell technologies to drug discovery.* Drug Discov Today, 2007. **12**(17-18): p. 688-99.
136. Friedrich Ben-Nun, I. and N. Benvenisty, *Human embryonic stem cells as a cellular model for human disorders.* Mol Cell Endocrinol, 2006. **252**(1-2): p. 154-9.
137. Frake, R.A., et al., *Autophagy and neurodegeneration.* J Clin Invest, 2015. **125**(1): p. 65-74.
138. Tanaka, M., et al., *Trehalose alleviates polyglutamine-mediated pathology in a mouse model of Huntington disease.* Nat Med, 2004. **10**(2): p. 148-54.
139. Rose, C., et al., *Rilmenidine attenuates toxicity of polyglutamine expansions in a mouse model of Huntington's disease.* Hum Mol Genet, 2010. **19**(11): p. 2144-53.
140. Caccamo, A., et al., *Molecular interplay between mammalian target of rapamycin (mTOR), amyloid-beta, and Tau: effects on cognitive impairments.* J Biol Chem, 2010. **285**(17): p. 13107-20.
141. Du, J., et al., *Trehalose rescues Alzheimer's disease phenotypes in APP/PS1 transgenic mice.* J Pharm Pharmacol, 2013. **65**(12): p. 1753-6.
142. Zhang, L., et al., *Evaluating the Effectiveness of GTM-1, Rapamycin, and Carbamazepine on Autophagy and Alzheimer Disease.* Med Sci Monit, 2017. **23**: p. 801-808.
143. Silva, M.C., et al., *Human iPSC-Derived Neuronal Model of Tau-A152T Frontotemporal Dementia Reveals Tau-Mediated Mechanisms of Neuronal Vulnerability.* Stem Cell Reports, 2016. **7**(3): p. 325-340.
144. Holler, C.J., et al., *Trehalose upregulates progranulin expression in human and mouse models of GRN haploinsufficiency: a novel therapeutic lead to treat frontotemporal dementia.* Mol Neurodegener, 2016. **11**(1): p. 46.
145. Malagelada, C., et al., *Rapamycin protects against neuron death in in vitro and in vivo models of Parkinson's disease.* J Neurosci, 2010. **30**(3): p. 1166-75.
146. Pupyshev, A.B., et al., *Restoration of Parkinson's Disease-Like Deficits by Activating Autophagy through mTOR-Dependent and mTOR-Independent Mechanisms in Pharmacological and Transgenic Models of Parkinson's Disease in Mice.* Bull Exp Biol Med, 2021. **171**(4): p. 425-430.
147. Pupyshev, A.B., et al., *Therapeutic activation of autophagy by combined treatment with rapamycin and trehalose in a mouse MPTP-induced model of Parkinson's disease.* Pharmacol Biochem Behav, 2019. **177**: p. 1-11.
148. Siddiqui, A., et al., *Mitochondrial Quality Control via the PGC1alpha-TFEB Signaling Pathway Is Compromised by Parkin Q311X Mutation But Independently Restored by Rapamycin.* J Neurosci, 2015. **35**(37): p. 12833-44.
149. Zhang, X., et al., *Rapamycin treatment augments motor neuron degeneration in SOD1(G93A) mouse model of amyotrophic lateral sclerosis.* Autophagy, 2011. **7**(4): p. 412-25.

150. Zhang, X., et al., *MTOR-independent, autophagic enhancer trehalose prolongs motor neuron survival and ameliorates the autophagic flux defect in a mouse model of amyotrophic lateral sclerosis.* Autophagy, 2014. **10**(4): p. 588-602.
151. Maetzel, D., et al., *Genetic and chemical correction of cholesterol accumulation and impaired autophagy in hepatic and neural cells derived from Niemann-Pick Type C patient-specific iPS cells.* Stem Cell Reports, 2014. **2**(6): p. 866-80.
152. Boya, P., F. Reggiori, and P. Codogno, *Emerging regulation and functions of autophagy.* Nat Cell Biol, 2013. **15**(7): p. 713-20.
153. Stavoe, A.K.H. and E.L.F. Holzbaur, *Autophagy in Neurons.* Annu Rev Cell Dev Biol, 2019. **35**: p. 477-500.
154. Hara, T., et al., *Suppression of basal autophagy in neural cells causes neurodegenerative disease in mice.* Nature, 2006. **441**(7095): p. 885-9.
155. Komatsu, M., et al., *Loss of autophagy in the central nervous system causes neurodegeneration in mice.* Nature, 2006. **441**(7095): p. 880-4.
156. Bjedov, I., et al., *Mechanisms of life span extension by rapamycin in the fruit fly Drosophila melanogaster.* Cell Metab, 2010. **11**(1): p. 35-46.
157. Suzuki, S.W., J. Onodera, and Y. Ohsumi, *Starvation induced cell death in autophagy-defective yeast mutants is caused by mitochondria dysfunction.* PLoS One, 2011. **6**(2): p. e17412.
158. Nixon, R.A., *The role of autophagy in neurodegenerative disease.* Nat Med, 2013. **19**(8): p. 983-97.
159. Avior, Y., I. Sagi, and N. Benvenisty, *Pluripotent stem cells in disease modelling and drug discovery.* Nat Rev Mol Cell Biol, 2016. **17**(3): p. 170-82.
160. Soldner, F. and R. Jaenisch, *Stem Cells, Genome Editing, and the Path to Translational Medicine.* Cell, 2018. **175**(3): p. 615-632.
161. Kuma, A., et al., *The role of autophagy during the early neonatal starvation period.* Nature, 2004. **432**(7020): p. 1032-6.
162. Mizushima, N., T. Yoshimori, and Y. Ohsumi, *The role of Atg proteins in autophagosome formation.* Annu Rev Cell Dev Biol, 2011. **27**: p. 107-32.
163. Chambers, S.M., et al., *Highly efficient neural conversion of human ES and iPS cells by dual inhibition of SMAD signaling.* Nat Biotechnol, 2009. **27**(3): p. 275-80.
164. Tao, Y. and S.C. Zhang, *Neural Subtype Specification from Human Pluripotent Stem Cells.* Cell Stem Cell, 2016. **19**(5): p. 573-586.
165. Altman, B.J. and J.C. Rathmell, *Metabolic stress in autophagy and cell death pathways.* Cold Spring Harb Perspect Biol, 2012. **4**(9): p. a008763.
166. Guo, J.Y., et al., *Autophagy provides metabolic substrates to maintain energy charge and nucleotide pools in Ras-driven lung cancer cells.* Genes Dev, 2016. **30**(15): p. 1704-17.
167. Lunt, S.Y. and M.G. Vander Heiden, *Aerobic glycolysis: meeting the metabolic requirements of cell proliferation.* Annu Rev Cell Dev Biol, 2011. **27**: p. 441-64.
168. Fernie, A.R., F. Carrari, and L.J. Sweetlove, *Respiratory metabolism: glycolysis, the TCA cycle and mitochondrial electron transport.* Curr Opin Plant Biol, 2004. **7**(3): p. 254-61.
169. Morzorati, S.L., W.J. McBride, and R.C. Frederickson, *Excitatory effect of L-aspartate and L-glutamate on Purkinje cells in rat cerebellum.* Brain Res Bull, 1981. **7**(4): p. 445-7.
170. Modoux, M., et al., *Tryptophan Metabolism as a Pharmacological Target.* Trends Pharmacol Sci, 2021. **42**(1): p. 60-73.

171. Hasmann, M. and I. Schemainda, *FK866, a highly specific noncompetitive inhibitor of nicotinamide phosphoribosyltransferase, represents a novel mechanism for induction of tumor cell apoptosis.* Cancer Res, 2003. **63**(21): p. 7436-42.
172. Yoshino, J., J.A. Baur, and S.I. Imai, *NAD(+) Intermediates: The Biology and Therapeutic Potential of NMN and NR.* Cell Metab, 2018. **27**(3): p. 513-528.
173. Reiten, O.K., et al., *Preclinical and clinical evidence of NAD(+) precursors in health, disease, and ageing.* Mech Ageing Dev, 2021. **199**: p. 111567.
174. Verdin, E., *NAD(+) in aging, metabolism, and neurodegeneration.* Science, 2015. **350**(6265): p. 1208-13.
175. Katsyuba, E., et al., *NAD(+) homeostasis in health and disease.* Nat Metab, 2020. **2**(1): p. 9-31.
176. Canto, C., A.A. Sauve, and P. Bai, *Crosstalk between poly(ADP-ribose) polymerase and sirtuin enzymes.* Mol Aspects Med, 2013. **34**(6): p. 1168-201.
177. Luna, A., M.I. Aladjem, and K.W. Kohn, *SIRT1/PARP1 crosstalk: connecting DNA damage and metabolism.* Genome Integr, 2013. **4**(1): p. 6.
178. Hewitt, G. and V.I. Korolchuk, *Repair, Reuse, Recycle: The Expanding Role of Autophagy in Genome Maintenance.* Trends Cell Biol, 2017. **27**(5): p. 340-351.
179. Ying, W., *NAD+/NADH and NADP+/NADPH in cellular functions and cell death: regulation and biological consequences.* Antioxid Redox Signal, 2008. **10**(2): p. 179-206.
180. Martinez-Reyes, I. and N.S. Chandel, *Mitochondrial TCA cycle metabolites control physiology and disease.* Nat Commun, 2020. **11**(1): p. 102.
181. Pickles, S., P. Vigie, and R.J. Youle, *Mitophagy and Quality Control Mechanisms in Mitochondrial Maintenance.* Curr Biol, 2018. **28**(4): p. R170-R185.
182. Zhang, L., et al., *Modulation of mitochondrial complex I activity averts cognitive decline in multiple animal models of familial Alzheimer's Disease.* EBioMedicine, 2015. **2**(4): p. 294-305.
183. Zheng, X., et al., *Metabolic reprogramming during neuronal differentiation from aerobic glycolysis to neuronal oxidative phosphorylation.* Elife, 2016. **5**.
184. Aman, Y., et al., *Autophagy in healthy aging and disease.* Nat Aging, 2021. **1**(8): p. 634-650.
185. Ruan, L., et al., *Mitochondria-Associated Proteostasis.* Annu Rev Biophys, 2020. **49**: p. 41-67.
186. Romani, M., et al., *NAD(+) boosting reduces age-associated amyloidosis and restores mitochondrial homeostasis in muscle.* Cell Rep, 2021. **34**(3): p. 108660.
187. Nowicka, U., et al., *Cytosolic aggregation of mitochondrial proteins disrupts cellular homeostasis by stimulating the aggregation of other proteins.* Elife, 2021. **10**.
188. Katsyuba, E., et al., *De novo NAD(+) synthesis enhances mitochondrial function and improves health.* Nature, 2018. **563**(7731): p. 354-359.
189. Navarro, S. and S. Ventura, *Fluorescent dye ProteoStat to detect and discriminate intracellular amyloid-like aggregates in Escherichia coli.* Biotechnol J, 2014. **9**(10): p. 1259-66.
190. Sirangelo, I. and G. Irace, *Inhibition of aggregate formation as therapeutic target in protein misfolding diseases: effect of tetracycline and trehalose.* Expert Opin Ther Targets, 2010. **14**(12): p. 1311-21.
191. Kataura, T., et al., *Autophagy promotes cell survival by maintaining NAD levels.* Dev Cell, 2022. **57**(22): p. 2584-2598 e11.

192. Boissart, C., et al., *Differentiation from human pluripotent stem cells of cortical neurons of the superficial layers amenable to psychiatric disease modeling and high-throughput drug screening.* Transl Psychiatry, 2013. **3**(8): p. e294.
193. Pourtoy-Brasselet, S., et al., *Human iPSC-derived neurons reveal early developmental alteration of neurite outgrowth in the late-occurring neurodegenerative Wolfram syndrome.* Am J Hum Genet, 2021. **108**(11): p. 2171-2185.
194. Shang, L., et al., *beta-cell dysfunction due to increased ER stress in a stem cell model of Wolfram syndrome.* Diabetes, 2014. **63**(3): p. 923-33.
195. Sarkar, S., et al., *Impaired autophagy in the lipid-storage disorder Niemann-Pick type C1 disease.* Cell Rep, 2013. **5**(5): p. 1302-15.
196. Makarov, M.V., et al., *Scalable syntheses of traceable ribosylated NAD(+) precursors.* Org Biomol Chem, 2019. **17**(38): p. 8716-8720.
197. Yang, Y., et al., *Dihydronicotinamide riboside is a potent NAD(+) concentration enhancer in vitro and in vivo.* J Biol Chem, 2019. **294**(23): p. 9295-9307.
198. Crouzier, L., et al., *Activation of the sigma-1 receptor chaperone alleviates symptoms of Wolfram syndrome in preclinical models.* Sci Transl Med, 2022. **14**(631): p. eabh3763.
199. Crouzier, L., et al., *Use of Zebrafish Models to Boost Research in Rare Genetic Diseases.* Int J Mol Sci, 2021. **22**(24).
200. Hershey, T., et al., *Early brain vulnerability in Wolfram syndrome.* PLoS One, 2012. **7**(7): p. e40604.
201. Lugar, H.M., et al., *Evidence for altered neurodevelopment and neurodegeneration in Wolfram syndrome using longitudinal morphometry.* Sci Rep, 2019. **9**(1): p. 6010.
202. Yang, Y., et al., *NRH salvage and conversion to NAD(+) requires NRH kinase activity by adenosine kinase.* Nat Metab, 2020. **2**(4): p. 364-379.
203. Matilla-Duenas, A., et al., *Rare Neurodegenerative Diseases: Clinical and Genetic Update.* Adv Exp Med Biol, 2017. **1031**: p. 443-496.
204. Caza, T., et al., *Cell type-specific mechanistic target of rapamycin-dependent distortion of autophagy pathways in lupus nephritis.* Transl Res, 2022. **245**: p. 55-81.
205. Cohen, M.A., P. Itsykson, and B.E. Reubinoff, *Neural differentiation of human ES cells.* Curr Protoc Cell Biol, 2007. **Chapter 23**: p. Unit 23 7.
206. Schindelin, J., et al., *Fiji: an open-source platform for biological-image analysis.* Nat Methods, 2012. **9**(7): p. 676-82.
207. Berg, S., et al., *ilastik: interactive machine learning for (bio)image analysis.* Nat Methods, 2019. **16**(12): p. 1226-1232.
208. Tinevez, J.Y., et al., *TrackMate: An open and extensible platform for single-particle tracking.* Methods, 2017. **115**: p. 80-90.
209. Mitsuishi, Y., et al., *Nrf2 redirects glucose and glutamine into anabolic pathways in metabolic reprogramming.* Cancer Cell, 2012. **22**(1): p. 66-79.
210. Saito, T., et al., *p62/Sqstm1 promotes malignancy of HCV-positive hepatocellular carcinoma through Nrf2-dependent metabolic reprogramming.* Nat Commun, 2016. **7**: p. 12030.
211. Komatsu, M., et al., *The selective autophagy substrate p62 activates the stress responsive transcription factor Nrf2 through inactivation of Keap1.* Nat Cell Biol, 2010. **12**(3): p. 213-23.
212. Hansen, M., D.C. Rubinsztein, and D.W. Walker, *Autophagy as a promoter of longevity: insights from model organisms.* Nat Rev Mol Cell Biol, 2018. **19**(9): p. 579-593.

213. Lin, M.T. and M.F. Beal, *Mitochondrial dysfunction and oxidative stress in neurodegenerative diseases.* Nature, 2006. **443**(7113): p. 787-95.
214. Schondorf, D.C., et al., *The NAD+ Precursor Nicotinamide Riboside Rescues Mitochondrial Defects and Neuronal Loss in iPSC and Fly Models of Parkinson's Disease.* Cell Rep, 2018. **23**(10): p. 2976-2988.
215. Kataura, T., et al., *Targeting the autophagy-NAD axis protects against cell death in Niemann-Pick type C1 disease models.* Cell Death Dis, 2024. **15**(5): p. 382.
216. Eichmuller, O.L. and J.A. Knoblich, *Human cerebral organoids - a new tool for clinical neurology research.* Nat Rev Neurol, 2022. **18**(11): p. 661-680.
217. Korsgen, M.E., et al., *Analysis of autophagy deficiency and cytotoxicity in autophagy-deficient human embryonic stem cell-derived neurons.* STAR Protoc, 2023. **4**(3): p. 102529.
218. Sun, C., et al., *Autophagy Dysfunction as a Phenotypic Readout in hiPSC-Derived Neuronal Cell Models of Neurodegenerative Diseases*, in *Induced Pluripotent Stem Cells and Human Disease: Methods and Protocols*, K. Turksen, Editor. 2022, Springer US: New York, NY. p. 103-136.
219. Rosenstock, T.R., et al., *Analysis of Mitochondrial Dysfunction by Microplate Reader in hiPSC-Derived Neuronal Cell Models of Neurodegenerative Disorders.* Methods Mol Biol, 2022. **2549**: p. 1-21.
220. Lengner, C.J., et al., *Derivation of pre-X inactivation human embryonic stem cells under physiological oxygen concentrations.* Cell, 2010. **141**(5): p. 872-83.
221. Cermak, T., et al., *Efficient design and assembly of custom TALEN and other TAL effector-based constructs for DNA targeting.* Nucleic Acids Res, 2011. **39**(12): p. e82.
222. Heyes, J., et al., *Cationic lipid saturation influences intracellular delivery of encapsulated nucleic acids.* J Control Release, 2005. **107**(2): p. 276-87.
223. Seranova, E., et al., *In Vitro Screening Platforms for Identifying Autophagy Modulators in Mammalian Cells.* Methods Mol Biol, 2019. **1880**: p. 389-428.
224. Sun, C., et al., *Autophagy Dysfunction as a Phenotypic Readout in hiPSC-Derived Neuronal Cell Models of Neurodegenerative Diseases.* Methods Mol Biol, 2022. **2549**: p. 103-136.
225. Hummon, A.B., et al., *Isolation and solubilization of proteins after TRIzol extraction of RNA and DNA from patient material following prolonged storage.* Biotechniques, 2007. **42**(4): p. 467-70, 472.
226. Bligh, E.G. and W.J. Dyer, *A rapid method of total lipid extraction and purification.* Can J Biochem Physiol, 1959. **37**(8): p. 911-7.
227. Maddocks, O.D., et al., *Serine Metabolism Supports the Methionine Cycle and DNA/RNA Methylation through De Novo ATP Synthesis in Cancer Cells.* Mol Cell, 2016. **61**(2): p. 210-21.
228. Pluskal, T., et al., *MZmine 2: modular framework for processing, visualizing, and analyzing mass spectrometry-based molecular profile data.* BMC Bioinformatics, 2010. **11**: p. 395.
229. Chambers, M.C., et al., *A cross-platform toolkit for mass spectrometry and proteomics.* Nat Biotechnol, 2012. **30**(10): p. 918-20.
230. Xia, J. and D.S. Wishart, *Web-based inference of biological patterns, functions and pathways from metabolomic data using MetaboAnalyst.* Nat Protoc, 2011. **6**(6): p. 743-60.
231. Gharanei, S., et al., *Vacuolar-type H+-ATPase V1A subunit is a molecular partner of Wolfram syndrome 1 (WFS1) protein, which regulates its expression and stability.* Hum Mol Genet, 2013. **22**(2): p. 203-17.

Appendix

Appendix 1: List of published articles

1. Targeting the autophagy-NAD axis protects against cell death in Niemann-Pick type C1 disease models. Kataura T.*†, Sedlackova L.*, **Sun C**., Kocak G., Wilson N., Banks P., Hayat F., Trushin S., Trushina E., Maddocks O.D.K., Oblong J.E., Miwa S., Imoto M., Saiki S., Erskine D., Migaud M.E., Sarkar S.† and Korolchuk V.I.† ***Cell Death and Disease*** 15(5): 382 (2024) [PMID: 38821960]. *Equal contribution; †Corresponding author

2. NAD depletion mediates cytotoxicity in human neurons with autophagy deficiency. **Sun C**.*, Seranova E.*, Cohen M.A.*, Chipara M., Roberts J., Astuti D., Palhegyi A.M., Acharjee A., Sedlackova L., Kataura T., Otten E.G., Panda P.K., Reyna S.L., Korsgen M.E., Kauffman K.J., Huerta-Uribe A., Zatyka M., Silva L.F.S.E., Torresi J., Zhang S., Hughes G.W., Ward C., Kuechler E.R., Cartwright D., Trushin S., Trushina E., Sahay G., Buganim Y., Lavery G.G., Gsponer J., Anderson D.G., Frickel E.M., Rosenstock T.R., Barrett T., Maddocks O.D.K., Tennant D.A., Wang H., Jaenisch R., Korolchuk V.I.† and Sarkar S.† ***Cell Reports*** 42(5): 112372 (2023) [PMID: 37086404]. *Equal contribution; †Corresponding authors

   Features:

   - *New insights into the autophagy-NAD axis in brain disease. Cell Reports 42(5): 112420 (20 April 2023) [Preview].*
   - *Brain cells are starved of energy when autophagy malfunctions, new study finds. University of Birmingham (28 April 2023) [News].*
   - *How brain cells are starved of energy in autophagy dysfunction. The Print (30 April 2023) [News].*

3. Depletion of WFS1 compromises mitochondrial function in hiPSC-derived neuronal models of Wolfram syndrome. Zatyka M.*, Rosenstock T.R.*, **Sun C.**, Palhegyi A.M., Hughes G.W., Reyna S.L., Astuti D., Maio A.D., Sciauvaud A., Korsgen M.E., Stanulovic V., Kocak G., Rak M., Pourtoy-Brasselet S., Winter K., Varga T., Jarrige M., Polveche H., Correia J., Frickel E.M., Hoogenkamp M., Ward D.G., Aubry L., Barrett T. and Sarkar S.† ***Stem Cell Reports*** 18(5): 1090-1106 (2023) [PMID: 37163979]. *Equal contribution; †Corresponding author

Feature:

- *Brain cell death in rare disease Wolfram syndrome linked to mitochondrial defects. University of Birmingham (17 May 2023) [News].*

4. Analysis of autophagy deficiency and cytotoxicity in autophagy-deficient human embryonic stem cell-derived neurons. Korsgen M.E.*, **Sun C.***, Seranova E., Zatyka M., Astuti D., Kataura T., Barrett T., Korolchuk V.I.† and Sarkar S.† ***STAR Protocols*** 4: 102529 (2023) [PMID: 37624702]. *Equal contribution; †Corresponding author

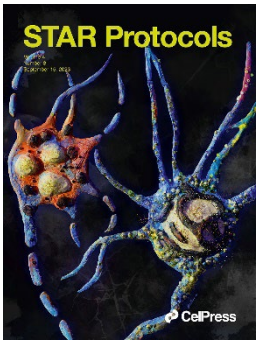

5. The autophagy-NAD axis in longevity and disease. Wilson N.*, Kataura T.*, Korsgen M.E., **Sun C.**, Sarkar S.† and Korolchuk V.I.† ***Trends in Cell Biology*** 33(9): 788-802 (2023) [PMID: 36878731]. *Equal contribution; †Corresponding authors

6. Autophagy promotes cell survival by maintaining NAD levels. Kataura T.*, Sedlackova L.*, Otten E.G., Kumari R., Shapira D., Scialo F., Stefanatos R., Ishikawa K., Kelly G., Seranova E., **Sun C.**, Maetzel D., Kenneth N., Trushin S., Zhang T., Trushina E., Bascom C.C., Tasseff R., Isfort R.J., Oblong J.E., Miwa S., Lazarou M., Jaenisch R., Imoto M., Saiki S., Papamichos-Chronakis M., Manjithaya R., Maddocks O.D.K., Sanz A., Sarkar S.† and Korolchuk V.I.† ***Developmental Cell*** 57(22): 2584-2598 (2022) [PMID: 36413951]. *Equal contribution; †Corresponding authors

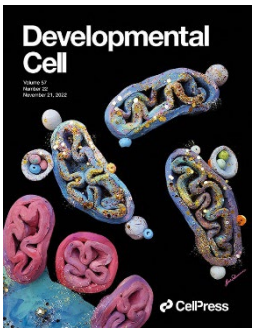

Feature:

- *Researchers at the University of Birmingham have identified the molecular basis of metabolic diseases linked to autophagy. Institute of Cancer and Genomic Sciences, University of Birmingham (30 November 2022) [News].*

7. Analysis of mitochondrial dysfunction by microplate reader in hiPSC-derived neuronal cell models of neurodegenerative disorders.Rosenstock T.R., **Sun C.**, Hughes G.W., Winter K. and Sarkar S.† ***Methods in Molecular Biology*** 2549: 1-21 (2022) [PMID: 35347693]. †Corresponding author

8. Autophagy dysfunction as a phenotypic readout in hiPSC-derived neuronal cell models of neurodegenerative diseases. **Sun C.***, Rosenstock T.R.*, Cohen M.A. and Sarkar S.† ***Methods in Molecular Biology*** 2549: 103-136 (2022) [PMID: 34490597]. *Equal contribution; †Corresponding author

9. Human induced pluripotent stem cell models of neurodegenerative disorders for studying the biomedical implications of autophagy. Seranova E.*, Palhegyi A.M.*, Verma S., Dimova S., Lasry R., Naama M., **Sun C.**, Barrett T., Rosenstock T.R., Kumar D., Cohen M.A., Buganim Y. and Sarkar S.† ***Journal of Molecular Biology*** 432(8): 2754-2798 (2020) [PMID: 32044344]. *Equal contribution, †Corresponding author

Note: Part of my work in this thesis is included in some of the above manuscripts.

Appendix 2: List of conference poster presentations

1. 11th annual scientific meeting MSCA Mercia Stem Cell Alliance at the University of Nottingham on 4th December 2023
    - Targeting the defective autophagy–NAD axis for therapeutic intervention in iPSC-derived neuronal models of neurodegenerative diseases. **Congxin Sun**, Elena Seranova, Malgorzata Zatyka, Gamze Kocak, Laetitia Aubry, Timothy Barrett, Viktor Korolchuk and Sovan Sarkar
    - Human embryonic stem cell-based screening platforms for autophagy modulators. Dewi Astuti, **Congxin Sun**, Malkiel A. Cohen, Elena Seranova, Miriam Körsgen, Timothy Barrett and Sovan Sarkar

2. Manchester Regenerative Medicine Network (MaRMN) and Manchester Rare Conditions Centre (MRCC) Symposium on 'In vitro models of human genetic diseases' at the University of Manchester on 13th September 2023
    - NAD depletion mediates cytotoxicity in human neurons with autophagy deficiency. **Congxin Sun**, Elena Seranova, Malkiel A. Cohen, Miruna Chipara, Jennie Roberts, Dewi Astuti, Adina M. Palhegyi, Animesh Acharjee, Tatiana R. Rosenstock, Samuel Lara Reyna, Tetsushi Kataura, Lucia Sedlackova, Eva Maria Frickel, Timothy Barrett, Oliver D.K. Maddocks, Daniel A. Tennant, Haoyi Wang, Rudolf Jaenisch, Viktor I. Korolchuk and Sovan Sarkar

3. 8th Annual Autophagy UK Network Meeting at the University of Birmingham on 19-20 June 2023
    - NAD depletion mediates cytotoxicity in human neurons with autophagy deficiency. **Congxin Sun**, Elena Seranova, Malkiel A. Cohen, Miruna Chipara, Jennie Roberts, Dewi Astuti, Adina M. Palhegyi, Animesh Acharjee, Tatiana R. Rosenstock, Samuel Lara Reyna, Tetsushi Kataura, Lucia Sedlackova, Eva Maria Frickel, Timothy Barrett, Oliver D.K. Maddocks, Daniel A. Tennant, Haoyi Wang, Rudolf Jaenisch, Viktor I. Korolchuk and Sovan Sarkar